Critical Design Report

J. Hervey, M. Huynh, S. Makar, N. Rusali, C. Santos, A. Solakhyan
Group 4: Demeter's Wings

Contents

List of Figures

List of Tables

I. Summary

A. Executive Summary

This report outlines the progression of design configurations developed prior to the current aircraft configuration, alongside the key considerations that informed our decisions. These preliminary concepts were derived from established agricultural aircraft models that featured characteristics relevant to our mission objectives. Specifically, we examined the AT-802, Airtruk, and EMB 202.

The AT-802 was selected as a foundational reference due to its proven reliability and widespread use in agricultural aviation. However, its size exceeded our operational requirements. The Airtruk was considered for its distinctive rear-loading capability, which offers the potential for reduced turnaround time between missions. Lastly, the EMB 202 was evaluated for its ethanol-compatible engine, enabling fuel flexibility—a valuable feature for varying mission demands.

The report proceeds to detail the aircraft's design methodology, including weight estimation, sizing analysis, and power loading considerations, as well as the design iterations undertaken throughout the process. The initial concept, designated CD-4, was originally envisioned as a fully electric aircraft. However, during the weight and sizing phase, we determined that a fully electric solution would be prohibitively heavy. Consequently, a hybrid series-parallel electric-gas configuration was adopted. This system enables operation via both power sources simultaneously or through the gas engine alone.

Based on a thorough weight analysis, we established an optimal sizing configuration informed by wing loading comparisons with similarly sized aircraft. The resulting parameters aligned closely with existing benchmarks.

Subsequent steps included a detailed weight and balance analysis, using a combination of engineering calculations and historical data from comparable agricultural aircraft to estimate component weights (e.g., engine, motor, and fuel tanks). Additionally, we evaluated center of gravity (CG) travel across various mission phases, accounting for payload release and fuel consumption.

Following CG estimation, we analyzed the neutral point to assess the aircraft's longitudinal stability. Due to the placement of the hopper behind the wing and aft of the CG, significant CG shift was predicted during its operation. To maintain a positive static margin and ensure stable flight, we increased the size of the canards, which effectively adjusted the neutral point.

The report concludes with a brief overview of the propulsion architecture, followed by a cost evaluation. Finally, we present our validation methodology, along with a description of the software tools and computational procedures used in the design and analysis of the aircraft.

B. Dimensioned Three-View Drawings

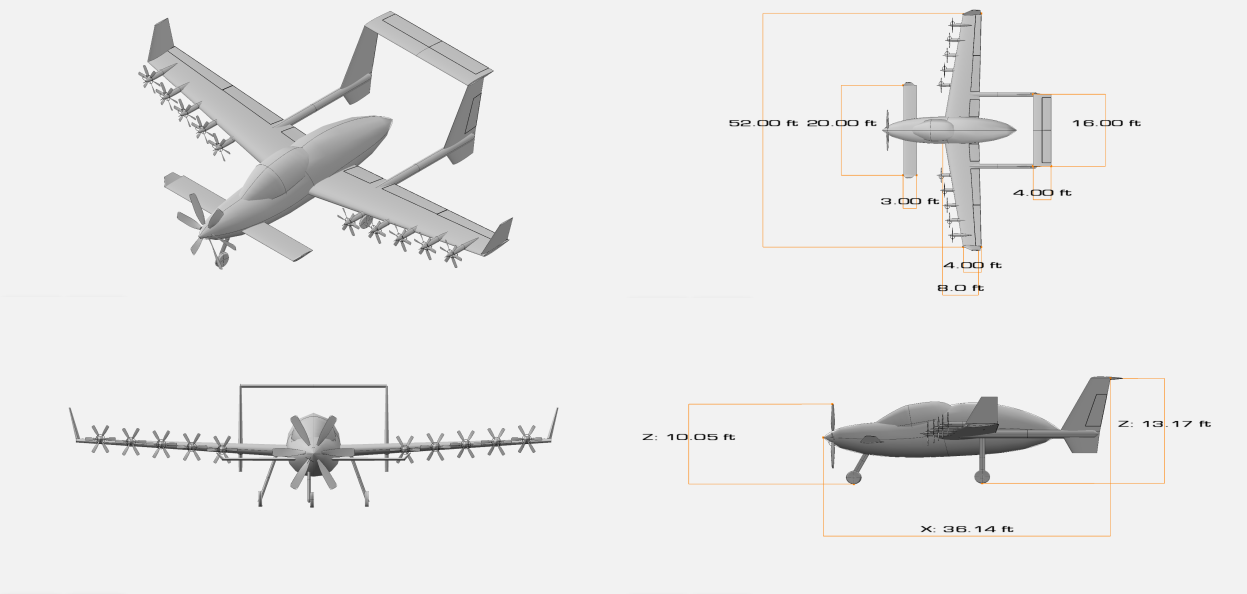

Fig. 1 Dimensioned 3-view of aircraft

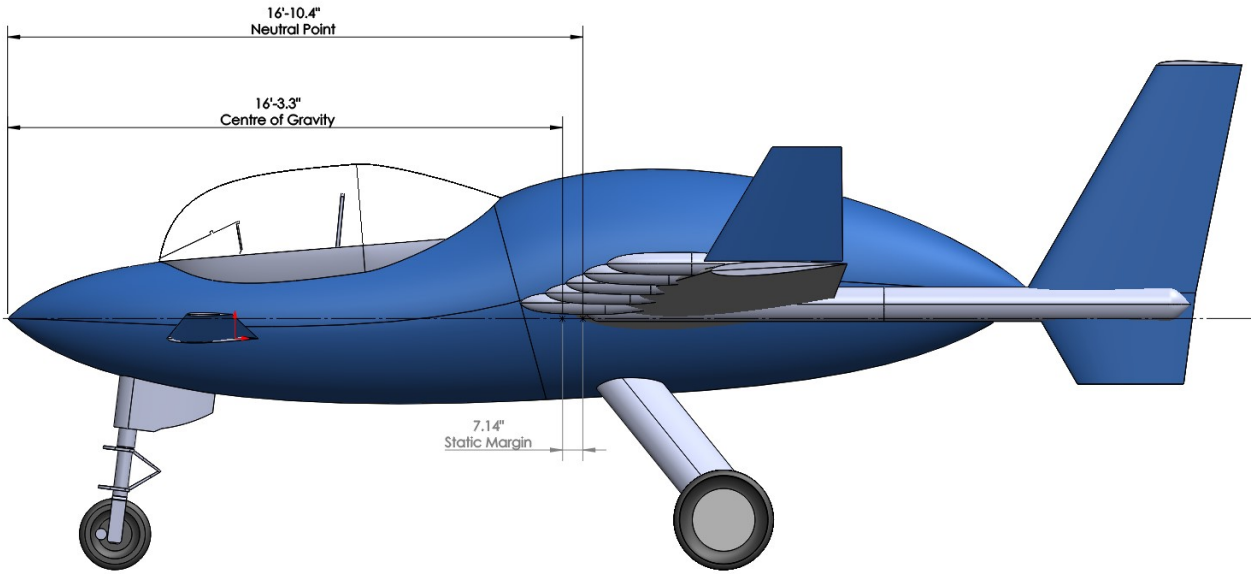

Fig. 2 Center of gravity and neutral point location

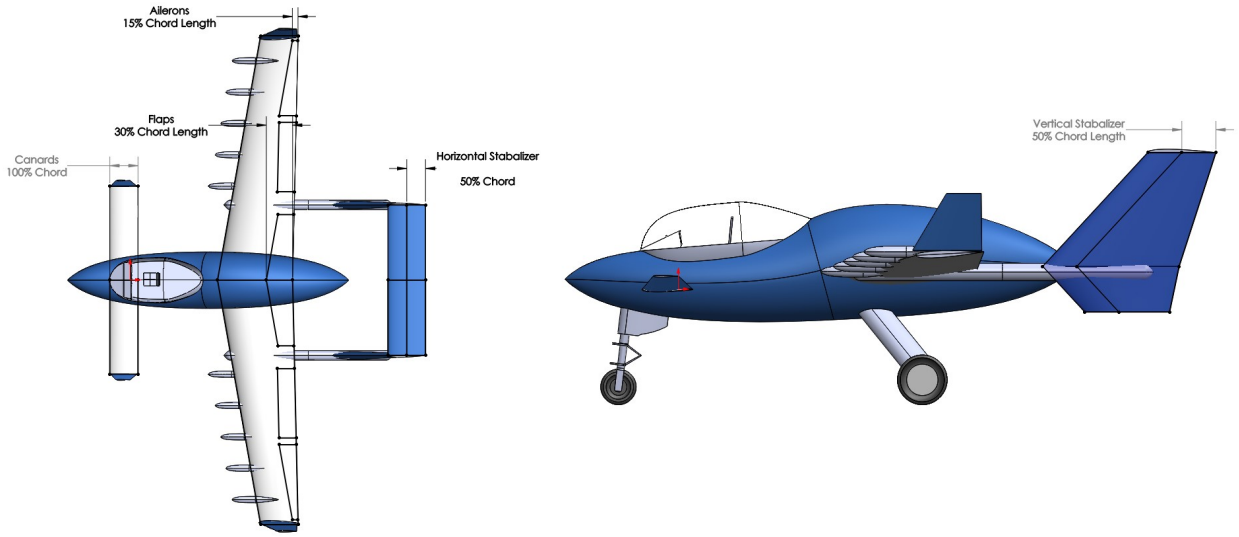

Fig. 3 Dual View Control Surfaces Sizing

C. Major Geometric and Performance Parameters

Table 1 Geometric Performance Parameters

Parameter	CD-4	AT-402B	EMB 202
Takeoff Weight (lbs)	7460	9170	3970
Empty Weight (lbs)	4843	4300	2250
Payload (lbs)	2000	5150	1650
Cruise C_L	0.4	N/A	N/A
Landing C_L	1.90	N/A	N/A
Takeoff C_L	1.90	N/A	N/A
Cruise L/D	10	N/A	N/A
Power Loading, W/P (lbs/hp)	11.0	13.5	12.4
Wing Loading, W/S (lbs/ft^2)	23.9	30	18.5
Engine Type/Architecture	Hybrid-Electric	Gas	Gas
Maximum Rated Power (SHP)	680	680	360
Engine Cruise SFC ($\frac{lbm}{hr-hp}$)	0.5	0.5	N/A
Span (ft)	52	51	38.4
Reference Area (ft^2)	312	306	215
Aspect Ratio	8.7	8.5	6.9
Average Wing Thickness Ratio, t/c	0.18	0.15	0.15
Cruise Speed (kts)	150	140	115
Maximum Range (nmi)	600	660	506
Mission Range Fuel Burn (lbs)	337	N/A	N/A
Maximum Range Fuel Burn (lbs)	984	1020	460
Number of Passengers	1	1	1
Static Margin (MTOW)	0.101	N/A	N/A
Maximum Landing Distance (ft)	1500	N/A	1345
Maximum Takeoff Distance (ft)	1500	975	1840
Fuel Type	SAF	AV1	100 Oct. 15% Eth.

II. Introduction

The agricultural aviation industry has not changed much since the 1970's, with many aircraft in service today being from this era. Farmers are the cornerstone of the world, and the agricultural aviation sector is no small part of it. With this, we have decided to focus our attention to the opportunity of modernizing the agricultural aviation sector through meeting sustainability, affordability and productivity needs of the future.

The goal of this aircraft is to detect the concentration of pests, nitrogen, or water in the field (depending on the application) using spectral cameras and then use the real-time data to automatically program the sprayer to distribute its payload only in areas of the field that require it. This will reduce the amount of spray used by the aircraft, resulting in lower costs for farmers, less environmental damage, and potential increases in crop yields. With the world population expected to increase to 9.7 billion by 2050 [1], the global food market is expected to increase by 70% [2] with fewer resources and land available today to meet these demands.

With the increase in demand for a dependable agricultural aircraft, it is crucial to ensure that our aircraft excels in environmental sustainability and affordability. As the global food demand increases and applied technology advances, competition surges in the market for effective aerial agricultural vehicles. A measured increase in crop coverage of almost 50% was measured in the United States from 2012 with 10.3 million acres to 2017 with 15.4 million acres, and these numbers are projected to continue to climb [3]. In 2023, the market value for agricultural aircraft was estimated to be about $5.5 billion USD, and is expected to surpass $9 billion USD in the following decade [4]. With the increasing demand for food and decreasing amount of land available to grow it, it is vital that we provide an aircraft that can increase the yield of current fields.

III. Configurations

The technical age of the agricultural aviation industry is relatively old and outdated, and as a result we aim to bring new technologies to minimize its carbon footprint, increase the yield of crops, and lower operating costs for farmers. The biggest difference between regular agricultural aircraft and our proposed new design would be the hybrid electrical powertrain with distributed electrical propulsion (DEP). This brings a modern efficient system to an older outdated way of producing lift, while still maintaining the usability of older systems and increasing reliability. Additionally, the vortices generated by the DEP can mix the spray in the air before it lands on the crops, allowing for a more uniform distribution. The DEP will be paired with an engine that runs on sustainable aviation fuel (SAF) to lower emissions when compared to traditional hydrocarbon based fuels[5]. There are challenges with this new technology. First is the storage of electrical energy in batteries. At the current battery density technology, batteries create a large amount of additional weight when compared to traditional hydrocarbon fuels. Additionally, the maintenance of a hybrid system is new and foreign to most farmers, and as such will have to learn to use the appropriate tools and standard operating practices. This does pose a barrier to entry for some farmers.

Novel technologies such as spectral imaging for crop nitrogen and water concentration [6][7] and artificial intelligence pest detection [8] are already being used in the agriculture industry to improve resource management. By incorporating these technologies into agricultural aircraft, there is great potential to reduce waste during aerial applications such as spraying, fertilizing, and seeding. The proposed agricultural aircraft design will incorporate these technologies for precision spraying and seeding applications over a 400-acre area, within a 25 nmi range of the take-off location. The mission profile is depicted in Figure 4

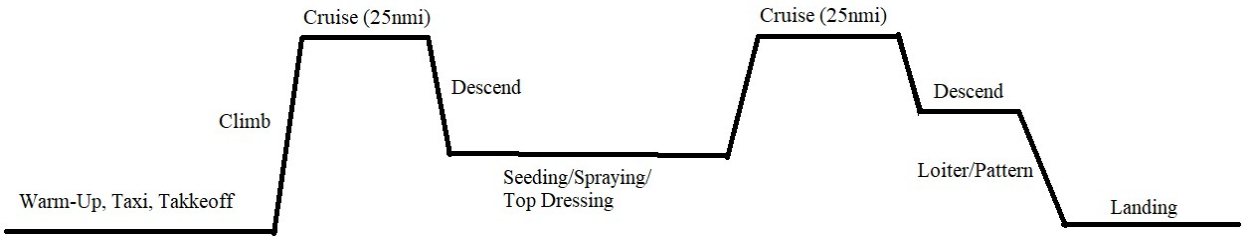

Fig. 4 Mission Profile

Three different configurations were evaluated during the conceptual design phase, each optimized for agricultural operations with varying propulsion systems and aerodynamics requirement.

A. Concept 1: Modified AT-802

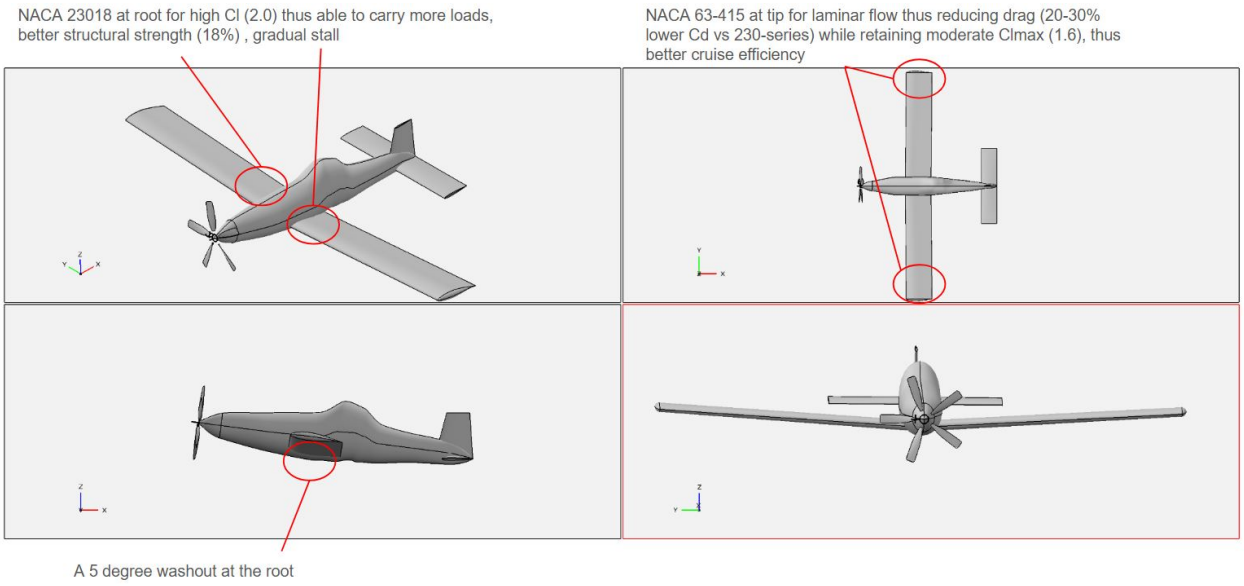

Fig. 5 Modified AT-802 Orthographic View

1. Aerodynamics:

A NACA 23018 airfoil was used at the root of the wing since it has a higher C_l (around 2.0) when compare to other popular NACA series airfoils. NACA 23018 airfoil also has relatively good stall characteristics. Agricultural aircraft need short takeoff and landing performance, and NACA 23018 provides strong lift at low speeds, which is ideal for operations in short, unpaved field. With 18% thickness-to-chord ratio, NACA 23018 airfoil provides good structural strength, allowing for strong spars and fuel storage. This factor is crucial for an agricultural aircraft since they carry heavy payloads and experiences high wing loading. For the tip of the wing, NACA 63-415 was chosen. NACA 63-415 airfoil has lower drag at cruise when comparing to NACA 23018 since it is a laminar-flow airfoil, thus it has lower profile drag. NACA 63-415 is also thinner than NACA 23018, and by using a thinner airfoil at the tip, it helps achieve a more elliptical lift distribution, thus reducing induced drag and improving aerodynamic efficiency, and this contributes to better roll stability and control during low-speed turns. By using NACA 63-415 at the tip, the wing would stall at the root first, this make stall recovery easier, which is a critical aspect for low altitude operations. Besides, with its 15% thickness-to-chord ratio, a balance between strength and weight savings is provided. Lastly, a 5 degree washout is added at the root for enhancing effectiveness, a washout can delays tip stall, reduces induced drag, and improve stability and controllability. With NACA 23018 and the root and NACA 63-415 at the tip, the modified AT-802 can carry a large amount of payload while maintaining good aerodynamic characteristics.

2. Performance:

Regarding other characteristics of the AT-802, with a high-wing monoplane configuration, there will be unobstructed downward visibility. This is essential for precise crop spraying and avoiding obstacles like trees, power lines, or uneven terrain. The high-wing configuration also has better lateral stability due to the pendulum effect, this makes controlling at low speeds and in turbulence easier. Also, spraying chemicals from a high-wing aircraft prevents residue from accumulating on the wings, fuselage, and control surfaces, which these can corrode overtime. The plane has a fixed landing gear, which is good for low-maintenance, cost, and operation. Agricultural aircraft operate from unpaved runways, dirt strips, and rough terrain, so a fixed landing gear is a good choice because it has good durability, lower maintenance costs, faster turnaround times. Fixed gear is simpler and can handle frequent short takeoffs and landing on rough surfaces. Retractable gears adds complexity, maintenance requirements, and weight, which are unnecessary for low-altitude agricultural missions. For turnaround times, there is no need to worry about gear retraction with a fixed-gear configuration, this allow quicker refueling, reloading, and takeoff cycles. The AT-802 uses a Pratt & Whitney PT6A

turboprop engine, the PT6A is one of the most widely used engines in agricultural aviation because of its reliability, power output, and ease of maintenance. It provides enough power to handle 2000+ lbs of payload while maintain good short takeoff and landing performance. The PT6A engines are known for their simple rugged design, allowing them to operate in dusty, humid, and harsh environment without significant performance loss. When comparing to piston engines, a turboprop engine like the PT6A offers better fuel efficiency for long spray runs while still giving high thrust at low speed.

B. Concept 2: EMB 202

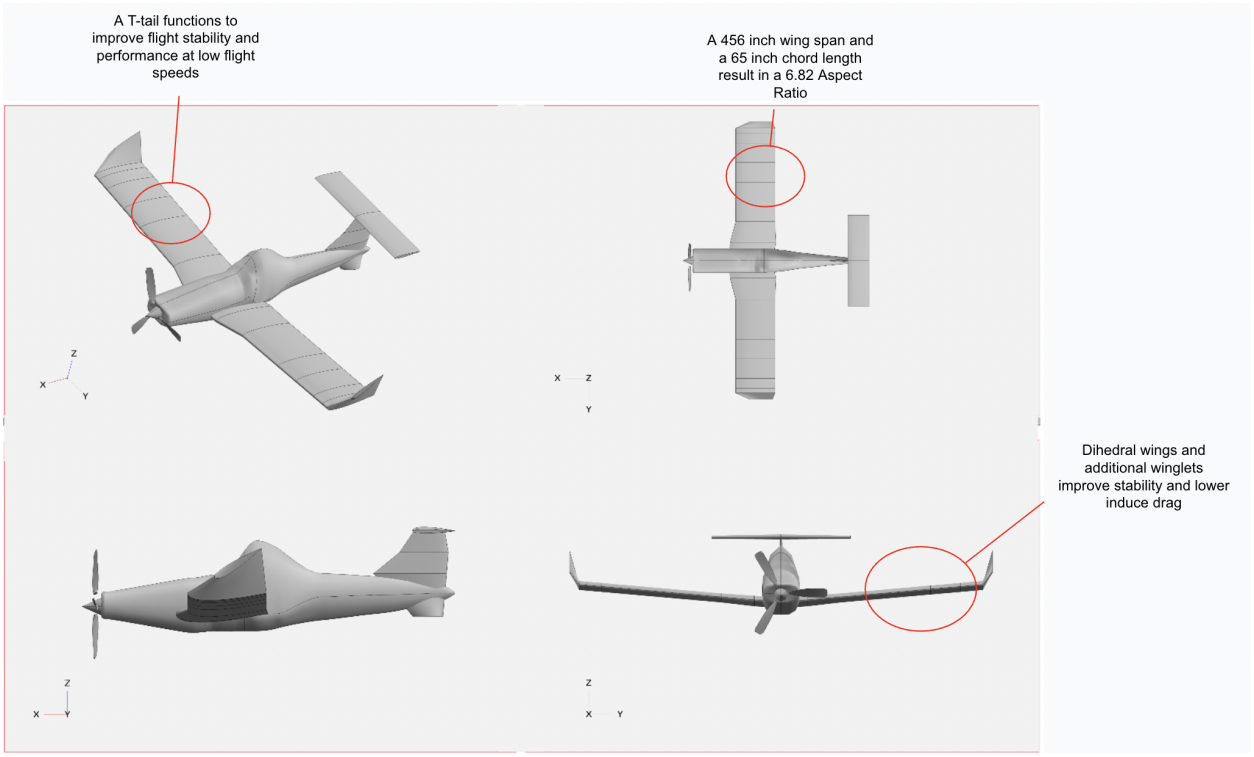

Fig. 6 EMB 202 "Ipanema" Orthographic View

1. Aerodynamics:

The Ipanema EMB 202 uses a NACA 4415 airfoil at the wing root, this helps to optimize low-speed lift generation and gentle stall behavior. This semi-symmetrical airfoil balances lift and structure strength, with a 15% thickness-to-chord ratio providing ample internal volume for fuel storage and load-bearing spars. At the tip, a NACA 63(3)-618 laminar-flow airflow minimizes profile drag during cruise, enhancing fuel efficiency. Its 18% thickness ensures compatibility with aileron integration while maintaining torsional rigidity. Winglets are also added at the tip to reduce drag and improve aerodynamic efficiency, thus improving range and endurance, allowing longer runs without refueling and reduce fuel cost over time. There is a 3 degree washout too, this ensures progressive root-to-tip stall characteristics. The high-wing with dihedral configuration add passive lateral stability is also added. The tail is modified to a T-tail for better stability and performance at low flight speeds.

2. Performance:

The Ipanema uses a Lycoming IO-540-N2A5 piston engine, delivering 300 hp at 2700 RPM, optimized for short-field operations.

C. Concept 3: Electric Long EZ and Airtruk Combination

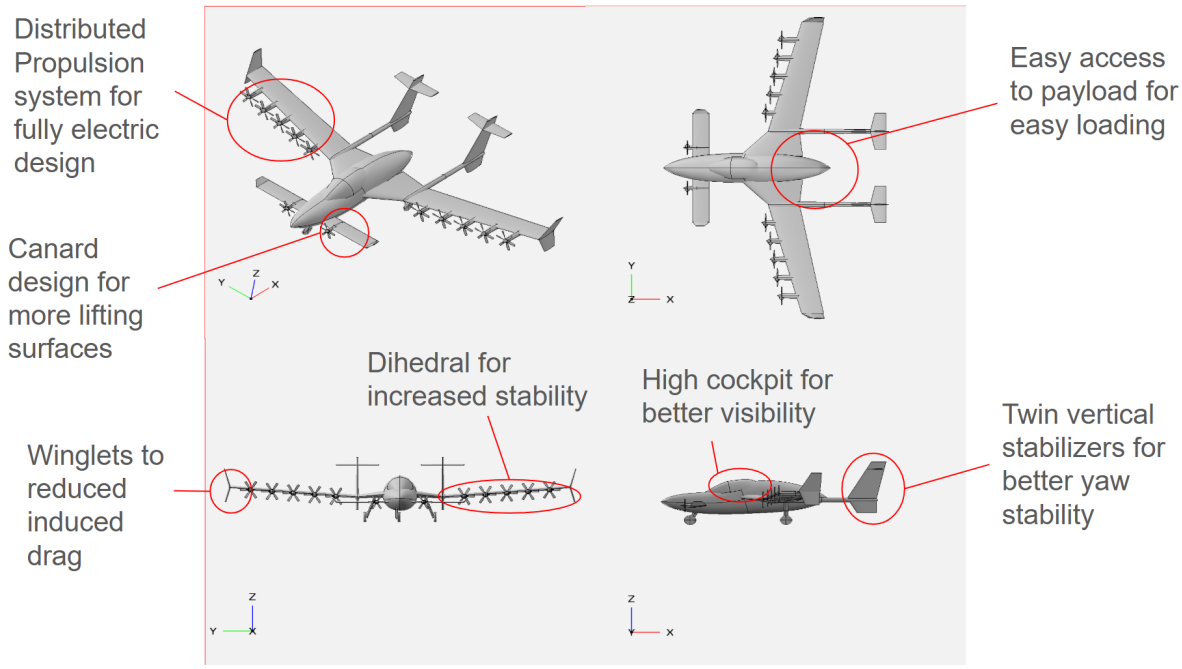

Fig. 7 Custom "Cybertruk" Orthographic View

1. Aerodynamics:

The Cybertruk has a delta-wing configuration, thus the entire wing-body structure is more integrated, making the aircraft stronger and more durable, and technically there is no need for a horizontal tail. With the delta wings, strong leading-edge vorticies are created, generating lift even at high angle of attacked, this could improve low-speed handling and short-field takeoff performance. Also, the delta wings provides ample internal space, which could allow bigger chemical tanks or more fuel capacity for extended missions. At the tip of the wings, winglets are added to suppress vortices, thus induced drag is reduced. There is a dihedral angle added to the wings too, this help with increasing lateral stability, making the aircraft self-correcting in roll, this make the aircraft self-stabilize better, reducing down the workload of the pilots since they do not have to make constant roll corrections. At the tip of the aircraft, there are two canards added for more lifting surfaces and stall resistance since when a stall happen, it would happens at the canard before the main wing, this lower the nose gently instead of the aircraft enter a deep stall. The canard also helps lift the nose earlier during takeoff, thus a shorter runaways is needed. A twin vertical stabilizer configuration is used for the empennage, the main reason is this configuration make loading and unloading process of the payload bay easier since the payload bay is at the back of this aircraft, allowing for faster loading, unloading process and shorter preparation time. The twin vertical stabilizers also increase yaw stability.

2. Performance:

The Cybertruk uses a distributed electric propulsion system with five engines at each wing and two more engines at the canard. This system enables short takeoff and landing performance through thrust vectoring during takeoff. Each motor operates independently, allowing asymmetric thrust compensation for crosswind landings. Since the propulsion system is fully electric, the amount of carbon footprint the aircraft produce is also reduced dramatically, making this aircraft environmentally friendly.

D. Materials

Besides the three different aircraft configurations above that were used during the conceptual design, a deeper look into material option was also made.

1. Aluminum Alloys:

Aluminum dominates agricultural aircraft due to its high strength-to-weight ratio, which reduces fuel consumption during operation. However, its production is energy intensive, emitting 10-15 kg CO_2 / kg of aluminum. While recycled aluminum slashes emissions by 95%, initial production remains carbon-heavy. In service, aluminum's corrosion resistance (when coated) and ease of repair lower maintenance costs, as damaged sections can be welded using standard techniques. Yet, untreated surfaces risk pitting from agrochemicals, increasing inspection frequency. Over decades, fatigue cracks from low-altitude turbulence may necessitate airframe replacements, raising long-term costs. At end-of-life, aluminum's 100% recyclability supports circular economies, mitigating disposal expenses [9].

2. Steel Alloys:

Steel's superior tensile strength makes it ideal for landing gear and joints, but its weight penalizes fuel efficiency. Production emits less CO_2 than aluminum (1.85 kg CO_2/kg steel), yet operational emissions rise due to higher fuel consumption. Steel components endure rough airstrips well but require corrosion-resistant coatings to combat rust from agrochemicals and mud. Maintenance involves frequent inspections for cracks and lubrication, with galvanized coatings complicating recycling. Though 90% of steel is recycled globally, its weight-driven fuel inefficiency and shorter service life under abrasive conditions offset sustainability gains [10].

3. Fiberglass Composite:

Fiberglass composites provide a lightweight yet durable solution for agricultural aircraft, enhancing payload capacity and fuel efficiency, this also allow for more diverse mission profiles. Their corrosion resistance makes them ideal for chemical-intensive environments, extending aircraft lifespan while reducing maintenance. Unlike metals, fiberglass resists fatigue cracking, improving structural longevity. However, repairs require specialized skills and materials, increasing downtime and costs. Exposure to UV radiation and moisture can lead to degradation, necessitating protective coatings and periodic inspections. While fiberglass improves aerodynamic efficiency and operational durability, its higher initial costs and recyclability challenges remain barriers to widespread adoption in primary airframe structures [11].

E. Final Selected Configuration

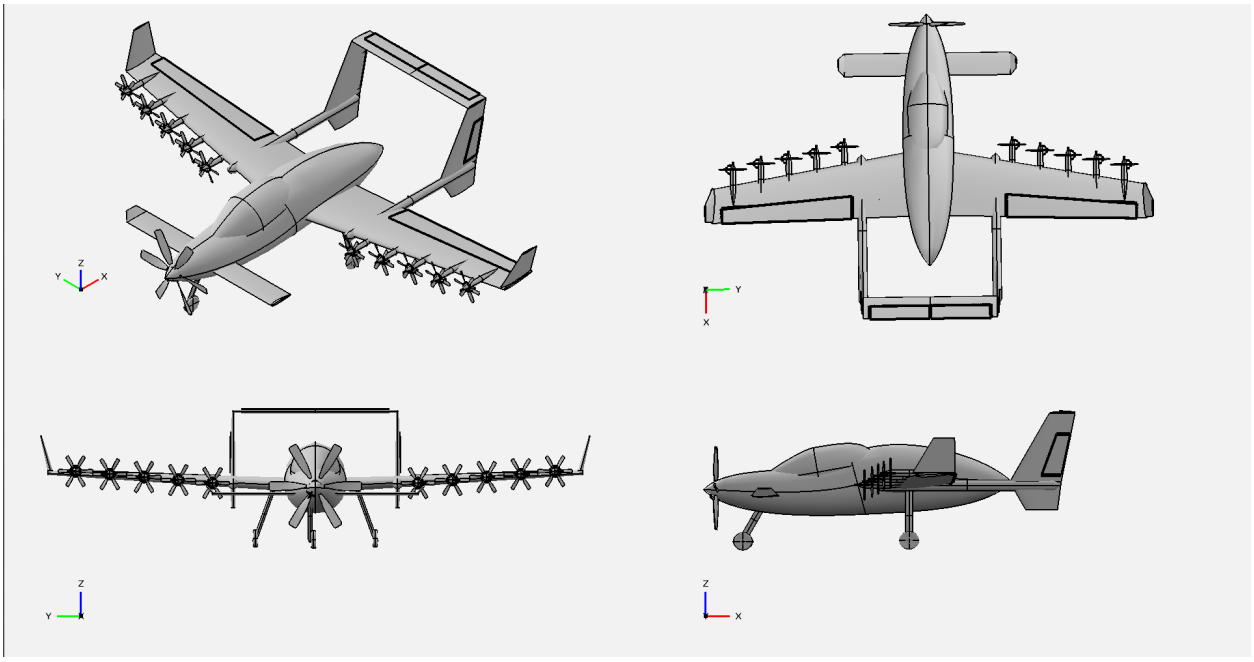

Fig. 8 Final selected configuration "CD-4" CyberTruk

1. Spectral Imaging and AI:

Spectral imaging and AI revolutionize precision agriculture by enabling real-time crop health assessment, early disease detection, and optimized resource allocation. Spectral cameras onboard agricultural aircraft capture multi-spectral and hyperspectral data, identifying nutrient deficiencies, water stress, and pest infestations before they become visible to the human eye. AI-driven analytics process this data to generate targeted treatment maps, ensuring precise pesticide, fertilizer, and water applications, minimizing environmental impact while maximizing yield. Additionally, machine learning models continuously refine intervention strategies, adapting to changing weather, soil conditions, and crop growth patterns. By integrating AI with spectral imaging, agricultural aircraft enhance efficiency, sustainability, and profitability, reducing waste and input costs while improving overall farm productivity.

2. Fiberglass Composite:

Despite fiberglass composites requiring specialized skills and materials to repair, thus increasing downtime and cost, they are much lighter when compared to steel or aluminum. This could allow for the AirTruk to carry more payload if needed. Additionally, agricultural aircraft work in a chemical-intensive environment, and with fiberglass composite's corrosion resistance characteristics, the lifespan of the aircraft would be increased and required maintenance would decrease.

3. Distributed Lift with Hybrid Powertrain:

At the beginning, a fully electric powertrain was considered, but even with an assumed battery energy density of 500 Wh/kg, this concept is simply not efficient. The weight of the batteries is excessive and take up a lot of volume within the plane. A 50-50 hybrid configuration was considered instead, however the battery and motor size were decided to still be too large, as discussed in trade study in the powertrain section of this report. The final decision was made to lower the hybridization ratio to 10% and only use the DEP during flight conditions where maximum power is needed, such as takeoff, climb, and sustained turns.

4. Boom-tail:

The boom-tail was developed from the twin vertical stabilizers from the custom CyberTruk concept design. A boom tail design would give the aircraft better yaw stability, making them more stable at low altitude and speeds. The widely spaced tail reduces side forces caused by wind gusts. With separate booms, the payload bay can be accessed easier, allowing for faster loading and unloading times.

5. Canard:

Canards were added to generate additional lift near the front of the aircraft. This allows for additional pitch control by shifting the neutral point forward (NP) when there is little to no payload in the hopper and the center of gravity (CG) is near the front.

6. High Cockpit:

Since agricultural aircraft operate at low altitudes, perform tight turns, and use rough airstrips, a high-wing, high-cockpit design is essential for safety and visibility. A high cockpit position gives the pilot a clear downward view of the spraying area, and it also gives the pilot better surrounding visibility to spot obstacles like trees and power lines.

7. Rear Hopper

The rear placement of the hopper was to limit the exposure of the pilot to toxic chemicals, as requested by the RFP. This placement in combination with the boom-tail allows for ease of access when loading payload by truck.

IV. Preliminary Sizing

A fully electric and a 50% hybrid configuration were analyzed during the preliminary sizing. Sizing constraints such as stall, takeoff field length, landing field length, climb, cruise, ceiling, and a sustained turn maneuver were considered when building the constraint diagram.

A. Stall Speed

The maximum stall speed was set to 100 kts, based on the maximum stall speed requirement in the RFP. Based on Table 3.1 in Roskam [12], the estimated $C_{L_{max}}$ value range for agriculture aircraft is estimated to be from 1.3 to 1.9. Atmospheric density is from an average cruise height of 8,000 ft, based on the average cruise altitude of common agriculture aircraft such as the AT-802 or AT-402B [13]. The wing loading ($\frac{W}{S}$) from stall speed is estimated from Equation (1).

$$\frac{W}{S} = \frac{1}{2}\rho v_{stall}^2 C_{L_{max}} \tag{1}$$

B. Takeoff

Level ground roll distance (s_{TO_G}) and obstacle clearance distance (s_{TO}) are taken from the RFP to be 1000 ft and 1500 ft, respectively. The takeoff parameter from FAR 23 (TOP_{23}) is estimated using s_{TO} by solving for the non-extraneous roots in Equation (2) from Roskam [12].

$$s_{TO} = 8.134\,(TOP_{23}) + 0.0149\,(TOP_{23})^2 \tag{2}$$

The $\frac{W}{P}$ for takeoff is a function of TOP_{23}, ρ, and $C_{L_{max_{TO}}}$. $C_{L_{max_{TO}}}$ is estimated to be the same range based on values from Roskam Table 3.1. The takeoff altitude is estimated to be 5,000 ft, which will determine what power loading is needed at higher take off elevations. Atmospheric density at this altitude is $2.048 * 10^{-3}\ \frac{slugs}{ft^3}$. Equation (3) is used to calculate power loading ($\frac{W}{P}$) as a function of $\frac{W}{S}$.

$$\frac{W}{P} = \frac{(TOP_{23})\left(\frac{\rho_{TO}}{\rho_{SL}}\right) C_{L_{max_{TO}}}}{\frac{W}{S}} \tag{3}$$

C. Landing

Balanced field length is calculated using Equation 4.15 in the Metabook from the estimated TOP_{23} value of 149.549519 $\frac{lb}{ft^2}$

$$TOP = \frac{BFL}{37.5} \tag{4}$$

S_{land} is calculated using Equation (5) to comply with FAR 23 requirements. S_a is assumed to be 600 ft for general aviation

$$S_{land} = (BFL)\,0.6 \tag{5}$$

Assuming the average cruise altitude is 8,000 ft, the atmospheric density at this altitude is $1.8685 \times 10^{-3}\frac{slugs}{ft^3}$. The $\frac{W}{S}$ from the landing constraint is estimated using Equation (6) from with estimated values $C_{L_{max}}$ ranging for agriculture aircraft from 1.3 to 1.9. Maximum landing to takeoff weight ratio is assume to be 0.88, which is in the middle for the range from 0.85 - 0.95 for agricultural aircraft from Table 3.3 in Roskam[12].

$$\frac{W}{S} = \frac{\left(\frac{\rho}{\rho_{SL}}\right) C_{L_{\max}}}{80 \times 0.88}\,(S_{\text{land}} - S_a) \tag{6}$$

D. Climb

To calculate climb, there are 3 different segments in the FAR 23 airworthy requirements. Considering our aircraft is a Level 1 low-speed aircraft, we can use the following parameters:

We can then use these parameters in the following equation to calculate the power loading of the different cases:

$$W/P = \left(\frac{G + (L/D)^{-1}}{C_L^{1/2}} \frac{(W/S)^{1/2}}{18.97\eta_P(\rho/\rho_{SL})}\right)^{-1} \tag{7}$$

In this case, we assume that case 1 and 3 are taken at sea level, while case 2 is at 5000 ft.

Table 2 Climb Parameters

Parameter	Case 1	Case 2	Case 3
G	8.3%	1.5%	3%
k_s	1.2	1.2	1.3

Case 2 also asks for one engine inoperable, since our aircraft has 1 engine and 10 motors, we can use the following correction:

$$\left(\frac{P}{W}\right)_{takeoff} = \left(\frac{N_{engines}}{N_{engines}-1}\right)\left(\frac{W}{W_{takeoff}}\right)^{3/2}\left(\frac{P}{W}\right) \tag{8}$$

We also assume that in all the cases, that the payload would be dumped, except for case 1, where the takeoff weight would equal the current weight.

From there, the power loading for climb as a function of wing loading can be plotted using Equation (7) and correction (8).

E. Cruise

Our aircraft is a propeller aircraft, so we can use the following equation to calculate the power loading at cruise:

$$\left(\frac{W}{P}\right)_{cr} = \left[\frac{q_{cr}v_{cr}\left(C_{D0} + \frac{k\left(\frac{W}{S_{ref}}\right)^2}{q^2_{cruise}}\right)}{550\eta_p\frac{W}{S_{ref}}} \cdot \left(\frac{P_{TO}}{P_{cr}}\right)\right]^{-1} \tag{9}$$

Using Equation (9), we can plug in the aircraft parameters that were calculated in the previous sections. However, we first need to determine the value of k, or the induced drag factor. The formula for the term is as follows in Equation (10)

$$k = \frac{1}{\pi e AR} \tag{10}$$

The takeoff-to-cruise power ratio can be calculated using a density correction factor seen in Equation (11).

$$\frac{P_{TO}}{P_{cr}} = \left(\frac{\rho_0}{\rho_{cr}}\right)^{\frac{3}{4}} \tag{11}$$

If we assume a maximum cruising speed of 150 knots, then we get the following parameters:

Table 3 Cruise Parameters

Parameter	Value
C_{D_0}	0.036389
k	0.04198
η_p	0.8
V_{cr}	150 knots

F. Ceiling

To determine the ceiling of flight, we want to determine the minimum possible Thrust over Weight, maximizing the lift to drag ratio. There is a service ceiling as well as an absolute ceiling. The absolute ceiling is when the maximum rate of climb is zero, making it the highest possible altitude for the aircraft. The service ceiling has a max rate of

climb of 100 $\frac{ft}{min}$. However, in this case, our active constraint is the absolute ceiling. For our airplane, the designed absolute ceiling is 25,000 ft of elevation, given from the FAR 23 conditions. At this elevation, we need to determine the minimum thrust to weight ratio. The formula is given as follows in Equation (12)

$$\left(\frac{T}{W}\right)_{min} = 2\sqrt{kC_{D,0}} \tag{12}$$

We already know the value of the zero lift drag coefficient. Based off Equation (10) earlier, the induced drag factor was determined to be k = 0.04198. With the k value, we determined the minimum thrust to weight ratio to be as follows:

$$\left(\frac{T}{W}\right)_{min} = 0.0557$$

With the thrust to weight ratio, the last step is to convert it to weight over power. The conversion to weight to power is as follows:

$$\frac{W}{P} = \frac{\eta_p}{V}\frac{W}{T} \tag{13}$$

The weight to thrust term is the inverse of the minimum ratio that was just determined. Furthermore, it was given from Table 2 that the propellor efficiency is 0.8. In order to determine the velocity component, the Equation (14) was used:

$$V = \sqrt{\frac{2}{\rho C_{L_{condition}}}\frac{W}{S_{ref}}} \tag{14}$$

ρ was determined from the elevation charts at 25,000 ft to be $\rho = 0.0343\frac{lb}{ft^3}$. We determined the lift coefficient to be 0.66366 from the following equation:

$$C_{L_{condition}} = \sqrt{\frac{C_{D,0}}{k}} \tag{15}$$

G. Maneuver

A sustained turn was selected to be analyzed as a maneuver, an important design criteria for top dressers and most agricultural planes. A 45 degree bank angle was selected to allow for tight turns while not structurally overloading the aircraft. A maneuvering speed of 110 knots was selected based on the average working speed of comparable aircraft such as the AT402B, which has a working speed of 104 to 122 knots[14]. Equation (16) is used to calculate the load factor acting on the aircraft at the set bank angle.

$$n = \sqrt{(\frac{\dot{\phi}V}{g})^2 + 1} \tag{16}$$

From Equation (17), the required $\frac{T}{W}$ requirement is calculated as a function of $\frac{W}{S}$.

$$\frac{T}{W} = \frac{qC_{D_0}}{W/S_{ref}} + k\left(\frac{n}{q}\right)^2 \left(W/S_{ref}\right) \tag{17}$$

Equation (13) is used to convert $\frac{T}{W}$ to $\frac{P}{W}$.

H. Total Power Loading Graph

By overlaying all the constraints onto one graph, the optimal sizing for the aircraft can be determined. The goal is to maximize the wing loading while minimizing power loading in order to require the smallest wing area and power output. The feasible region lies below all of the constraint lines and to the left of the stall line.

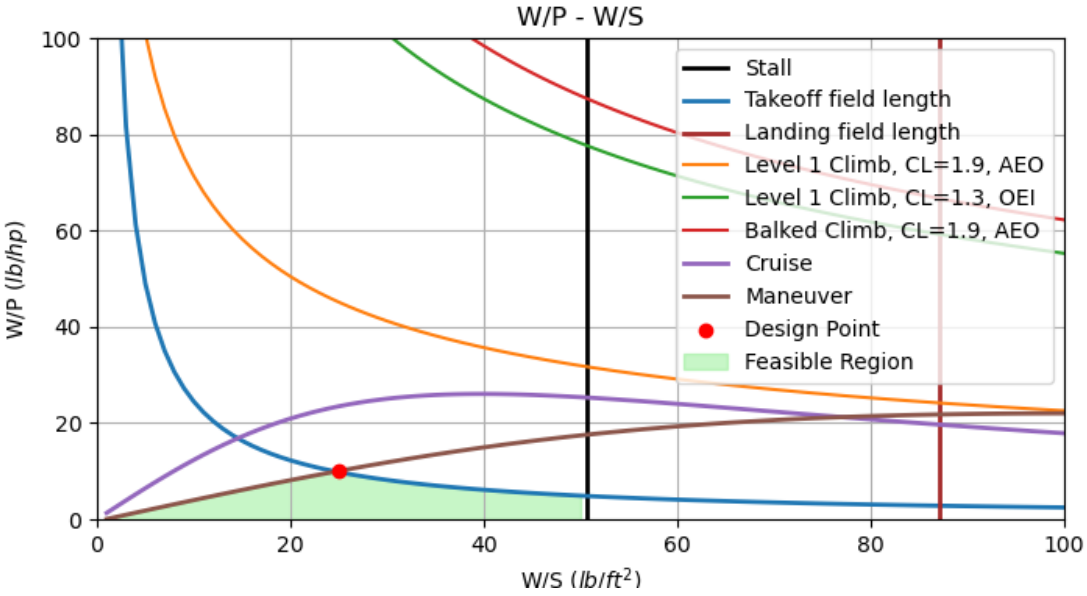

Fig. 9 Complete constraint graph with feasible region shaded and design point selected

The active constraints from the graph are maneuver, takeoff field length, and stall speed. The selected point maximizes both the wing loading while minimizing power loading, resulting in a wing loading of 25 $\frac{lbf}{ft^2}$ and a power loading of 10 $\frac{lbf}{hp}$. Due to battery and electric motor weight being a large contributing factor to the overall weight of the aircraft, the best option for this design is to minimize the required output of the plane, resulting in a smaller and lighter powertrain system.

I. Component Power Loading

The selected powertrain design is a parallel-series hybrid design. The components are given as follows: Propeller (P), Electronic Motor (EM), Power Manager (PM), Gas Turbine (GT), Gear Box (GB), Battery (BAT), and Fuel (F). Further analysis on component efficiencies and performance would be described in the propulsion system section. The efficiencies for P, EM, PM, GT, and GB are known. These cover seven of the components in the hybrid powertrain; however, to determine all ten power values, three additional equations are required to complete the system of linear equations. These final three equations are derived from the shaft ratio (ϕ), the supplied ratio (Φ), and the total propeller power (P_p). The ten governing equations are as follows:

$$P_{gt} = \eta_{gt} \times P_f \tag{18}$$

$$P_{s1} + P_{gb} = \eta_{gb} \times P_{gt} \tag{19}$$

$$P_{p1} = \eta_{p1} \times P_{s1} \tag{20}$$

$$P_{e1} = \eta_{em} \times P_{gb} \tag{21}$$

$$P_{e2} = \eta_{pm} \times (P_{e1} + P_{bat}) \tag{22}$$

$$P_{s2} = \eta_{em} \times P_{e2} \tag{23}$$

$$P_{p2} = \eta_{p2} \times P_{s2} \tag{24}$$

$$\phi_{shaft} = \frac{P_{s2}}{P_{s1} + P_{s2}} \tag{25}$$

$$\Phi = \frac{P_{bat}}{P_{bat} + P_f} \tag{26}$$

$$P_p = P_{p1} + P_{p2} \tag{27}$$

When the power loading equations were solved and the previously selected design point was input, the batteries produced the lowest power loading values of all the components. For this reason, the batteries of the fully electric and hybrid configurations were selected for component power loading graphs. The power loading graphs for the battery in the fully electric and hybrid configurations can be seen in Figures 10 and 11, respectively.

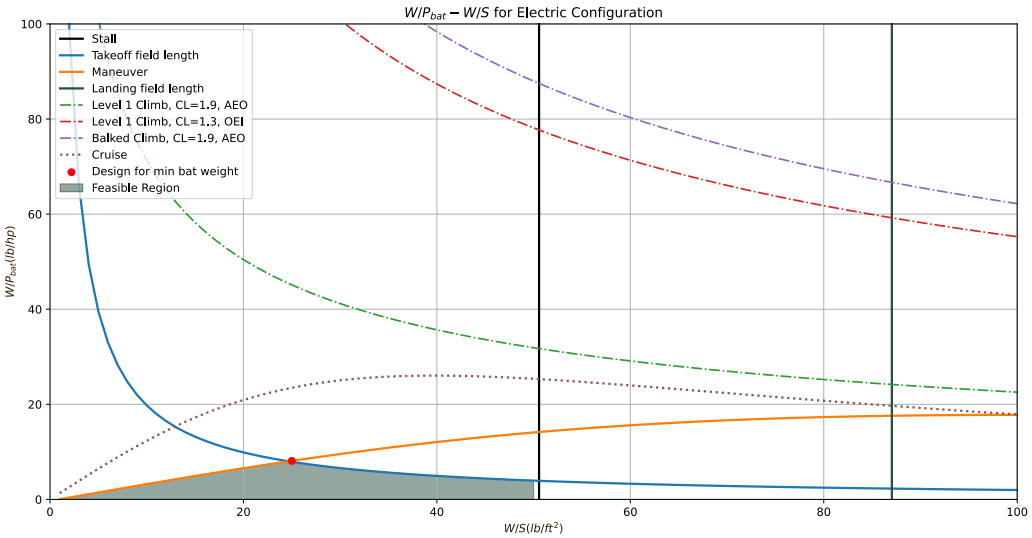

Fig. 10 Electric Battery Power Loading

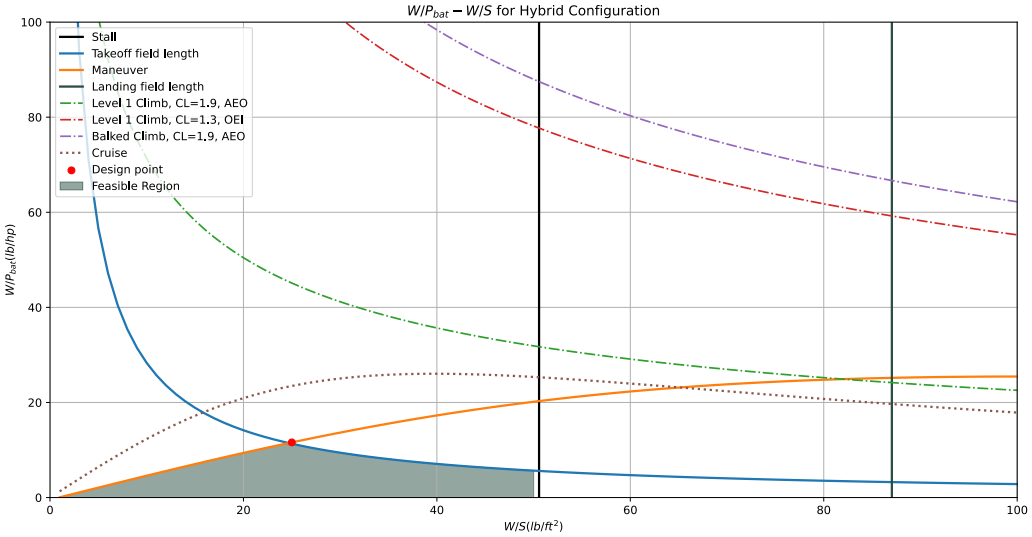

Fig. 11 Hybrid Battery Power Loading

J. Dimensioned Constraint Graphs and Final Design Point

Using the estimated weights from the weight estimation code for the fully electric and hyrbid configurations (12200 lb and 7460 lb, respectively), a power vs loading plot was created for each configuration.

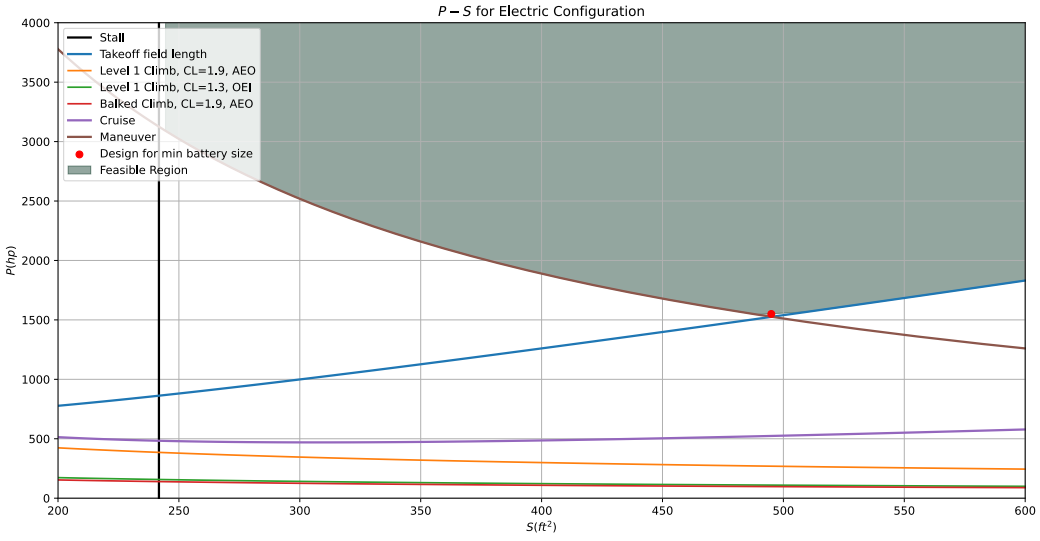

Fig. 12 Electric Power vs Area

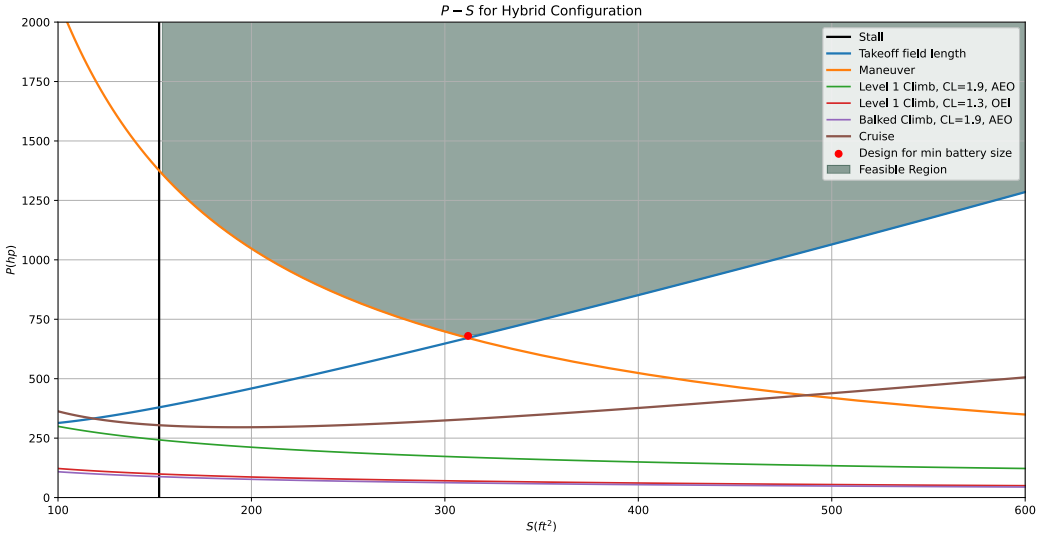

Fig. 13 Hybrid Power vs Area

Looking at both plots, it is clear that the hybrid configuration requires less wing area and less power to fly than the fully electric configuration. The electric configuration requires a wing area of almost 500 ft^2 and a required power of over 1500 hp, while the hybrid configuration only requires a wing area 312 ft^2 and a power output of 670 hp. Since a lower required power output means less batteries and smaller engines/motors, the hybrid configuration was selected to save on weight. This is why the design point that minimized the required power was selected, even though it wasn't the smallest wing area.

V. Weights and Center of Gravity

A. Powertrain

The powertrain design utilizes a hybrid electric propulsion system. With two separate power sources, there are many segmented components that are incorporated into the power train design. The components that are the most significant contributes are the battery, the fuel and oil, the gas engine, and the electric motors. The component locations are shown below in Figure 32. Notably, the figure shows many electrical components included in the aircraft. The electrical components are the high and low voltage wires, the fuel lines,and the voltage controller and converter. These components will be covered further sections.

The gas engine being used on the CD-4 is a preexisting engine where the engine weight is given. The Pratt & Whitney PT6A-15AG engine that is used on the AT-402B was selected for the aircraft since it produces 680 hp, meeting the power requirements deemed in the sizing. This would allow the aircraft to run solely on the gas engine in phases of flight such as cruise that do not need to use DEP. This engine has an estimated weight of around 320 lbs, including the weight of the gearbox. The distributed propulsion engines are preexisting motors that have their weights given along with the propellers. Currently, Lilium, an eVTOL company, is making prototype electric motors for their distributed propulsion system. Each motor weights about 10 lbs [15], and considering our aircraft has 10 distributed motors, it is assumed that the total weight added by the electric propulsion motors is around 100 lbs.

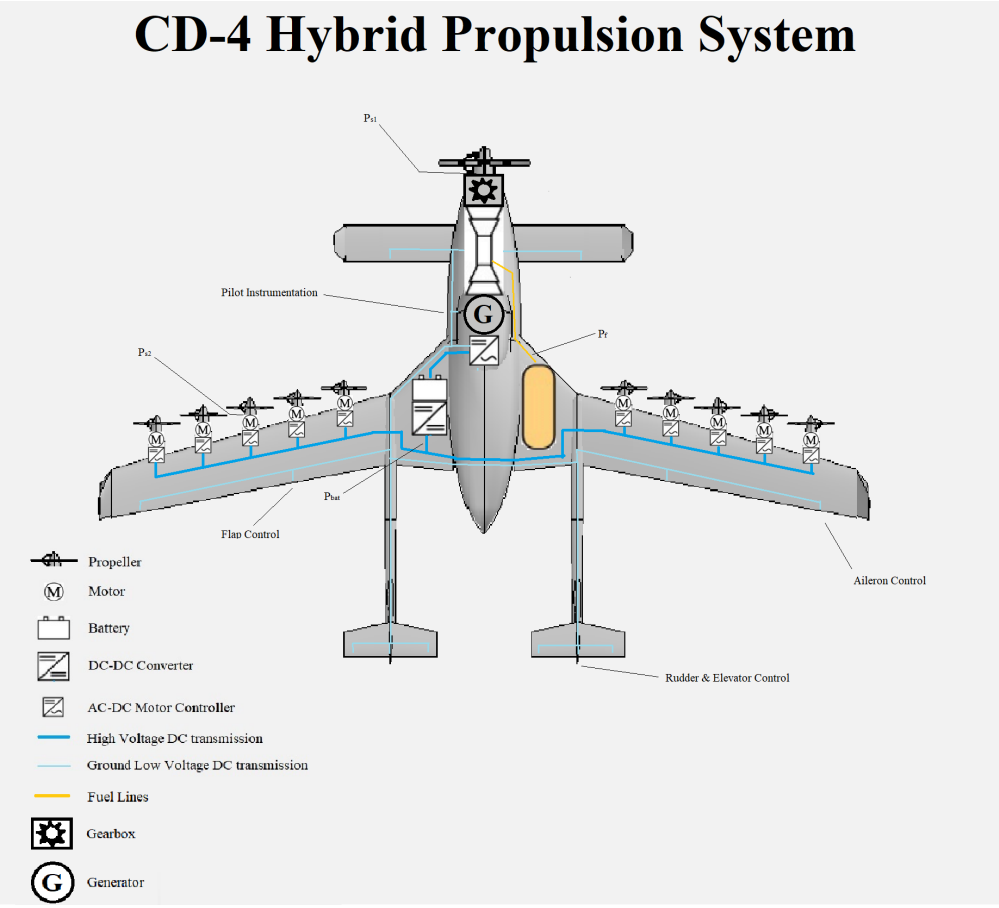

Fig. 14 Hybrid Electric Propulsion

B. Airframe Structure

Using the equation for general aviation aircraft, the weight of the wing is estimated to be 160 lbs. The equation is as follows:

$$W_{wing} = 0.036 S_w^{0.758} W_{fw}^{0.0035} \left(\frac{A}{cos^2\Lambda}\right)^{0.6} q^{0.006} \lambda^{0.04} \left(\frac{100t/c}{cos\Lambda}\right)^{-0.8} (N_z W_{dg})^{0.49} \tag{28}$$

It is then solved as:

$$W_{wing} = 0.036(312ft^2)^{0.758}(1050lbs)^{0.0035}\left(\frac{8.7}{\cos^2(10^\circ)}\right)^{0.6}(76.21\frac{lbs}{ft^2})^{0.006}(0.5)^{0.04}\left(\frac{100(0.18)}{\cos(10^\circ)}\right)^{-0.8}(4.4{\cdot}8800lbs)^{0.49}$$

$$W_{wing} = 185lbs \cdot 0.86 = 160lbs$$

The weight of the horizontal and vertical tails can be estimated using two separate equations:

$$W_{horizontal-tail} = 0.016(N_z W_{dg})^{0.414} q^{0.168} S_{ht}^{0.896} \left(\frac{100t/c}{\cos\Lambda}\right)^{-0.12} \tag{29}$$

$$W_{vertical-tail} = 0.073\left(1 + 0.2\frac{H_t}{H_v}\right)(N_z W_{dg})^{0.376} q^{0.122} S_{vt}^{0.873} \left(\frac{100t/c}{\cos\Lambda_{vt}}\right)^{-0.49} \tag{30}$$

Using Equations 29 and 30, we can find the total weight of the empennage and the canard:

$$W_{horizontal-tail} = 0.016((4.4)\cdot(8800lbs))^{0.414}(76.21\frac{lbs}{ft^2})^{0.168}(40ft^2)^{0.896}\left(\frac{100(0.12)}{\cos(0^\circ)}\right)^{-0.12}$$

$$W_{horizontal-tail} = 46lbs$$

$$W_{vertical-tail} = 2\cdot 0.073\,(1+0.2(1.0))\,((4.4)\cdot(8800lbs))^{0.376}\,(76.21\frac{lbs}{ft^2})^{0.122}(35.8ft^2)^{0.873}\left(\frac{100(0.12)}{\cos(30^\circ)}\right)^{-0.49}$$

$$W_{vertical-tail} = 98.9lbs \cdot 0.86 = 85lbs$$

$$W_{canard} = 0.016((4.4)\cdot(8800lbs))^{0.414}(76.21\frac{lbs}{ft^2})^{0.168}(53.3ft^2)^{0.896}\left(\frac{100(0.18)}{\cos(0^\circ)}\right)^{-0.12}$$

$$W_{canard} == 56lbs$$

The fixed gear landing system can be calculated using the following equation:

$$W_{main-landing-gear} = 0.095(N_l W_l)^{0.768}(L_m/0.12)^{0.409} \tag{31}$$

$$W_{nose-landing-gear} = 0.095(N_l W_l)^{0.566}(L_n/0.12)^{0.845} \tag{32}$$

Solving Equations 31 and 32, we get the following results:

$$W_{main-landing-gear} = 0.095((1.5)(8800lbs))^{0.768}((5.7ft)/0.12)^{0.409}$$

$$W_{main-landing-gear} = 580lbs$$

$$W_{nose-landing-gear} = 0.095((1.5)(8800lbs))^{0.566}((3.3ft)/0.12)^{0.845}$$

$$W_{nose-landing-gear} = 290lbs$$

The fixed equipment onboard, such as the furnishings for the cockpit, can be taken as a function of the gross weight:

$$W_{fixed-equipment} = 0.0582 \cdot W_{dg} - 65 \tag{33}$$

Using Equation 33, this gives a fixed equipment weight of roughly 450 lbs.

To find the weight of the fuselage, it can be compared to existing aircraft. Since the fuselage of the CD-4 is heavily inspired by the Long EZ, we can take the weight of that fuselage and scale it to match with the CD-4. The Long-EZ fuselage weighs 710 lbs and has a length of 16 feet, while the CD-4 has a length of 30 feet. Considering the skin of the aircraft would increase by a factor of 4 (due to the area increasing by a squared term), we can estimate the CD-4's fuselage weight to be around 2800 lbs.

C. Control System

As shown in Figure 32, our aircraft has a system that uses high voltage DC wiring, ground low voltage DC wiring, in addition to 11 AC-DC motor controllers, in addition to a DC-DC converter for the battery. Although little, these components still contribute weight to the aircraft and affect the center of gravity. In a study published to the Society of Allied Weight Engineers [16], the total weight of wiring within an aircraft amounts to 1-2% of the empty weight of the plane. With an empty weight amounting to 4843 lbs, we expect about 95 lbs or wiring in our aircraft. Our aircraft contains a DC-DC converter as well as 11 AC-DC controller. These electronics are generally lightweight, with typical market converters like the KOP130-420 [17] weighing roughly 5 lb and the controllers like the SDM-CD16ACA [18] each weighing roughly 4 lb amounting to a total weight of 44 lb. Finally,our aircraft contains a fuel line from our fuel storage to our engine. The weight is largely negligible due to lightweight material.

D. Payloads

The crew and payload weights are already given in the RFP requirements. The crew contains only a single pilot with an average weight of around 160 lbs with no additional passengers. The payload capacity is also given at a strict 2000 lbs requirement.

E. Fuel

An updated fuel weight estimation was done to determine more accurate fuel fractions at each flight condition. Calculations were performed for both the standard mission with payload and the ferry mission without payload to determine the amount of fuel required for each configuration. For taxi and takeoff, the fuel fractions for each were estimated using Equation (34). The taxi was estimated for 15 minutes to account for startup and warm up while at 5% power. The takeoff was estimated for 1 min at maximum power.

$$\frac{W_{i+1}}{W_i} = 1 - t\frac{c}{\eta}(\frac{P_A}{W})_i \tag{34}$$

The climb condition was discretized into 10 separate segments while climbing to 8000 ft. A loop function was used to calculate the climb velocity and change in energy height for each segment using Equation (35) and Equation (36), respectively.

$$v = [\frac{4}{3}(\frac{W}{S})^2(\frac{k}{C_{D0}\rho^2})]^{\frac{1}{4}} \tag{35}$$

$$\Delta h_e = \Delta(h + \frac{v^2}{2g}) \tag{36}$$

With the climb velocity and change in energy height, the fuel fragment of each segment was calculated with Equation (37) and then multiplied together to get the total climb fuel fraction.

$$\frac{W_{i+1}}{W_i} = exp(-\frac{c\Delta h_e(P/v)}{\eta W(1 - D/(P/v))}) \tag{37}$$

The cruise segment fuel fraction was calculated using an exponential approach with the Breguet range equation by varying the lift to drag ratio. C_L was calculated at each stage using the weight of the aircraft, which was then used to calculate the lift to drag ratio. The cruise altitude for the standard mission was selected to be 2500 ft. This decision was made since it would be inefficient to climb to 8000 ft just to travel 25 nmi. The also FAA requires aircraft to fly at least 500 above ground level over sparsely populated areas []. This selected altitude allows the aircraft to comply with FAA regulations while saving fuel. The cruise altitude for the ferry mission remains at 8000 ft. The cruise was split into 10 segments and looped to find the cruise fuel fraction with Equation (38).

$$\frac{W_{i+1}}{W_i} = exp(-\frac{\Delta Rc}{\eta(L/D)_i}) \tag{38}$$

Note, for the MTOW configuration, the mission for spraying the field was modeled as a descent, cruise for the spray application, and a climb back to cruise altitude. The mission fuel fraction includes the cruise to the field, the descent to the field, the spraying of the field, the climb back to cruise, and the cruise back to the takeoff point.

The loiter fuel fraction was calculated using Equation (39) with a 30 minute loiter time. The maximum lift to drag for the aircraft was used.

$$\frac{W_{i+1}}{W_i} = exp(-\frac{Ev_\infty c}{\eta(C_L/C_D)}) \tag{39}$$

The descent and landing fuel fractions were estimated with historical data from Raymer[19]. The segment fuel fractions were multiplied to obtain the total overall fuel fraction for each mission. The fuel fractions for the MTOW and the maximum range configurations are listed in Table 4 and Table 5, respectively.

Table 4 Fuel Fractions for standard mission at MTOW

Condition	Fuel Fraction
Taxi	0.999
Takeoff	0.998
Climb	0.999
Cruise	0.845
Loiter	0.994
Descent	0.999
Landing	0.998
Total	0.957

Table 5 Fuel fractions for maximum range configuration

Condition	Fuel Fraction
Taxi	0.999
Takeoff	0.998
Climb	0.998
Mission	0.968
Loiter	0.994
Descent	0.999
Landing	0.998
Total	0.848

A trapped fuel factor of 1.06 is applied to the calculated fuel weight to account for trapped fuel in the system. After all other empty weight components were estimated, the weight estimation code was used to iterate the weight for each mission to determine the amount of fuel required. The MTOW configuration for the standard mission resulted in 337

lbs of fuel and 31 lbs of reserves for loiter. The maximum range configuration for the ferry mission resulted in 984 lbs of fuel and 31 lbs of reserves for loiter.

F. Batteries

Sizing of the batteries for the electric motors has been a critical design point throughout the entire sizing process of the aircraft. Due to the low energy density of batteries when compared to hydrocarbon based fuels, large battery weights are usually required to power the distributed electric propulsion system. A trade study was performed with the hybridization ratio of the aircraft with battery energy density, which will be discussed in the powertrain section. Based on the results of this trade study, the decision was made to decrease the hybridization ratio to 10% and only use the distributed electric propulsion system during the flight segments that require the most power, such as takeoff, climb, sustained turn maneuvers and spraying applications. The battery weight was estimated using the calculated fuel for each of the aforementioned sections at MTOW for the standard mission, since this is when the battery will be utilized the most. To do this, the mass of the battery was estimated using Equation 2.23 from the Metabook [20], as seen below.

$$m_{battery} = \frac{RW_0}{\eta e^* (L/D)} \tag{40}$$

The range (R) was estimated using the horizontal distance covered during climb, which was calculated with Equation (41), and the range covered during spraying the 400 acre field.

$$x_{climb} = \frac{\Delta h_e v_{climb}}{P_s} \tag{41}$$

Where $P_S = \frac{P - D \cdot v_{climb}}{W}$, using the weight during climb. The lift-to-drag ratio was estimated from the average LD at each flight segment that uses battery. η is the battery efficiency, while e^* is the specific energy of the battery. With the mass determined, the energy ratio of each section was calculated using Equation 2.25, as seen below.

$$E_{01} = (1 - (\frac{W_1}{W_0})_{HCFA})(\frac{W_0}{W_{cruisefuel}})_{HCFA} \tag{42}$$

The energy ratios for each segment were summed together and added to 1. The hybridization ratio (ϕ) was applied to this total energy ratio, as seen in Equation (43)

$$E_0 = \phi(1 + E_{01} + E_{12} + ...) \tag{43}$$

The total weight of the battery was determined by multiplying this energy ratio to the mass of the battery and acceleration due to gravity, as seen in Equation (44).

$$W_{battery} = m_{battery} g E_0 \tag{44}$$

The weight of the battery converged to 88 lbs, a substantial decrease from the thousands of pounds required for a 50/50 hybrid configuration that utilized the electric propulsion for all segments of flight.

G. Other Systems

Generally, aircraft instruments and avionics are designed to be lightweight, especially on smaller aircraft such as in the agricultural industry. As a result, for instruments such as a thermostat and barometer, it is expected to contribute for a weight of roughly 10 lbs. However, our aircraft utilizes AI spectral imaging technology that requires a specialized camera. A company known as Resonon has an airborne sensing system that has a payload as low as 5 lbs. Finally, our aircraft also contains a hydraulic system in order to control various parts of the aircraft. Typical weights of the hydraulic system ranges for 10 - 15 lbs for small aircraft. As a result, we settled on a hydraulic system weight of roughly 12 lbs. These values were determined through the Society of Allied Weight Engineers. [21]

H. Center of Gravity

The current location of the CG is 16.3 ft from the nose of the aircraft. During its travel, the aircraft's CG weight and location will change depending on what is used during the mission during different stages. The different weight configurations are as follows:

1) Maximum Takeoff Weight
2) Empty Weight + Maximum Fuel + Crew + Battery & Electronics
3) Empty Weight + Mission Required Fuel + Crew + Battery & Electronics
4) Empty Weight + Battery & Electronics

Table 6 C.G. Travel

Stage	**C.G. Weight** (lbs)	**X-Location** (ft)	**X-Location** ($\%MAC$)
Max Weight	7460	16.27	2.62
No Payload w/ Max Fuel	6110	13.91	2.34
No Payload w/ Mission Fuel	5460	13.77	2.21
No Payload w/o Fuel	5090	13.68	2.20

Table 7 Weight and Balance of the CD-4 (Datum Location at the Nose)

Component	**Weight** (lbs)	**C.G. Distance** (ft)
Fuselage	2800	14.2
Main Wing	160	19.1
Canard	65	5.6
Empennage	150	32.9
Gas Engine	320	3.8
Electric Motors	100	17.2
Main Landing Gear	440	18.4
Nose Landing Gear	200	3.8
Fixed Equipment	450	11.9
Fuel + Oil	1050	17.6
Battery	90	12.2
Crew	160	11.7
Payload	2000	23.1
Controller	44	17.2
Converter	5	11.9
Wiring	95	12.0
Hydraulics	12	11.9
Instruments	15	10

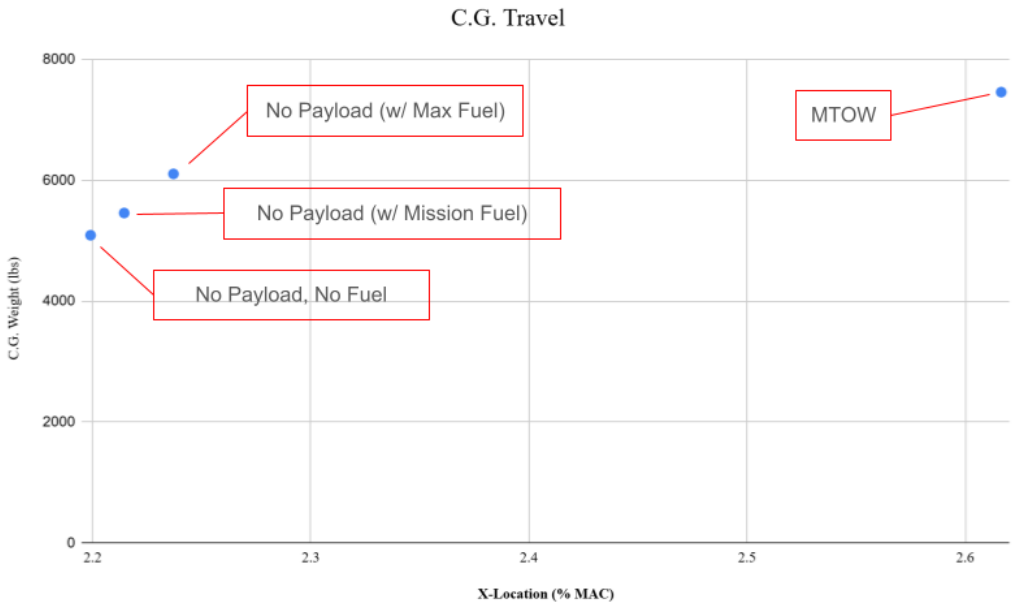

Fig. 15 C.G. Travel Diagram

VI. Aerodynamics

A. Wing Design

A wing with a 10 degree sweep angle was selected for electric propeller clearance. Winglets are also added at the tip, their primary function is to reduce wingtip vortices, thus less induced drag is created and lift efficiency is increased.

B. Aspect Ratio (AR)

In order to determine the Aspect Ratio, the wingspan and the reference wing area is required. The wingspan was given in OpenVSP as follows:

$$b = 52ft$$

To determine the wing reference area, we took the basic geometry of the wings to determine the reference area. The calculated reference area is

$$S_{ref} = 312ft^2$$

The aspect ratio is determined to be 8.7 from the following equation:

$$AR = b^2/S = 8.7 \tag{45}$$

The reference area and aspect ratio match up with the values given from OpenVSP.

C. Zero Lift Drag Coefficient

In the previous estimate for a drag polar, the value of the zero-lift drag was based solely on the aircraft's weight and wing surface area. Although this value is satisfactory for preliminary reports, the zero-lift drag value is not an accurate measurement for the aircraft. In determining the drag coefficient for the drag-polar, the following governing equation is used.

$$C_D = \left(C_{D0} + (\Delta C_D)_{\text{flaps}} + C_{D_{\text{trim}}}\right) + C_{Di} \tag{46}$$

There are several different factors that go into the aircraft's drag. However, one of the most important factors is the Zero-Lift Drag, or C_{D0}. While previous estimates use the aircraft weight, this estimate takes in several more factors, such as the aircraft components and leakage drag. The governing equation for determining the Zero Lift Drag is shown below. This equation is largely part of the method known as the Component Build Up Method.

$$C_{D_0} = \frac{1}{S_{\text{ref}}} \sum_{c=1}^{n_{\text{components}}} \left(C_{f_c} FF_c Q_c S_{\text{wet}}\right) + C_{D_{\text{mis}}} + C_{D_{L\&P}} \tag{47}$$

Equation (47) shows that there are three main parts in determining the zero lift drag. The first is a product of the components of the aircraft, the second is known as miscellaneous form drag, and the third component is leakage and protuberance drag.

1. Component Build Up

There are many factors going into determine the drag effect for each component. The first is the reference area, S_{ref}. We know this value to be 312 ft^2. The second factor is the component's skin friction coefficient, C_{f_c}. There are two equations used in determining that value. They are shown below as follows.

Laminar:

$$C_f = \frac{1.328}{\sqrt{R}} \tag{48}$$

Turbulent:

$$C_f = \frac{0.455}{(\log_{10} R)^{2.58}(1 + 0.144M^2)^{0.65}} \tag{49}$$

An important value necessary for determining these equations is the Reynolds Number. Flight is assumed to be at 150 knots and 8000 feet of elevation.

$$R = \frac{\rho V l_c}{\mu} \tag{50}$$

Finally, based on findings from Raymer, the attainable laminar flow as a percentage of wetted area for an aircraft made with smooth molded composites is 25% for the fuselage and 50% for the wings and tail. We use the weighted average of the laminar and turbulent to obtain the skin friction coefficient.

The next component used is the Form Factor, FF, which represents the shape of the component. To determine the form factor, the following equations were used.

For wings, tails, struts and pylons:

$$FF = \left[1 + \frac{0.6}{(x/c)_m}\left(\frac{t}{c}\right) + 100\left(\frac{t}{c}\right)^4\right]\left[1.34M^{0.18}\left(\cos\Lambda_m\right)^{0.28}\right] \tag{51}$$

For fuselage and canopy:

$$FF = \begin{cases} 0.9 + \dfrac{5}{f^{1.5}} + \dfrac{f}{400} & \text{if } f < 6 \\ 1 + \dfrac{60}{f^3} + \dfrac{f}{400} & \text{if } f \geq 6 \end{cases} \tag{52}$$

For nacelles and smooth external stores:

$$FF = 1 + \frac{0.35}{f} \tag{53}$$

where:

$$f = \frac{\ell}{d} = \frac{\ell}{\sqrt{\frac{4}{\pi}A_{\max}}} \tag{54}$$

The final two components are the interference factor, Q_c, and the wetted area, S_{wet} of the component. The wetted areas for each component were obtained through a tool in OpenVSP.

2. Miscellaneous Form Drag

The next component of drag affecting the zero lift drag is the miscellaneous form drag. The general equation for determining the drag is shown as follows.

$$C_{D_{\text{mis}}} = \frac{1}{S_{\text{ref}}} \sum_{c=1}^{n_{\text{components}}} \left(\frac{D}{q}\right)_c \tag{55}$$

D/q represents the drag area for each component of miscellaneous form drag. Our aircraft utilizes no speed brakes, spoilers, or bluff surfaces as well as no fuselage upsweep. However, there is the possibility of our aircraft's propellors of feathering or stopping outright. The equation to determine the drag area for a feathered and stopped engine is shown below.

$$\frac{D}{q} = \begin{cases} 0.1\sigma A_{\text{disk}} & \text{feathered prop} \\ 0.8\sigma A_{\text{disk}} & \text{stopped prop} \end{cases} \tag{56}$$

Utilizing the equation above, we found the change in the drag coefficient to be as follows for our electric and gas engines.

Table 8 Engine Failure Drag Increments

Scenario	ΔC_d
1 Electric engine feathered	0.000949
1 Gas engine feathered	0.006918
1 Electric engine stopped	0.007592
1 Gas engine stopped	0.055347

In addition to a feathered or stopped engine, another major factor for drag is the landing gear. Due to the fact that our aircraft uses a simple landing gear design, the drag effect of the landing gear would be constant, resulting in it contributing towards the zero lift drag with D/q being a quarter of the frontal area of the landing gear.

3. Leakage and Protuberance Drag

Leakage drag is a result of the inhaling and exhaling in high pressure zones while Protuberance Drag results from components such as antennas, vents, and edges. For a Propeller plane such as ours, we estimate the leakage and protuberance drag as a percentage of total parasite drag to be 7%.

4. Zero Lift Drag Determination

In our aircraft, there are ten different components looked at. They are listed as follows: the fuselage, the main wing, the canard, the booms, the main winglet, the canard winglet, the nacelles, the horizontal stabilizers, and the vertical stabilizers. The values used for each values are shown as follows in Table 2.

With these values, we could finally obtain the overall zero lift drag. Furthermore, we will compare them to the estimated values from OpenVSP, also using the drag build up method.

Table 9 Aerodynamic Drag Breakdown with Component Parameters

Component	S_{wet}	FF	L_{ref}	f	C_f	Q
A: Fuselage	375.89	1.3828	30.00	4.832	0.002 015	1.00
B: Main Wing	538.50	2.2510	6.22	0.180	0.001 990	1.00
C: Canard	93.98	1.5606	3.00	0.120	0.002 357	1.00
D: Canopy	57.03	2.0755	12.00	2.635	0.002 359	1.00
E: Booms	79.91	1.0553	18.00	18.00	0.001 591	1.00
F: Main Winglet	46.39	1.3560	3.16	0.120	0.002 328	1.00
G: Canard Winglet	8.17	1.7092	2.07	0.120	0.002 582	1.00
H: Nacelle 1	10.04	1.0467	5.00	7.500	0.002 091	1.00
H: Nacelle 2	10.14	1.0467	5.00	7.500	0.002 091	1.00
H: Nacelle 3	11.17	1.0467	5.00	7.500	0.002 091	1.00
H: Nacelle 4	12.72	1.0467	5.00	7.500	0.002 091	1.00
H: Nacelle 5	10.82	1.0467	5.00	7.500	0.002 091	1.00
I: Horizontal Stabilizer	130.64	1.6216	4.00	0.100	0.002 201	1.07
J: Vertical Stabilizers	130.36	1.3461	4.01	0.120	0.002 200	1.07

Table 10 Zero Lift Drag Comparison

Component	Buildup Method (Cd0)	OpenVSP (Cd0)
A: Fuselage	0.003 356	0.003 93
B: Main Wing	0.007 732	0.008 59
C: Canard	0.001 108	0.001 50
D: Canopy	0.003 356	0.000 99
E: Booms	0.000 430	0.000 77
F: Main Winglet	0.000 469	0.000 73
G: Canard Winglet	0.000 116	0.000 14
H: Nacelle 1	0.000 070	0.000 13
H: Nacelle 2	0.000 071	0.000 13
H: Nacelle 3	0.000 078	0.000 14
H: Nacelle 4	0.000 089	0.000 16
H: Nacelle 5	0.000 076	0.000 14
I: Horizontal Stabilizer	0.001 599	0.001 90
J: Vertical Stabilizers	0.001 071	0.001 98
Leakage/Protuberance	0.002 381	
Landing Gear	0.014 387	
TOTAL	**0.036389**	

D. Lift-Induced Drag

The trim drag and lift-induced drag were estimated using AVL. The team rebuilt the aircraft's configuration using the lifting surfaces only. It is important to note that the fuselage, nacelles, propellers, and boom were all omitted in order to find the drag values that were only based on the lifting surfaces. This is due to AVL's way of estimating the drag on the aircraft. AVL combines the drag coefficient into one number with the profile drag being a separate addition.

In order to minimize the errors while using AVL and to get an accurate drag estimation from the induced lift, we decided it was best to only use the lifting surfaces. AVL combines the trim drag and the lift-induced drag into a combined number that is only classified as "CDind" for each defined CL value. In AVL, we modelled the aircraft using three different control surfaces. In the AVL geometry file, the canard is able to rotate entirely, flaps were modeled on the entirety of the main wing span with the hinge being at 0.7c, and the elevator was modeled on the horizontal stabilizer with the hinge being located at 0.5c.

Using AVL, we estimated the Drag Values at various lifts in order to determine the lift-induced drag for takeoff, landing, and cruise. However, the drag coefficient is also nonzero at a lift of zero. This is due to AVL modeling trimmed drag in addition to lift-induced drag. Additionally, the zero lift drag varies from takeoff and landing compared to cruise. This allows for the program to also model flap drag. Using AVL, we helped identify the following governing equations and values for the drag polar.

$$C_d = C_{d0} + KC_l^2 \tag{57}$$

$$C_{d0,trim} = 0.00374$$

$$C_{d0,flaps.takeoff} = 0.0665$$

$$C_{d0,flaps,landing} = 0.1640$$

$$K = 0.04017$$

E. Configurations

There are three different configurations to consider when using AVL, the first is landing, second is takeoff, and the last is cruise. During cruise, there is no flaps and the elevator and canard deflection are not enforced. To enforce trim, the aircraft is set at the cruise speed (150 knots) and all moments were enforced to zero to simulate trim conditions. In this configuration, the combined drag coefficient given by AVL only includes lift-induced drag and trim drag as a combined value, with no drag due to flaps. The next two configurations, landing and takeoff, had their drag estimated with elevator, canard, and flap deflection. This means that the drag estimation given includes the drag needed to trim (canard and elevator deflection), drag due to flaps (flap deflection) and drag due to induced lift (based on the CL). Refer to Table 11 for the different configuration deflections.

Table 11 Configuration Deflections

Component	Takeoff	Landing	Cruise
Flaps	15°	30°	0°
Elevator	-4.2°	-2.2°	+0.5°
Canard	15°	15°	0°

It is important to note that there is an even distribution of lattices on the lifting surfaces with 5 vorticies for each side of a lifting surface. This means that our results have room for increased fidelity if we chose to increase our vortex lattice density. For each configuration, the CL was enforced in AVL going up in 0.1 increments starting from zero. At each step, the CDind was recorded based on the AVL calculations. This results in a drag polar for each configuration where the CL was enforced and the CDind is calculated.

F. Flap Sizing

From Table 3.1 in Roskam[12], $C_{L_{max}}$ for agricultural aircraft typically fall within the range of 1.3 to 1.9. The estimate for $C_{L_{max}}$ was set to 1.9 based on this data.

To validate if the $C_{L_{max}}$ was a reasonable value to achieve at takeoff and landing when high C_L values are needed, a polar analysis was performed on the selected NACA 23018 airfoil selected for the wing. The flap angles were set to 15° and 30° for takeoff and landing configurations, respectively. The geometry of each configuration was created using GDES on Xfoil. Initially, the hinge point was set at 80% of the chord length, but after performing analysis in AVL, the flaps were insufficient in generating enough lift for the aircraft at a safe angle of attack. This led to the hinge point

being moved to 70% of the chord length in order to increase the flap size. The geometry for each configuration is seen in Figure 19. The airfoil is treated as a single modified geometry since the selected flap style will be plain flaps with minimal gaps to reduce complexity.

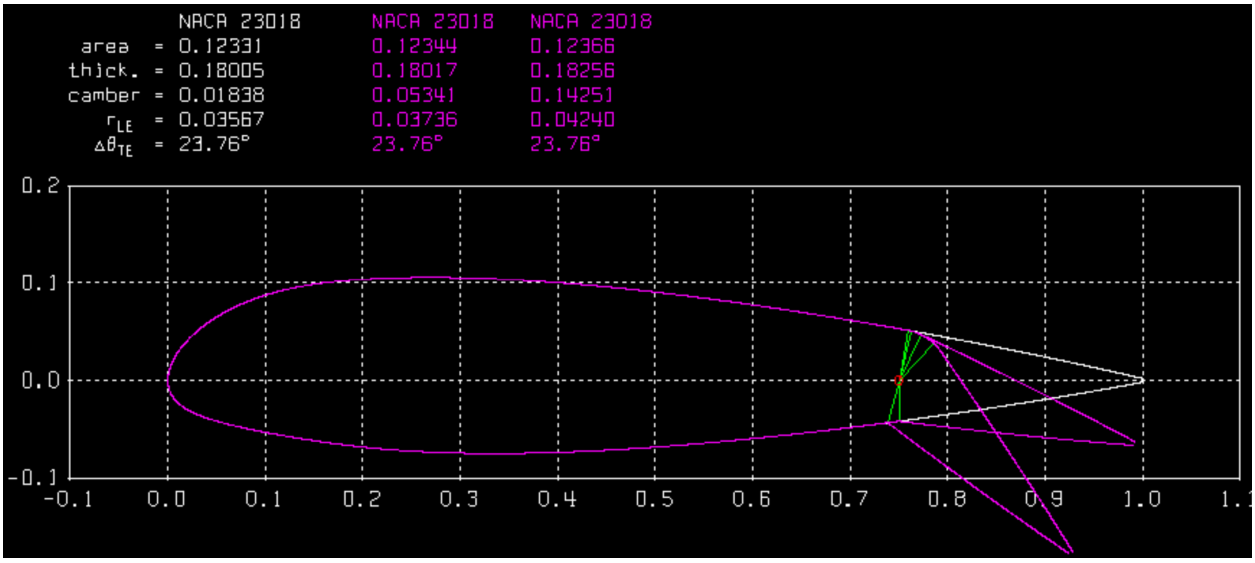

Fig. 16 Takeoff and landing flap deflections of airfoil section in Xfoil

Our aerodynamic analysis in AVL shows that the main wing's 26 ft semi-span (52 ft total span) uses a segmented flap system to optimize performance. The inboard flap section spans from 8 ft to 16 ft from the centerline, with a hinge at 70% chord was specifically chosen to enhance low-speed lift generation. The outboard section spans from 18 ft to 26.0 ft integrates a dual-function aileron-flap with an 85% chord hinge, balancing roll control and lift augmentation. This asymmetric hinge positioning, validated through AVL's vortex-lattice modeling, ensures efficient load distribution while maintaining symmetry across the left/right wings (mirrored in negative Y-values). The 3D results confirm enhanced maneuverability and stall resistance, critical for the CD-4's low-altitude mission profile.

Using a Reynold's number of $5.5 \cdot 10^6$, which was selected from density and speed parameters at takeoff and landing conditions, the airfoil was varied from an angle of attack of 0° to 19° to determine the maximum sectional lift coefficient and stall angle. This stall angle is used to verify that the aircraft does not pass stall angle during trimmed takeoff and landing conditions. The polar plots of takeoff and landing flapped airfoils are seen in Figures 17 and 18, respectively.

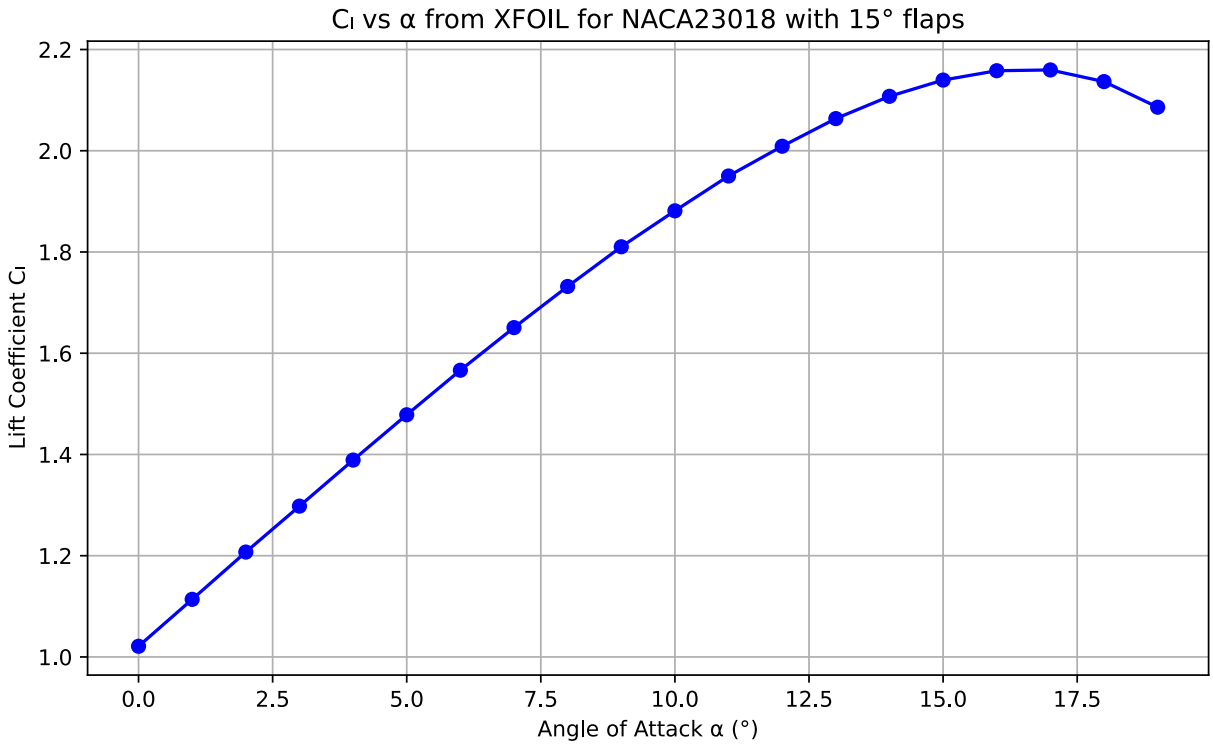

Fig. 17 Polar of 15° flapped airfoil

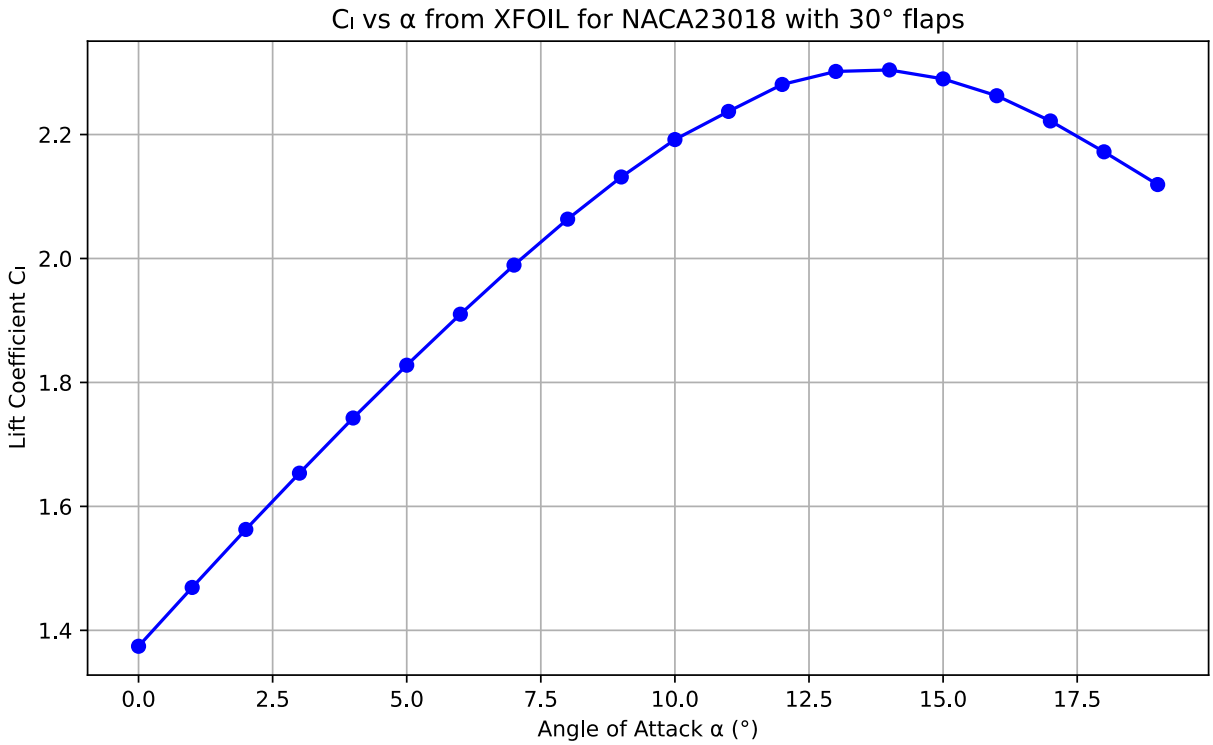

Fig. 18 Polar of 30° flapped airfoil

From the polar plots for takeoff and landing flaps, the $C_{L_{max}}$ vales are estimated to be 2.15 and 2.3, respectively. The stall angles are estimated to be 17° and 14° for takeoff and landing. These sectional $C_{L_{max}}$ exceed the selected $C_{L_{max}}$ value of 1.9, indicating the flaps are big enough to generate enough lift.

G. Drag Polar

Through combining the drag coefficient values found in AVL to the Parasite Drag from the build up method, we are able to determine the overall drag polar in the equation. We found that by introducing trimmed drag, the drag coefficient would go up by 0.00034, leading to a minimum drag in cruise amounting to 0.03673. Furthermore, we are able to determine the affects of the landing and takeoff flaps by finding the difference in the minimum drag compared to the cruise condition. With a minimum drag coefficient of 0.04338, we found that the takeoff flaps add 0.00665 to the drag coefficient. Landing flaps add more, with a minimum drag coefficient of 0.05313, resulting in an increase of 0.0164. The updated drag coefficient is shown below.

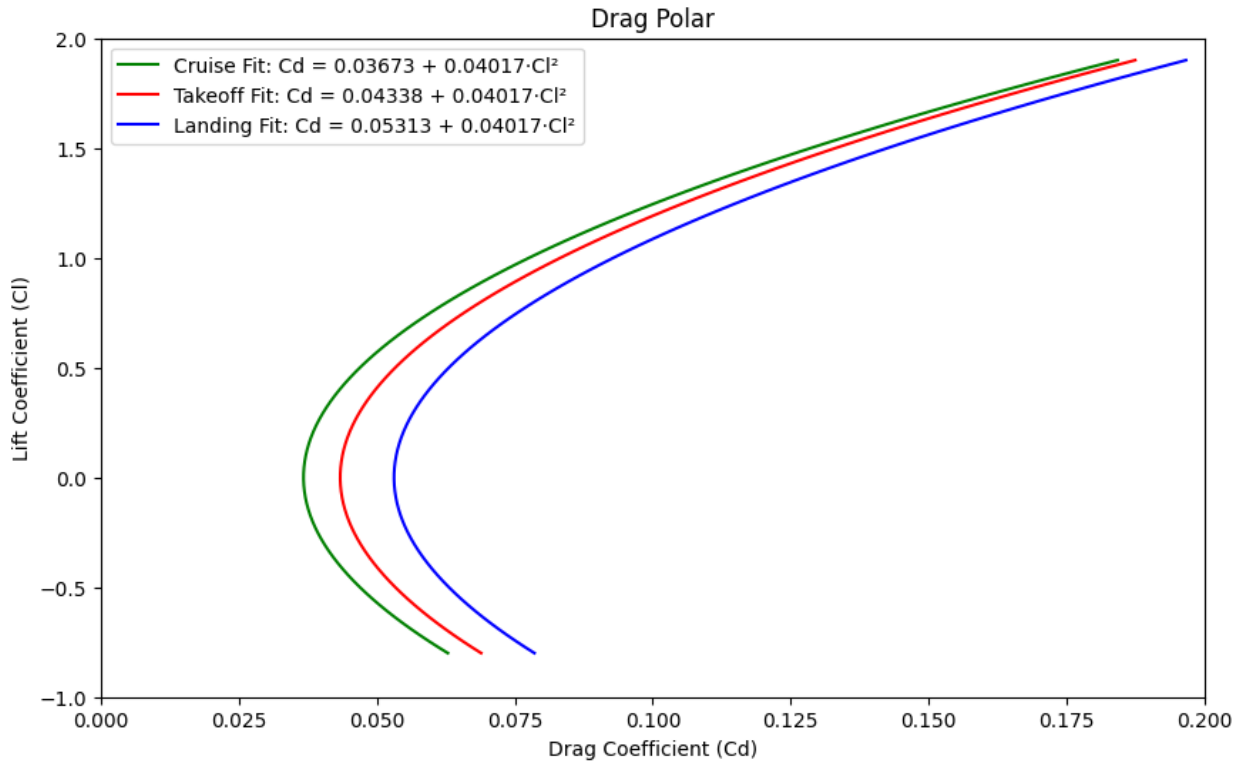

Fig. 19 Drag Polar for Three Conditions: Cruise, Takeoff, and Landing

H. Main Wing/Canard Airfoil Selection

The chosen airfoil for CD-4 Cybertruk's main wing is NACA 23018, it is a member of the NACA 5-digit series, which is described by its specific aerodynamic characteristics. This airfoil features a maximum thickness of 18% located at 30% of the chord length from the leading edge, and a maximum camber of 1.8% located at 15% of the chord. The reason why this airfoil was picked is because of the following factors:

1. High lift coefficient

The NACA 23018 is designed to have a higher lift coefficient compared to some other airfoils. It has a $C_L max$ of approximately 1.4 to 1.6, this factor is beneficial for agricultural aircraft since they mainly operate at lower speeds and require a certain lift to carry heavy loads. In addition, having a high $C_L max$, this allows for a wider range of mission profiles. This factor enhances the versatility of the aircraft, enabling it to perform various tasks along its original agricultural functions.

2. Structural thickness

With a maximum 18%, this airfoil provides a sturdy structural profile. This thickness allows for stronger wing structure, which is good for CD-4 Cybertruk when it encounter rough field conditions or bad weather condition thus this would require durable wings to withstand various type of operational stresses. Additionally, with the 5 electric motors, fuel tanks, booms, spraying equipment on each wing, structural integrity is crucial for the success of these wings. A thicker airfoil will allow room for structural components and attachment points for the nacelles of the electric motors.

3. Low-speed handling and stall characteristics

Another compelling reason to choose the NACA 23018 airfoil for CD-4 Airtruk is because it has excellent low-speed handling characteristic and predictable stall behavior. Numerical data shows that the NACA 23018 airfoil experiences stall at an angle of attack approximately around 16 degrees. This relatively high stall angle gives a comfortable margin

of safety during low-speed operations.

Table 12 Main Wing Parameters

Parameter	Value
Span (b_w)	52 ft
Root Chord ($c_{w,root}$)	8 ft
Tip Chord ($c_{w,tip}$)	4 ft
Sweep Angle (λ_w)	10°
Area (S_{ref})	312 ft^2
Aspect Ratio (AR)	8.7

Table 13 Canard Parameters

Parameter	Value
Span (b_c)	20 ft
Root Chord ($c_{c,root}$)	3 ft
Tip Chord ($c_{c,tip}$)	3 ft
Sweep Angle (λ_c)	0°
Area (S_{ref})	60 ft^2
Aspect Ratio (AR)	6.7

I. Empennage Airfoil Selection

The chosen airfoil for CD-4 Cybertruk's empennage is NACA 0012, which is an excellent choice for our agricultural aircraft, since it offers specific advantages that align with the requirements of agricultural operations. It has a symmetrical profile with 12% thickness and predictable aerodynamic characteristics along with great structural benefits.

1. Symmetric Characteristics

The NACA 0012 is a symmetrical airfoil, thus producing 0 lift at 0 angle of attack. This is ideal for the installation since it guarantees neutral aerodynamic behavior when the control surfaces are centered. With the neutrality, the balanced pitch and yaw responses are predictable.

2. Low-Drag Performance

Since empennage typically does not generate a lot of lift but it does contribute to the overall drag, with NACA 0012's relatively low drag, efficiency is maintained. This is important for low-speed operations with precision tasks meanwhile keeping the efficiency good for fuel.

3. Good control at low Reynolds numbers

Since empennage typically operate at lower Reynolds numbers when compared to the main wing. The NACA 0012 is known to perform reliable and effective in low Reynolds numbers condition, ensuring that the control surfaces remain controllable during low-speed operations.

Table 14 Horizontal Stabilizer Parameters

Parameter	Value
Span (b_h)	16 ft
Root Chord ($c_{h,root}$)	4 ft
Tip Chord ($c_{h,tip}$)	4 ft
Sweep Angle (λ_w)	0°
Area (S_{ref})	64.0 ft^2
Aspect Ratio (AR)	4

Table 15 Vertical Stabilizer Parameters

Parameter	Value
Reference Span (b_h)	18.7 ft
Reference Chord ($c_{h,root}$)	4 ft
Reference Area (S_{ref})	71.63 ft^2

J. Speeds

The relationship between specific range at different cruise speeds and altitudes was studied. The main goal are lowering the fuel burn and cost of the aircraft. The original cruising speed was 150 knots and the cruising altitude is 8000 ft, but as speed increases, the specific range decreases and the operation cost of the aircraft increases, thus the trade study's main goal is to figure out what is the optimal speed and altitude to cruise at for maximizing fuel efficiency. Figure 20 reveals a clear trend of the specific range, which peaks at around Mach 0.17 and gradually decreases as cruise speed increases. This indicates that a slight reduction in cruise speed can significantly enhance fuel efficiency at the cost of increased flight time. At the CD-4 Cybertruk's designated cruise altitude of 8,000 feet, chosen to align with industry standards for agricultural aircraft[14]. The optimal cruise speed was determined to be approximately Mach 0.17. Although the most fuel-efficient altitude was identified as 10,000 feet, maintaining a cruise altitude of 8,000 feet at Mach 0.17 still yields a favorable specific range of roughly 0.29 nautical miles per pound of fuel. Operating at this condition reduces fuel consumption, thereby lowering overall operating costs and increasing efficiency.

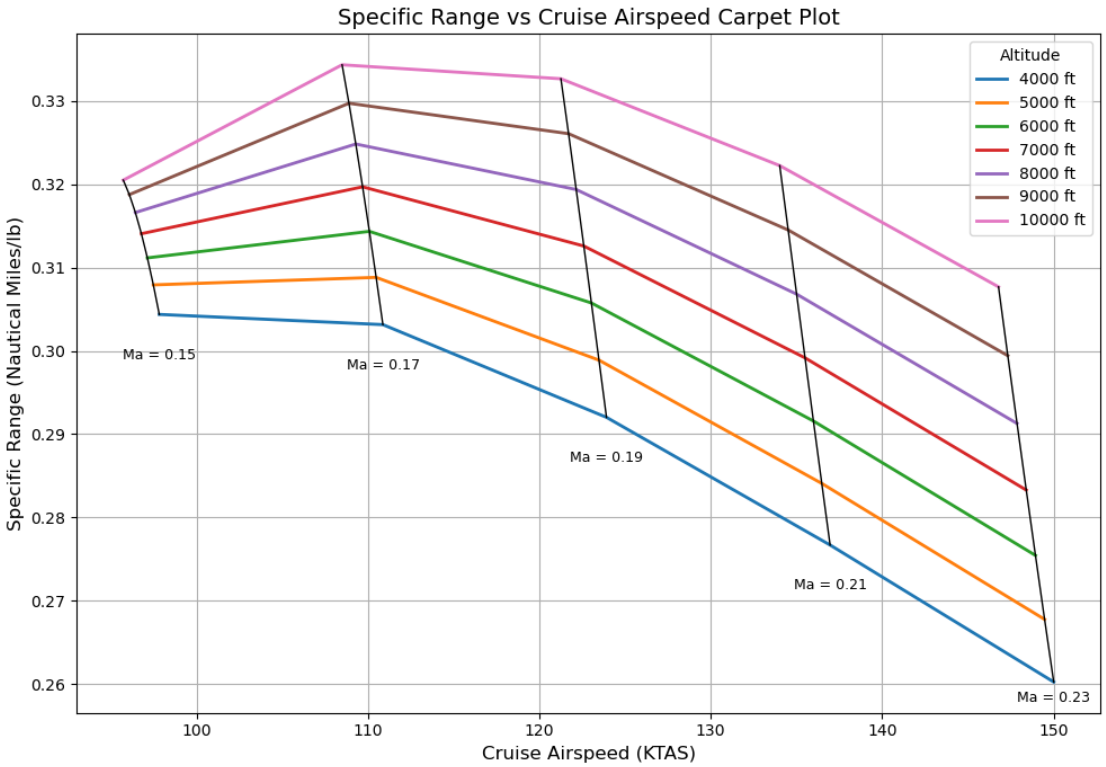

Fig. 20 Specific Range vs Cruise Speed Trade Study Plot

K. Payload Range Chart

A payload range chart was created to determine the payload load and range for the design mission, max fuel with payload, and max range configurations. Figure 21 displays the trade-offs between payload weight and the range achievable by the aircraft.

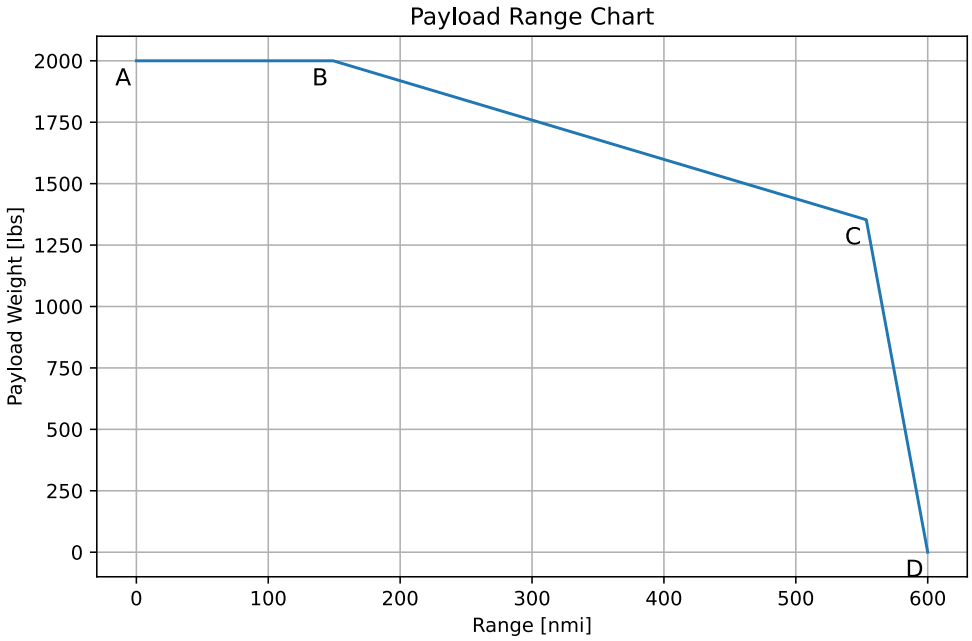

Fig. 21 Payload range chart

The maximum payload range at point B is determined from the RFP requirements. This includes a 25 nmi cruise segment out and back from the take-off point, 50 nmi total, as well as passes and turns necessary to cover a square 400 acre area. In total, this range stands at about 149 nmi. To carry the 2000 lb maximum payload this far, 337 lbs of fuel are required, with an additional 31 lbs of fuel dedicated to reserves for a 30 minute loiter. The maximum amount of fuel required to reach the required 600 nmi range at point D was calculated to be 984 lbs, plus an additional 31 lbs of fuel for reserves. With the maximum amount of fuel known, the payload at point C, which is the load at MTOW with maximum fuel, was calculated to be 1353 lbs. In this configuration, the aircraft is able to travel 553 nmi, just 47 nmi shorter than the no payload configuration. What this chart shows is that the aircraft can successfully transport large amounts of payload for hundreds of miles. While it may not be able to transport its max payload for the full ferry range, it can successfully carry about 70% of its max payload for about 550 nmi, allowing the aircraft to access smaller fields which may be further away. Additionally, this makes it ideal for transporting payload that can be offloaded at another site. The original fuel tanks were sized to carry 45 gallons each, for a total of 90 gallons, meaning they did not have enough capacity to contain the 1015 lbs of fuel (152 gallons) required to reach the maximum range of 600 nmi. Since the structural attachment point of the tail booms prevents extension of the tanks, an additional 35 tank was added into each wing to allow for a total fuel capacity of 160 gallons. The tanks will be connected with plumbing and pumps to allow for weight balance during flight.

VII. Stability and Control

A major factor in determining the success of an aircraft design is the aircraft's stability. Stability plays a huge factor in determining how an aircraft can recover from a disturbance. Furthermore, stability can result in a more predictable and a more comfortable flight for both pilots and passengers. A major factor in determining an aircraft's static margin. A higher static margin represents a higher stability for an aircraft, while a lower static margin means the aircraft is less stable. Furthermore, a negative static margin means that an aircraft is unstable, resulting in an inoperable aircraft. To determine the static margin, two values are first needed. The first is the center of gravity, which represents the point where the aircraft's mass is balanced. The second factor is the neutral point, which is the location where the aircraft's pitching moment remains constant with changes in angle of attack.

A. Neutral Point

Upon further inspection of the neutral point and static margin hand calculations, errors were found that severely underestimated the static margin and placed the neutral point further forward than it actually was, meaning the plane was over-stable and lacked pitch control. To counteract this effect, the decision was made to move the wing and the components within it, such as electric motors and fuel tanks, 2.5 ft forward in order to shift the neutral point forward and reduce the static margin. This allowed the plane to achieve a static margin closer to 0.10 at MTOW. The hand calculation and AVL computation process is derived in the following section.

To determine the neutral point, several preliminary steps must be taken. A multitude of factors influence the neutral point's location. In our aircraft, the primary contributors are the wing, the canard, the tail-mounted horizontal stabilizers, and the fuselage. Typically, horizontal stabilizers provide a positive contribution, shifting the neutral point further aft in the aircraft. A canard, however, is positioned ahead of the wing, resulting in a negative distance value from the center of gravity. Additionally, the canard generates a lift component that produces an opposing moment to the tail-mounted horizontal stabilizers. To determine the neutral point, we first employed the following governing equation:

$$C_{m_{cg}} = \frac{x_{cg}}{\bar{c}} C_{L_w} + \frac{l_h S_h}{S_w \bar{c}} C_{L_h} + C_{m_w} + C_{m_{fus}} \tag{58}$$

In our aircraft, there are two horizontal stabilizers and a canard. The canard is referenced with a subscript of 'c', while the horizontal stabilizers are denoted with a subscript of 'h'. Using the equation above, we derived the neutral point formula as follows:

$$\frac{\bar{x}_{\text{np}}}{\bar{c}} = \frac{l_h S_h}{\bar{c} S_w} \frac{\partial C_{L_h}}{\partial \alpha} \left(\frac{\partial C_{L_w}}{\partial \alpha} \right)^{-1} - \frac{l_c S_c}{\bar{c} S_w} \frac{\partial C_{L_c}}{\partial \alpha} \left(\frac{\partial C_{L_w}}{\partial \alpha} \right)^{-1} - \frac{\partial C_{m_{\text{fus}}}}{\partial \alpha} \left(\frac{\partial C_{L_w}}{\partial \alpha} \right)^{-1} \tag{59}$$

Our aircraft employs an unconventional wing configuration, with a canard positioned ahead of the wing. As a result, when determining the components for the neutral point, we assigned a negative value to the canard's contribution, accounting for the negative l_c.

To compute this equation, the first component analyzed is $\left(\frac{\partial C_{L_w}}{\partial \alpha} \right)$. It is determined using the following equation:

$$\frac{\partial C_{L_w}}{\partial \alpha} \approx \frac{2\pi AR}{2 + \sqrt{\left(\frac{AR}{\eta} \right)^2 \left(1 + \tan^2 \Lambda - M^2 \right) + 4}} \tag{60}$$

The values for these equations are provided in Tables 1-4. Furthermore, this equation can be applied to the canard and horizontal stabilizers, yielding $\left(\frac{\partial C_{L_{h,\text{clean}}}}{\partial \alpha} \right)$ and $\left(\frac{\partial C_{L_{c,\text{clean}}}}{\partial \alpha} \right)$. To determine the actual values for the change in canard and stabilizer lift coefficient per change in angle of attack, the effects of downwash must be considered. Downwash can be estimated using the following equation:

$$\frac{\partial \varepsilon}{\partial \alpha} \approx \frac{2}{\pi AR_w} \frac{\partial C_{L_w}}{\partial \alpha} \tag{61}$$

Typically, a horizontal stabilizer experiences downwash, which reduces the lift coefficient slope. Conversely, a canard experiences upwash, producing the opposite effect. To determine the lift slope for the canard and the stabilizers, the following equations were used:

$$\frac{\partial C_{L_h}}{\partial \alpha} = \frac{\partial C_{L_{h,\text{clean}}}}{\partial \alpha} \left(1 - \frac{\partial \varepsilon}{\partial \alpha} \right) \tag{62}$$

$$\frac{\partial C_{L_c}}{\partial \alpha} = \frac{\partial C_{L_{c,\text{clean}}}}{\partial \alpha} \left(1 + \frac{\partial \varepsilon}{\partial \alpha} \right) \tag{63}$$

The final necessary component is the fuselage pitching moment. To determine the pitching moment coefficient slope, the following equation was used:

$$\frac{\partial C_{m_{\text{fus}}}}{\partial \alpha} = K_f \frac{w_f^2 L_f}{S_w \bar{c}} \tag{64}$$

K_f, or the engine nacelle moment factor, is directly related to the position of the quarter chord of the aircraft wing relative to the length of the fuselage. Our aircraft's wing is positioned relatively far aft on the fuselage, at 56.67% of its length. As a result, $K_f = 0.821$. This value is higher than that of traditional aircraft, which is accounted for by the presence of the canard. The final value necessary before calculation is the mean aerodynamic chord length, or $barc$. Using the root and tip chord lengths, we determined the taper ratio to be:

$$\lambda = \frac{c_{\text{tip}}}{c_{\text{root}}} = 0.5 \tag{65}$$

With the taper ratio, we calculated the mean aerodynamic chord as follows:

$$\bar{c} = \frac{2}{3} c_{\text{root}} \frac{1 + \lambda + \lambda^2}{1 + \lambda} = 6.22\,\text{ft} \tag{66}$$

Finally, we determined the coefficient slopes to be as follows:

$$\left(\frac{\partial C_{L_w}}{\partial \alpha}\right) = 2.49$$

$$\left(\frac{\partial C_{L_c}}{\partial \alpha}\right) = 2.91$$

$$\left(\frac{\partial C_{L_h}}{\partial \alpha}\right) = 1.97$$

Using these values in Equation 2, we calculated the neutral point location from the nose to be:

$$x_{np} = 16.44\,\text{ft}$$

These results were validated in AVL when analyzing trimmed conditions, as discussed later.

B. Static Margin

With both the neutral point and the center of gravity determined, we can now calculate the static margin. The static margin is defined as the difference between the neutral point and the center of gravity, normalized by the mean aerodynamic chord length, as expressed in the following equation:

$$\text{SM} = \frac{x_{\text{np}} - x_{\text{cg}}}{\bar{c}} \tag{67}$$

The resulting static margin at MTOW is shown below:

$$SM = 0.103$$

With a positive static margin, it indicates that the aircraft is generally stable. During operation, the center of gravity shifts forward as the fuel weight decreases during flight. This results in the static margin increasing as the aircraft is in service. With a higher static margin, the stability of the aircraft increases, however in turn, the maneuverability decreases. Overall, the aircraft is in a good range of stability during flight. This value will be validated in AVL, as discussed in the trimmed conditions section.

C. Control Surfaces Sizing

1. Elevator

Initially, the horizontal stabilizer had a chord length of 2.5 ft, and the elevator hinge point was at 60% of the chord length. Due to the high stability of the aircraft, this was found to create excessive elevator deflections of over 30°, therefore, the decision to increase the size of both the horizontal stabilizer and elevator was made. The horizontal stabilizer was increased to 4 ft, while the hinge point was moved to 50% of the chord length. When performing the trim analysis of the aircraft as seen later, the elevator required deflections of less than 10° to trim all conditions of the aircraft.

2. Canards

The canards were initially designed as fixed pitch to provide supplemental lift during critical maneuvers such as sustained turns. As previously mentioned in the elevator sizing section, excessive elevator deflections were required to trim the aircraft. In combination with increasing the elevator size, the canards were made variable pitch in order to generate additional lift in the front of the aircraft to support the pitch up moment. The chord was also increased from $2\frac{2}{3}$ ft to 3 ft to provide additional lift. Moving forward, a control system will have to be determined for the canards. There are two options that are being considered. The first is to link the canards to the elevator control system such that they provide additional pitch when the elevator is activated. A second option is to have set increments like flaps to allow for constant provided lift.

3. Ailerons

Historical data from comparable agricultural aircraft guided the sizing of the outboard control surfaces. To maintain sufficient roll authority throughout the mission profile, the aileron span was set to 8 ft from the tip of the wing and the hinge was placed at 85% of the chord.

4. Rudders

The main consideration for the sizing of the rudder was to make sure that the aircraft was able to still fly under conditions when one section (in this case the distributed propulsion along a wing) were to become inoperable. To size for these conditions, we can need to balance out the moment applied to the C.G.

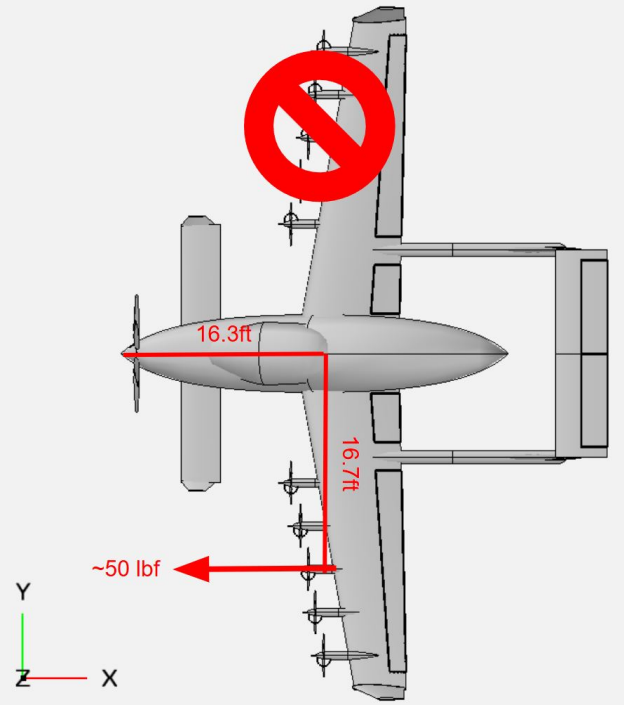

Fig. 22 One Engine Inoperable (OEI) Diagram

As seen in Figure 22, the location of the C.G. and the total force from the distributed propulsion is labeled on the diagram. Based on the thrust generated from the electric propulsion, this applies a moment onto the C.G. that can be seen in Figure 23.

To keep controlled flight, we need to see how much force is needed to counteract the moment. In this case, due to the location of the vertical stabilizers, the force required is around 40 lbf (as seen in Figure 24).

Currently, the rudder is sized so that the hinge location is located at $0.5c$. This means that the rudder is 50 percent of the vertical stabilizer. Rearranging Equation 68 will give us the C_L required and therefore the deflection needed to stabilize the aircraft for cruise conditions.

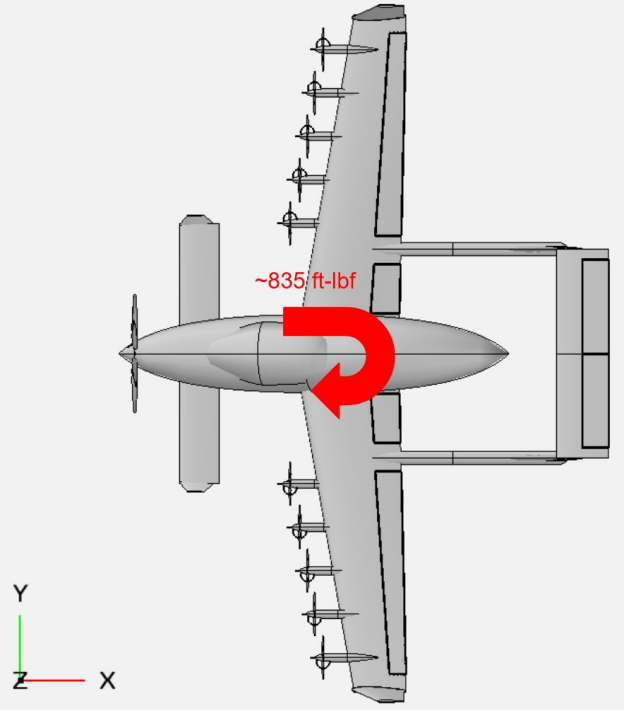

Fig. 23 Moment Applied to C.G.

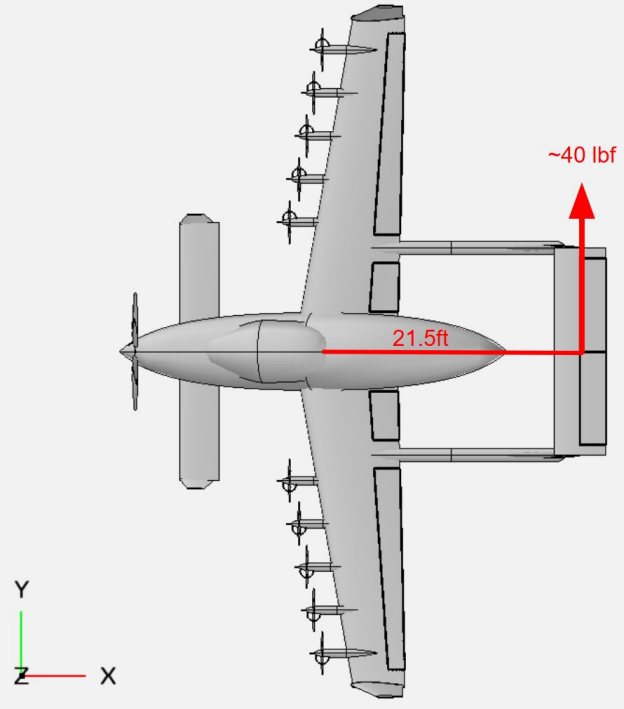

Fig. 24 Required Rudder Force

$$L = C_L \cdot \frac{1}{2}\rho_{8000ft} V_{cruise}^2 S_{ref} \tag{68}$$

Rearranging gives the following:

$$C_L = \frac{L}{\frac{1}{2}\rho_{8000ft} V_{cruise}^2 S_{ref}}$$

Using the values for the vertical stabilizer, altitude density, and cruise speed, we get the following equation:

$$C_L = \frac{40lbf}{\frac{1}{2}(0.02106\frac{slugs}{ft^3})(253\frac{ft}{s})^2(71.63ft^2)} = 0.0083$$

Based on C_L required by the vertical stabilizer, the effects of OEI are essentially negligible and no changes need to be made to the rudder's size.

D. Trimmed Conditions

AVL was used to determine the trimmed conditions at takeoff, cruise and landing by determining the elevator deflection angle that created 0 pitching moment. For takeoff, the flap deflection is set to 15°, and the angle of attack was set to reach the $C_{L_{max}}$ of 1.9. The lift distribution is seen in Figure 25

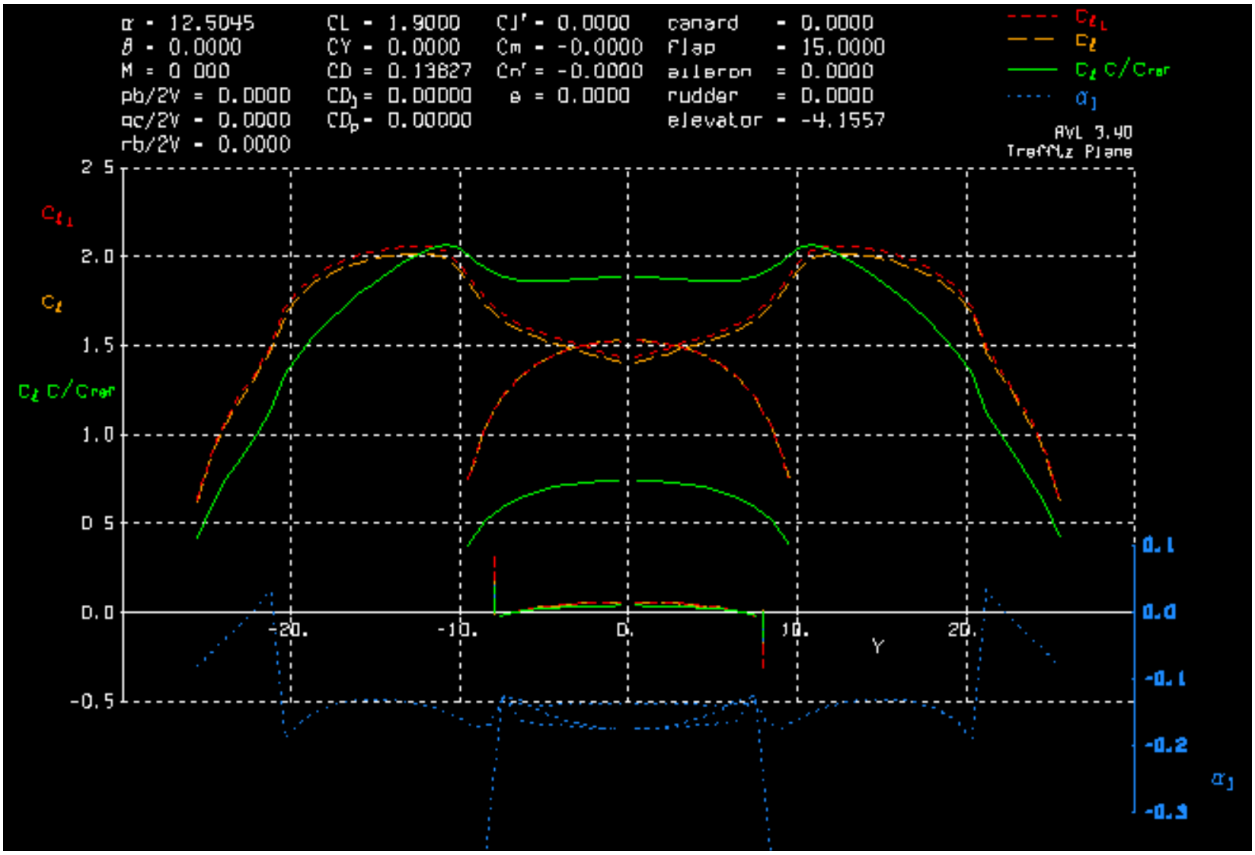

Fig. 25 Lift distribution for trimmed takeoff condition

For cruise, the angle of attack was selected to be 3°. The lift distribution is seen in Figure 26

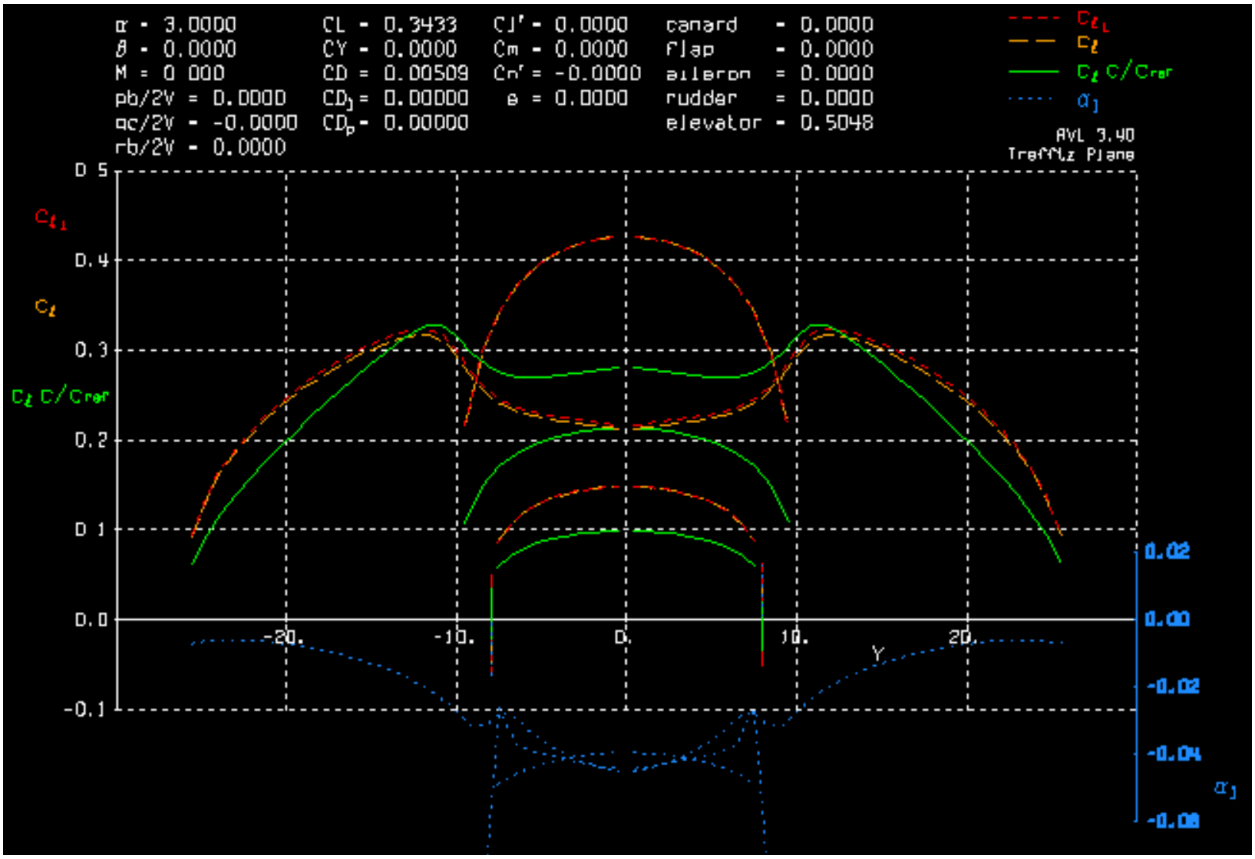

Fig. 26 Lift distribution for trimmed cruise condition

For takeoff, the flap deflection is set to 30°, and the angle of attack was set to reach the $C_{L_{max}}$ of 1.9. The lift distribution is seen in Figure 27

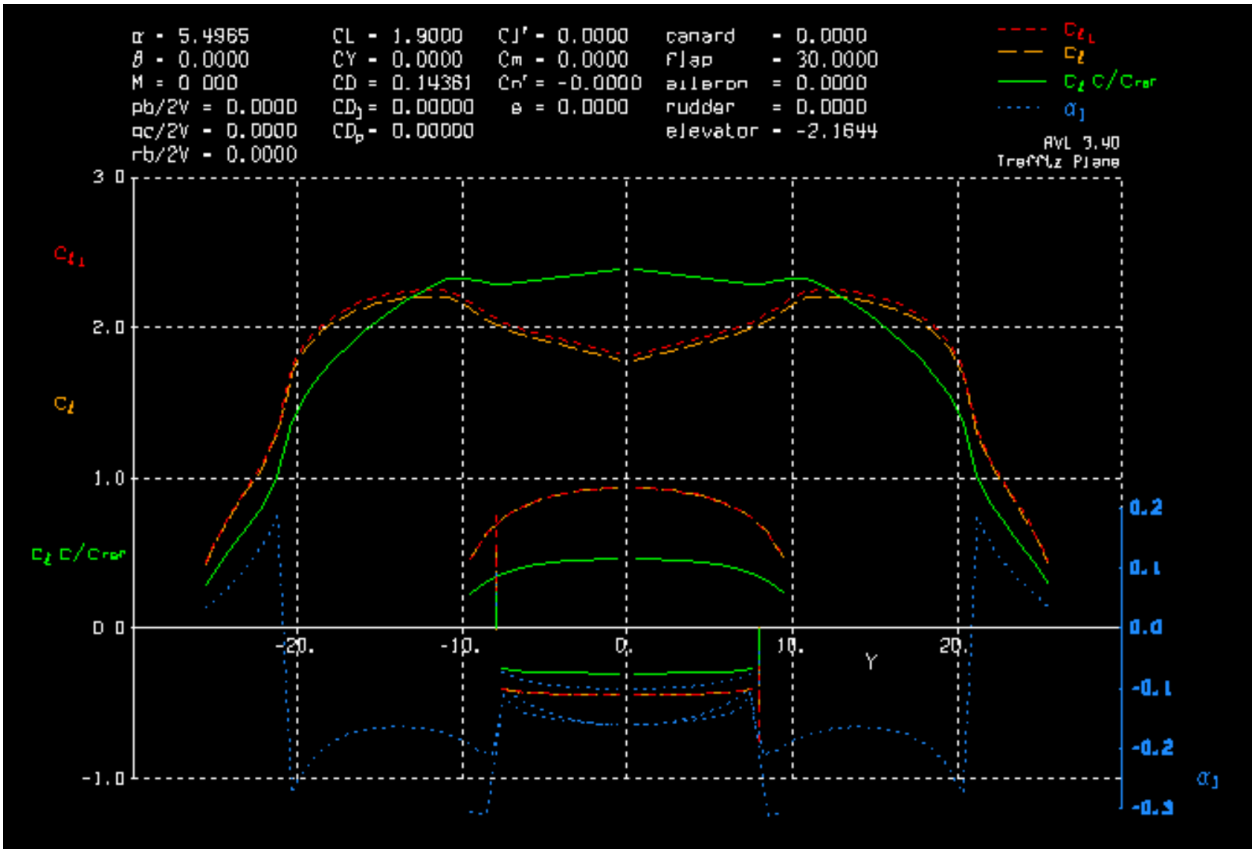

Fig. 27 Lift distribution for trimmed landing condition

The elevator deflections for the trimmed conditions are listed in Table 16. A positive angle indicates a downward deflection, causing the aircraft to pitch down. A negative angle indicates an upward deflection, causing the aircraft to pitch up. The low elevator deflections indicate the elevator as been properly sized to provide enough pitch control.

Configuration	Elevator Deflection
Takeoff	-4.2°
Cruise	+0.5°
Landing	-2.2°

Table 16 Elevator deflection for each trimmed configuration

E. Static Stability Derivatives

The static stability derivatives of the plane at trimmed were calculated using AVL. All stability derivatives as shown below in Table 10 have the corresponding signs that indicates positive stability.

Case	$\frac{\partial C_m}{\partial \alpha}$	$\frac{\partial C_n}{\partial \beta}$	$\frac{\partial C_l}{\partial \beta}$
Cruise	-0.633	0.220	-0.085
Landing	-0.828	0.231	-0.207
Takeoff	-1.052	0.234	-0.174

Table 17 Stability derivatives at MTOW

From Table 17, the pitch and roll stability derivatives are both negative which indicates a restoring moment towards equilibrium. The positive sign of the yaw stability derivative indicates a directional restoring moment towards equilibrium.

When using the assumption of $\frac{\partial C_l}{\partial \alpha} = 2\pi$ for the linear region in polar diagrams (not past the stall angle), the static margin can be estimated with Equation (69)

$$SM = -\frac{\frac{\partial C_m}{\partial \alpha}}{\frac{\partial C_l}{\partial \alpha}} = -\frac{\frac{\partial C_m}{\partial \alpha}}{2\pi} \tag{69}$$

Before shifting the location of the wing 2.5 ft forward, the longitudinal stability derivative for each case fell around -3, resulting in a static margin of about 0.48, indicating the plane was extremely over-stable and lacked pitch control. This is what led to making the decision to shift the wing forward in order to shift the neutral point forward and decrease the static margin. This caused the stability derivatives to decrease in magnitude, and led to the static margins and neutral point locations for each configuration at MTOW listed in Table 18.

Case	SM	x_{NP} [ft]
Cruise	0.101	16.87
Landing	0.132	17.11
Takeoff	0.167	17.40

Table 18 Static margins for each condition at MTOW

These static margin values fall within a more reasonable range of 0.10 to 0.20, which indicates enough stability to allow the plane to remain in equilibrium while allowing for adequate pitch control. This justifies the repositioning of the wing.

VIII. Propulsion System

In an ideal aircraft design, our designated propulsion system would be a distributed electric propulsion system. In the proposed aircraft, the idea of using an electric-based engine was highly considered. However, in order to support a fully electric aircraft, a significant amount of weight and volume would have to go towards batteries. However, many experts observe that roughly every 23 years, the battery energy density tends to double. As of the year 2020, the battery energy density for a typical aircraft was at around 228 Wh/kg. Researchers at the Warsaw University of Technology[22] expect that the battery energy density in 2035, the target year would reach 361.1 watt hours per kilogram. The projected battery growth is shown below:

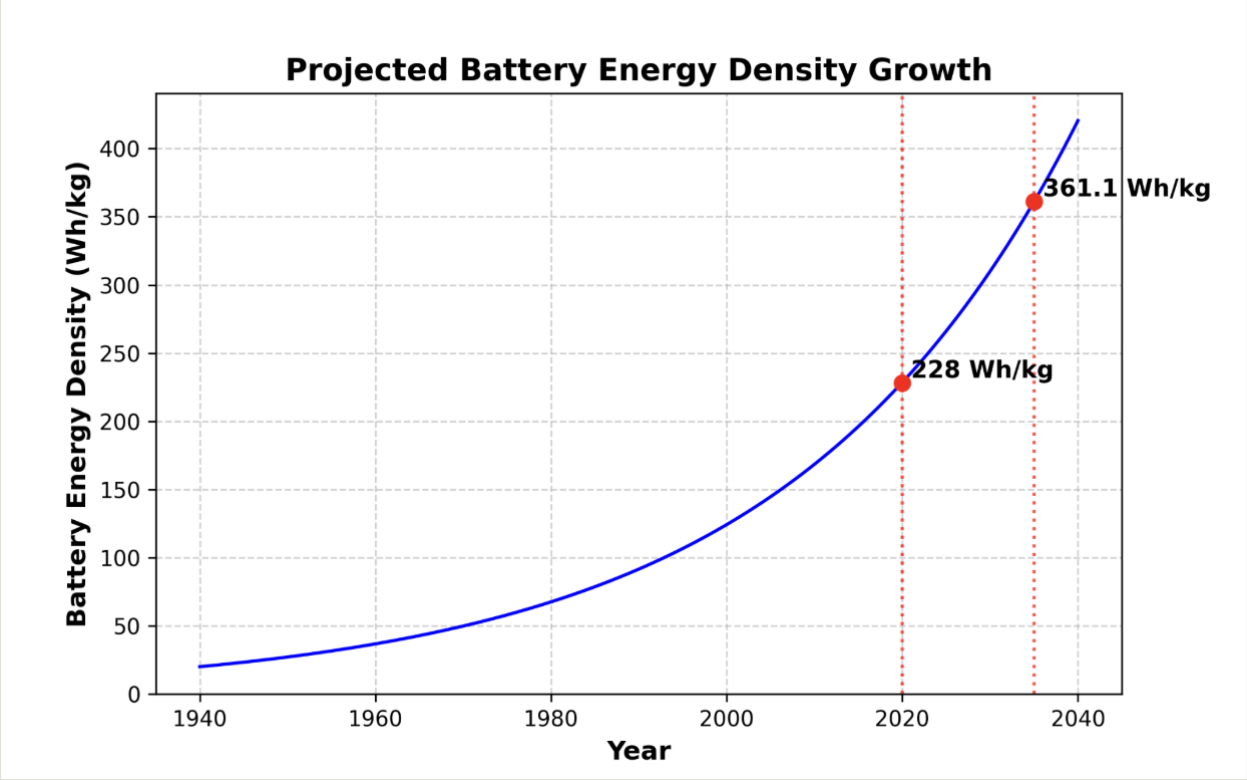

Fig. 28 Battery Energy Density Projected Growth

As battery energy density grows over time, we believe the prospect of using a fully electric powertrain would become more realistic. However, for the time being, our chosen powertrain is a series-parallel hybrid design. In a series-parallel hybrid design, the powertrain can combine the features of both a series hybrid design and a parallel hybrid design. This allows the aircraft to operate as a series hybrid, running a more efficient and simplified design, while also being able to operate as a parallel hybrid, where gas and electric power can function simultaneously, improving output. Furthermore, the series-parallel hybrid supports regenerative braking, where an electric motor can act as a generator during various flight conditions. This could help charge the battery during the flight, in a similar manner to a Toyota Prius.

When considering the fully electric propulsion candidate, the plane design settled on using a distributed electric propulsion system with twelve separate aircraft engines. With a distributed system, the RPM of the engines can vary and be optimized for the current flight conditions. This removes the need for a gearbox, resulting in the fully electric design using the powertrain as shown in Figure [29].

In the hybrid design, the proposed powertrain architecture is a series-parallel hybrid design, as shown in Figure [30]. Due to the battery density value, we chose the hybridization ratio to be 50/50. As a result, both the shaft ratio ϕ and supplied ratio Φ are equal to 0.5.

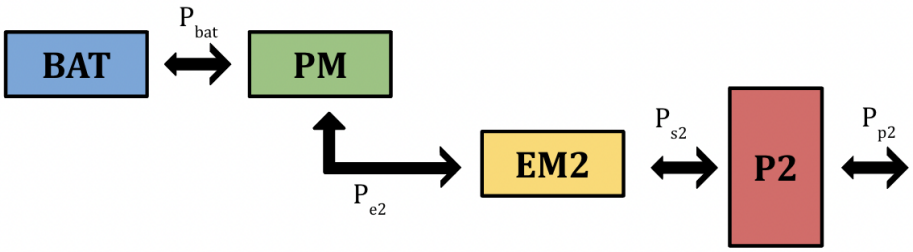

Fig. 29 Electric Powertrain Block Diagram

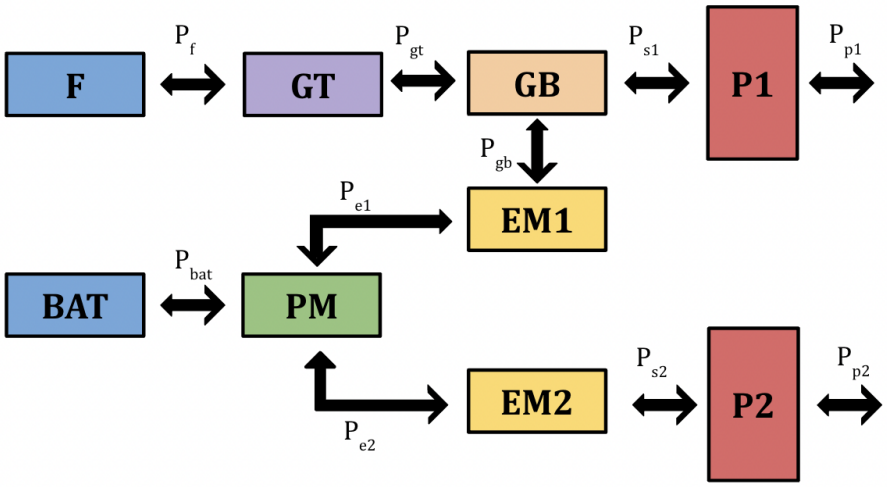

Fig. 30 Hybrid Powertrain Block Diagram

With respect to prior designs of the CD-4, the hybridization ratio was chosen arbitrarily as 50 percent, and with the findings seen in 31 a hybridization percent of 10 percent to maximize our goal of minimizing the MTOW of the aircraft. This decision was made based on two different pieces of evidence found. The first is looking at the hybridization Figure 31 the approximate increase in MTOW with respect the hybridization ratio increases dramatically at a rate of approximately 5 to 1 in some comparable regions of the graph. This means that for a small increase in battery weight, and with that hybridization percent, the total MTOW goes up 5 times that amount. This has led to decreasing the percent hybridization and minimization as low as possible.

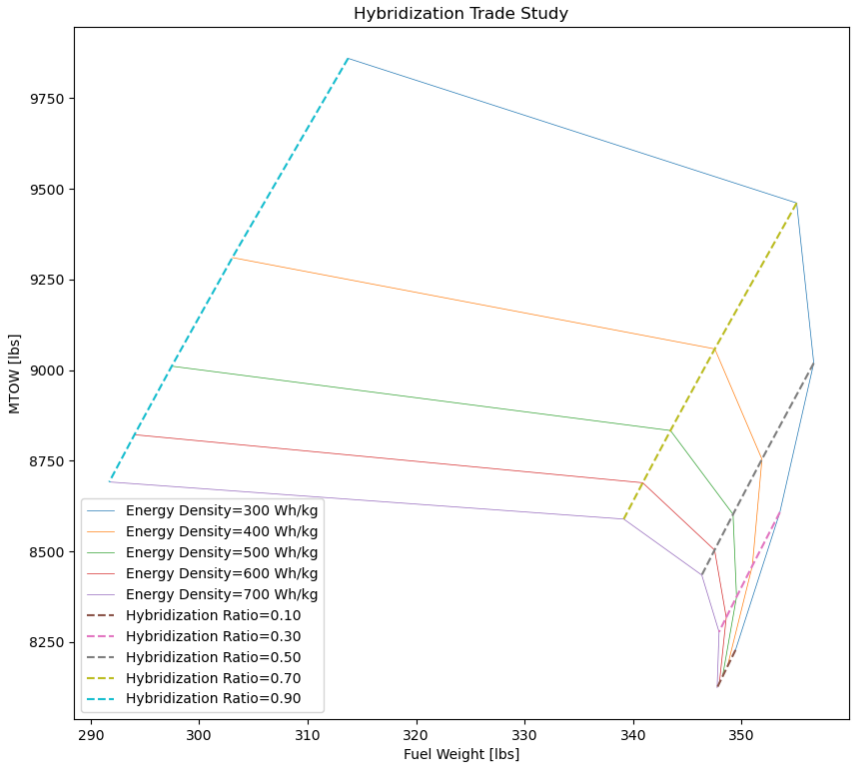

Fig. 31 MTOW vs Fuel Weight with respect to Hybridization Percent

This decision is further reinforced by looking at the energy density curves on Figure 31 which shows that even with a significant increase in energy density, exceeding those of the expected energy densities shown in 2035 by prior reports, there is not enough benefit with respect to the ratio of how much MTOW is gained versus the hybridization percent. Only if energy densities in batteries incredibly succeed the expectations of the estimate, it will become hard to justify the weight increase unless an entirely different system can be made. The second part of this decision was made based on the possible applicable benefits of the hybridization system within the CD-4, namely the increase amount of lift produced by the distributed propulsion system. As a result seen in Equation 5 and 6 the total usage of the propulsive lift system was chosen to be limited to only the climb, maneuvering/working and takeoff sections of the mission profile where it was most beneficial. This minimizes the required amount of hybridization percent, and in turn reduces the MTOW grossly.

We chose to keep the distributed electric propulsion system as in the electric design. A distributed electric propulsion system is common in electric-powered aircraft, and in our aircraft, a total of 10 electric aircraft engines are distributed along the length of the main wing. This results in better engine efficiency in addition to lower noise pollution. Furthermore, the addition of a distributed propulsion system results in a mitigated vortex trail, improving lift performance, stability, and control.

For the gas turbine portion of the hybrid design, we sized the gas engine to match the dimensions of current models in the industry with similar power outputs. We chose to use the Pratt and Whitney PT6A-15AG engine from the AT-402B, which generates 680 hp. This allows the aircraft to rely solely on the gas engine to reduce the size of the batteries. By integrating this engine into a parallel hybrid configuration, it allows the engine to supply electric power to the two battery packs, which will power the distributed electric propulsion system on the wings, allowing for greater fuel efficiency.

For the fully electric system, the powertrain contains batteries, a power management and distribution system, electronic motors, and propellers. Using Table 5.4 in the “Preliminary Sizing Method for Hybrid-Electric Distributed-Propulsion Aircraft” research report [23], the efficiencies for components were found: 0.99 for the power management

and distribution system and 0.96 for the electronic motors. The battery efficiency is 0.95, while the fuel efficiency varies based on the type of fuel and its energy density but averages around 0.55. Lastly, the efficiency for the propeller is 0.85.

The hybrid system is more complex, with both fuel and batteries running together. In addition to the power management and distribution system and the electronic motors, which are similar to the electric system, this system also has a gas turbine to transfer energy from the fuel to the gearbox. From the gearbox, the energy is distributed either to the propeller or back to the electric motor to charge the batteries. The efficiencies for components were selected to be 0.99 for the power management and distribution system, 0.96 for the electronic motors, and 0.96 for the gearbox. For fuel efficiency, a value of 1 was used for the gas turbine. The fuel efficiency for the electric part is the same as in the electric system, 0.55. The battery efficiency is also the same at 0.95. Regarding the gas turbine, the value varies based on the type of gas turbine chosen, but an average overall value of 0.4 was used. For the propeller, the efficiency remains the same for both systems at 0.85.

As shown in Figures 29 & 30, several arrows depict the flow of power between the components of the aircraft engines. The arrows are double-sided, indicating that power can flow both to and from the components. Figure [30], which illustrates the hybrid powertrain design, contains a total of ten arrows, each representing a distinct magnitude of power transfer within the powertrain components. Additionally, one side of each arrow is more prominent than the other. In the diagram and the accompanying equations, we assume that energy flows from the less prominent side to the more prominent side. Consequently, if a power value is negative, it indicates that the flow of power is in the opposite direction of the assumed energy flow.

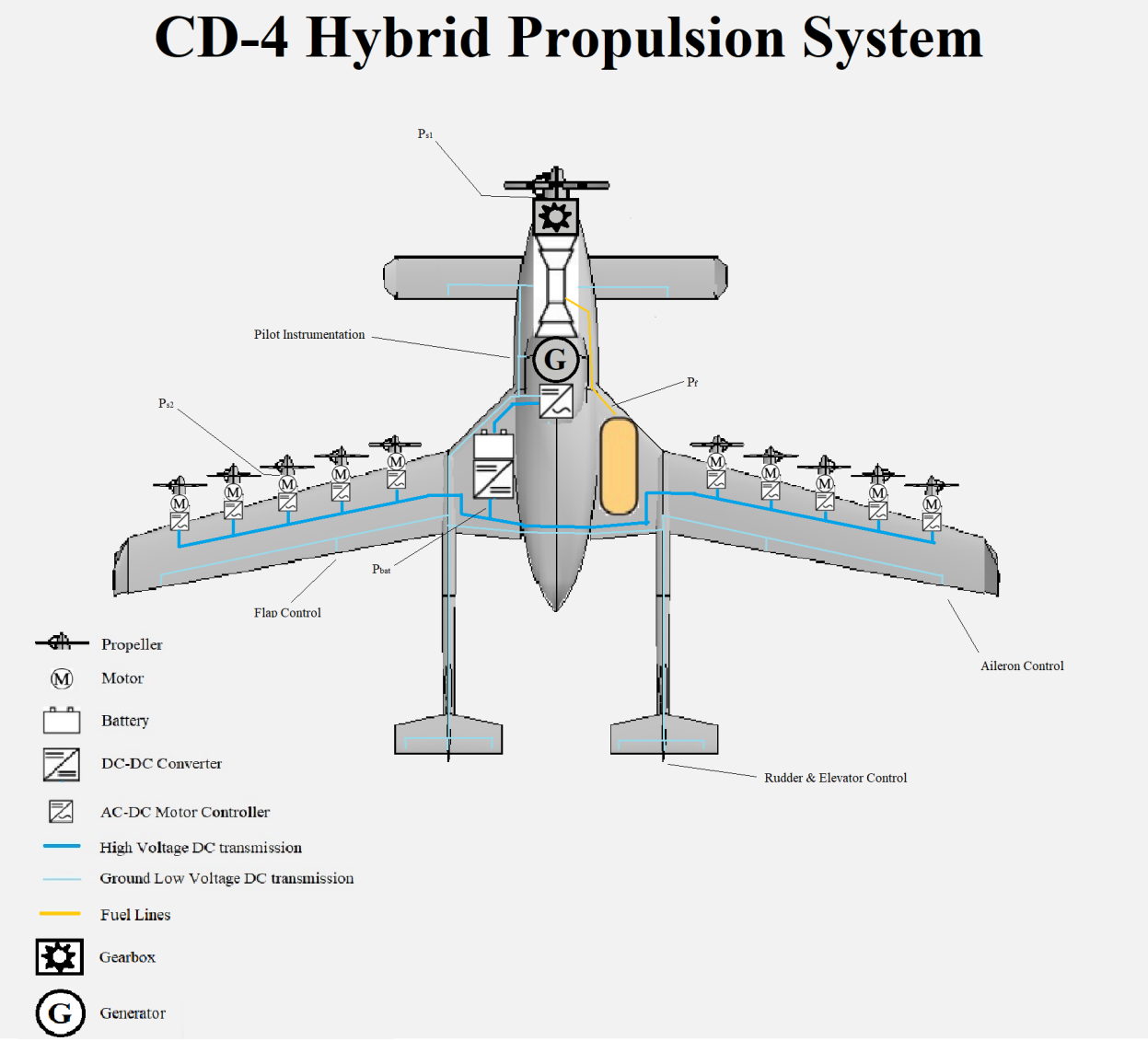

Fig. 32 Hybrid Electric Propulsion

Here is a hybrid propulsion system layout and routing of the aircraft. The aircraft utilizes a parallel-series hybrid system which allows the use of either gas or electric propulsion operation. All power is provided through the use of a large renewable resource gas tank, as well as 2 batteries for the distributed electrical propulsion close to the cargo storage in order to decrease it's affect on aircraft roll performance and structure requirements. All high voltage lines will run on the battery cell with the ability for the plan to use the gas turbine engine to charge the battery cell if required. All low voltage lines are handled by the gas turbine's rectifier of low voltage energy, however in the case of an emergency, routing can be switched to the ground low voltage DC system of the distributed electrical propulsion system.

IX. Sustainability

Currently, the design of agricultural aircraft presents significant challenges in achieving an optimal balance between lifecycle cost, maintainability, and environmental sustainability. The industry must confront the environmental impact of both materials and operational practices while maintaining economic feasibility for farmers. The following section outlines these key challenges and explores potential solutions informed by recent research and emerging technologies.

A. Material Selection

Fiberglass composite was selected as the primary structural material for the CD-4 Cybertruk agricultural aircraft. This decision follows a comprehensive comparison between carbon fiber and fiberglass composites, evaluating factors such as strength, weight, cost, and overall suitability for agricultural applications. While carbon fiber offers superior strength-to-weight and stiffness-to-weight ratios, its significantly higher cost, ranging from $20 to $100 per pound compared to fiberglass's $1.80 to $5.85, thus makes it less viable for this project. The price gap becomes even more pronounced when considering aerospace-grade carbon fiber. In contrast, fiberglass composite provides a favorable balance between performance and cost-effectiveness. By choosing fiberglass, the goals to maintain environmental and operational efficiency while ensuring the aircraft remains accessible and affordable for farmers are supported. [24] [25] [26] [27]

Fiberglass composite material offers a lightweight yet durable solution for agricultural aircraft, enhancing payload capacity, fuel efficiency, and enabling more versatile mission profiles. Its inherent corrosion resistance makes it well-suited for chemical-intensive environments, contributing to extended airframe lifespan and reduced maintenance requirements. Unlike metallic materials, fiberglass is resistant to fatigue cracking, further improving structural longevity. However, repairs can be complex, often requiring specialized skills and materials, which may increase downtime and associated costs. Additionally, prolonged exposure to UV radiation and moisture can cause material degradation, necessitating the use of protective coatings and regular inspections. While fiberglass enhances aerodynamic performance and operational durability, its relatively high initial cost and limited recyclability remain key challenges to broader adoption in primary airframe structures. Nonetheless, its performance advantages make it a strong candidate for sustainable and efficient agricultural aviation. [11]

In addition to fiberglass being selected as the primary material for the aircraft, steel alloy is utilized for several critical components due to its advantageous mechanical properties. First, it is used in the landing gear and structural joints because of its high tensile strength, which ensures reliability under significant loads. Second, the exhaust system employs steel alloy for its excellent thermal resistance, typically ranging from 800°F–1500°F. Third, steel was chosen for the fuel tank, not only for its corrosion resistance, which fiberglass also offers, but for its superior structural durability. Fourth, steel alloy is used in the wing spars, where it helps optimize the strength-to-weight ratio in load-bearing areas and effectively resists deformation under aerodynamic stress. Lastly, all fasteners are made from steel alloy due to its high shear strength and the ability to achieve extremely precise manufacturing tolerances. [10] [28] [29]

B. Maintainability/Modularity Designs

Although the CD-4 Cybertruk is expected to have a long service life, estimated at approximately 35 years, thanks to the use of fiberglass composite combined with ceramic/epoxy coatings (compared to the typical 20–30 years for agricultural aircraft), many of the major components have been designed to be modular. This modularity facilitates easier replacement and repair, ultimately reducing downtime and lowering maintenance costs. [30]

The modular hybrid powertrain of the CD-4 Cybertruk ensures ease of maintenance while balancing performance and redundancy. The gas turbine and distributed electric propulsion system are strategically positioned for accessibility, allowing for straightforward inspections and repairs. The gas engine can operate independently if the electric system fails, minimizing downtime during critical missions. Additionally, the battery system is designed for quick swapping, leveraging projected advancements in energy density (targeting 361 Wh/kg by 2035) to reduce weight and improve serviceability over time.

Simplified mechanical systems contribute to the aircraft's low-maintenance design. The fixed landing gear, optimized for rough-field operations, eliminates the complexity of retractable systems while maintaining durability. The ten electric motors, each weighing just 10 lbs, are individually replaceable without major disassembly, reducing repair times. This modular approach ensures that maintenance crews can address issues efficiently without extensive downtime.

C. Fuel Efficiency Improvements

The CD-4 Cybertruk incorporates several design features to maximize fuel efficiency while maintaining performance. The aircraft's aerodynamically optimized winglets reduce induced drag by suppressing wingtip vortices, improving lift-to-drag ratio and lowering fuel consumption during cruise. The hybrid-electric propulsion system combines a turboprop engine with distributed electric motors, allowing the aircraft to operate in fuel-efficient modes during low-power phases of flight. Additionally, the lightweight fiberglass composite airframe reduces overall weight compared to traditional aluminum structures, further decreasing fuel demands.

D. Reduced Enviromental Impact

Beyond fuel efficiency, the CD-4 significantly reduces environmental impact through precision agriculture technologies. The onboard spectral imaging and AI-driven spray system analyzes crop health in real time, enabling targeted application of pesticides, fertilizers, and water. This minimizes chemical runoff and over-spraying, reducing both operational costs and ecological harm. The hybrid propulsion system also cuts emissions by supplementing the gas turbine with electric power, particularly during low-altitude spraying where efficiency is critical. Combined with sustainable aviation fuel (SAF) compatibility, the CD-4 offers a cleaner alternative to conventional agricultural aircraft.

E. Emission

To address sustainability goals regarding fuel emissions, the CD-4 Cybertruk incorporates the use of Sustainable Aviation Fuel (SAF), specifically the ones that can be derived from renewable feedstocks such as waste oils, agricultural residues, or biomass, can reduce life cycle carbon emissions by up to 80% when compared to conventional Jet-A fuel, depending on the specific production pathway. During operation, although tailpipe CO2 emissions remain similar to fossil-based fuels, the overall well-to-wake emissions are significantly lower due to the biogenic carbon cycle. For typical agriculutural flight profiles, using a 50% SAF blend can yield an estimated 30% to 40% reduction in carbon dioxide emissions per mission. [5]

X. Structures

The structural design of the CD-4 CyberTruk was developed to maximize durability, operational reliability, and weight efficiency while ensuring compliance with safety and performance requirements. We implemented fiberglass composite material because of its ideal strength-to-weight ratio and excellent corrosion resistance, which makes it well suited for environments with frequent chemical exposure [11]. This material choice also reduces fatigue-related failures, extending the aircraft's service life compared to traditional metallic airframes [11]. We selected a high-wing configuration to provide direct load paths from the wings to the fuselage while improving ground clearance for spraying operations. The twin-boom tail enhances yaw stability and allows easier access to the rear payload bay for faster turnaround between missions. The canard surfaces were reinforced to support aerodynamic loads during low-speed maneuvers and to compensate for CG shifts. Additionally, the fixed steel alloy landing gear was designed to handle rough-field operations, prioritizing durability and ease of maintenance.

Structural sizing was based on primary aerodynamic and ground load cases, including maneuver loads designed for +3.8g and -1.52g, consistent with industry practice and FAR Part 23 design standards as discussed by Roskam [12]. Gust loads and landing impacts up to 10 ft/s were also considered. A factor of safety of 1.5 was applied to ensure structural integrity under ultimate load conditions. The structural weight fraction of the airframe was estimated at approximately 25 percent of maximum takeoff weight, aligning with common benchmarks for agricultural aircraft [12]. Internal structural components such as spars, ribs, and bulkheads were arranged to efficiently distribute loads while minimizing weight.

The distributed propulsion system, including multiple electric motors mounted on the wings and canards, was structurally integrated with reinforced mounting points. This modular design supports maintainability and future scalability. Overall, the CD-4's structural design achieves a balance of strength, weight efficiency, and operational durability. Structural analysis verified that the aircraft meets the required load cases for maneuvering, gusts, and landing, ensuring reliable performance in demanding agricultural environments. The combination of materials, layout, and modularity further enhances long-term value [20].

A. Vn Diagram

An essential factor in determining the structure and design of an aircraft is the V-n Diagram. A V-n diagram exhibits the structural limits and capabilities of an aircraft through displaying the aircraft's operating limits in addition to the effects of gusts. In the diagram, there is a defined region, which represents the region of safe flight. This region is defined through a curve, which is found later in addition to the maximum structural speed and the maximum and mimimum load factor for the aircraft. When the aircraft's load factor passes the limits set by the curves, the aircraft enters the stall region, resulting in a massive spike in drag and a loss in the maneuverability of the aircraft. When the aircraft goes past the structural load limits and velocity limits, the aircraft would experience structural damage, with risk of absolute failure. Furthermore, when the aircraft's speed passes the cruise speed of the aircraft, the aircraft would enter a cautionary range, where the structure of the aircraft experiences a greater stress.

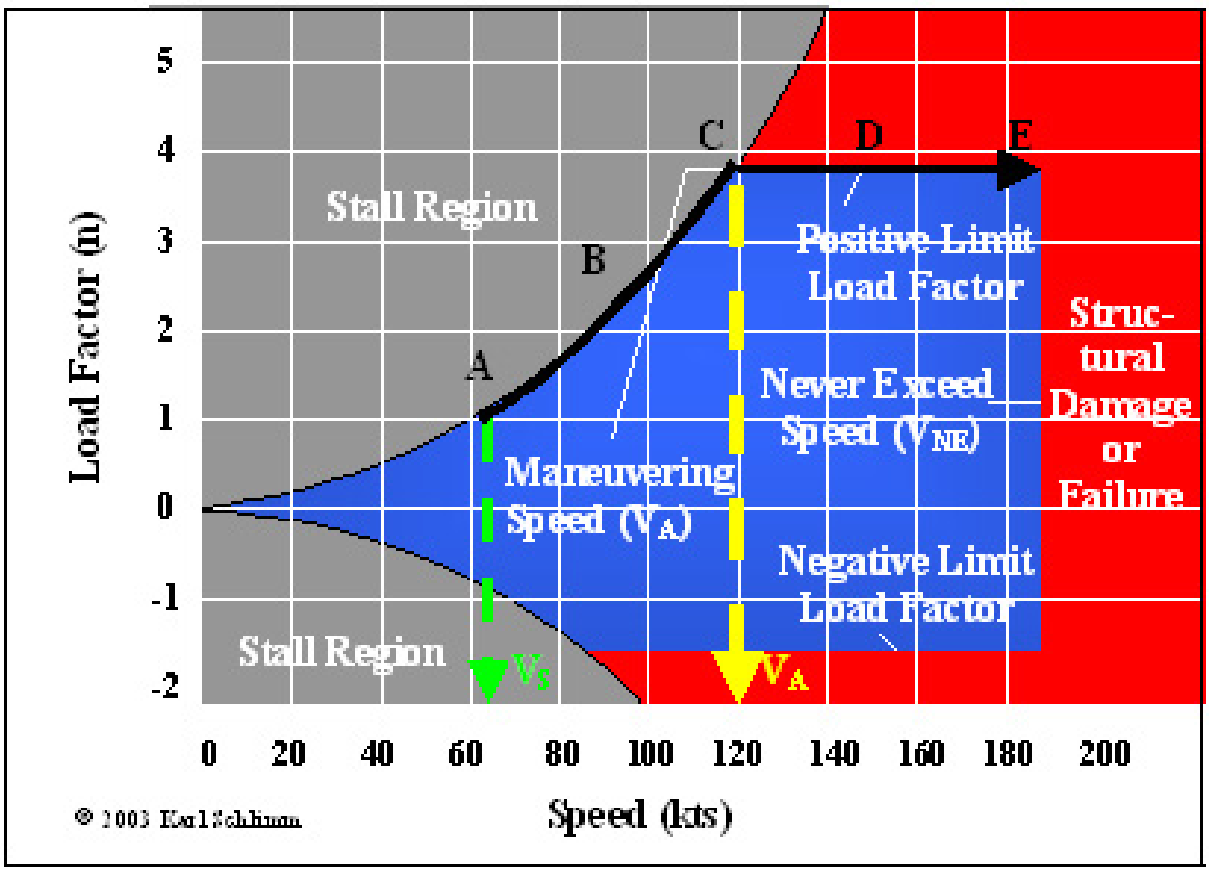

Fig. 33 Vn labeled Diagram

There are several key values needed in determining the V-n diagram. As mentioned before there is an upper and lower load limit. For a utility-based general aircraft, Raymer defines the upper load limit to be 4.4 g's and the lower load limit to be -1.8 g's. There are also several key velocities. The upper speed limit is defined as the maximum speed the aircraft's structure could support, shown as V_D in the V-n diagram. The RFP defines this speed as 250 kts, or 441 ft/s. The cruise speed, or V_C, defines the velocity from which the aircraft enters a caution range. We defined this velocity to be 180 kts, or 303 ft/s. V_S, or the stall speed is another essential velocity. It is minimum speed at which a 1-g load at level flight can be achieved. The equation for the stall speed is shown below.

$$V_s = \sqrt{\frac{2W}{\rho S C_{L_{\max}}}} \tag{70}$$

V_A and V_G were determined similarly. These velocity are representative of the minimum speed at which the maximum and minimum load factors can be experienced. The equation to determine the velocity is shown below

$$V = \sqrt{\frac{n \cdot 2\left(\frac{W}{S}\right)}{\rho_{\text{SL}} C_L}} \tag{71}$$

Finally, V_B, or the gust alleviation speed is the maximum speed at which deflection can be made without exceeding the maximum load factor. The velocity is determined through the following equation.

$$V_B = V_S \sqrt{1 + \frac{K_g U_{e,B} V_C C_{L_\alpha}}{498\left(\frac{W}{S_{\text{ref}}}\right)}} \tag{72}$$

where

$$\mu = \frac{2\left(\frac{W}{S}\right)}{\rho\, c\, C_{L_\alpha}\, g} \tag{73}$$

$$K_g = \frac{0.88\mu}{5.3 + \mu} \tag{74}$$

$$C_{L_\alpha} = \frac{C_{l_\alpha}}{1 + \left(\frac{C_{l_\alpha}}{\pi\, AR\, e}\right)} \tag{75}$$

In order to define the two curves in the V-n diagram, the equation to determine velocity was transformed to determine the load factor based on a changing velocity. The equation is shown below as follows.

$$n = \frac{\rho_{\text{SL}} V^2 C_L S}{2W} \tag{76}$$

For the upper load limit, C_L was set to its maximum value, while for the lower load limit, C_L was set to its minimum value. In addition to the structural loads, the load limits may be affected by gusts or turbulence. To account for gusts, the following gust load factor equation is used.

$$n = 1 \pm \frac{K_g\, C_{L_\alpha}\, U_{de}\, V}{498\left(\frac{W}{S}\right)} \tag{77}$$

The relative gust speeds were determined from the FAR 23 guidelines as follows:
$U_{eB} = 66 ft/s\ U_{eC} = 50 ft/s\ U_{eD} = 25 ft/s$
Finally, with all portions of the V-n diagram determined, two separate graphs were created. The first is for the maximum takeoff weight of 7460 lb, and the second is using the mimimum operational weight of 5122 lb. As shown in the following two figures, the wind gusts and turbulence has a lower effect at a higher weight, with the gusts not affecting the load factor limits nearly as much in the higher weight compared to the lower weight. Additionally, while the cruise and max speed is constant based on weight, some of the other key speeds vary from one weight to another. The following table compares these speed values for the maximum and minimum weights.

Table 19 Aircraft Key Speeds at Different Weights

Speed	**Symbol**	**7460 lb** (ft/s)	**5122 lb** (ft/s)
Stall Speed	V_S	102	85
Maneuvering Speed	V_A	215	178
Gust Penetration Speed	V_B	273	258
Cruise Speed	V_C	303	303
Dive Speed	V_D	421	421
Max Gust Speed	V_G	212	176

When looking at the max speed, or V_D, we found it to be at 421 ft/s, or 250 kts regardless of weight. This speed is also known as the max dive speed of the aircraft. Typically, in an aircraft, 90-95% of V_D is the Never Exceed speed for the aircraft, as the loads and stresses the components face are reaching more dangerous levels. The second the speed of an aircraft passes its max dive speed, it would result in failure in the aircraft' structure due to the loads and stress experienced.

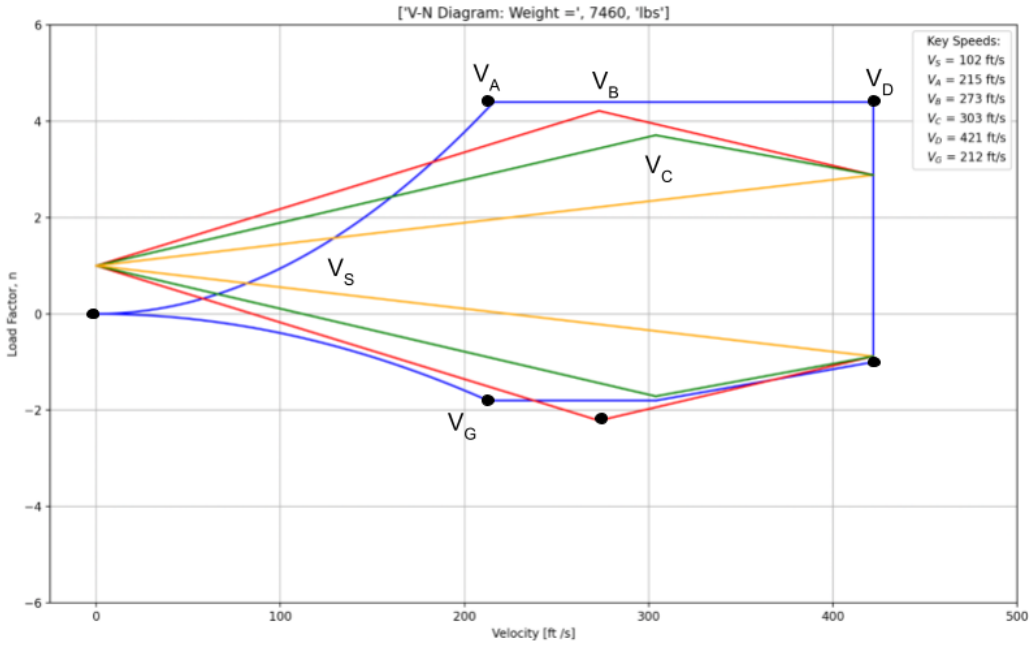

Fig. 34 Vn Diagram MTOW

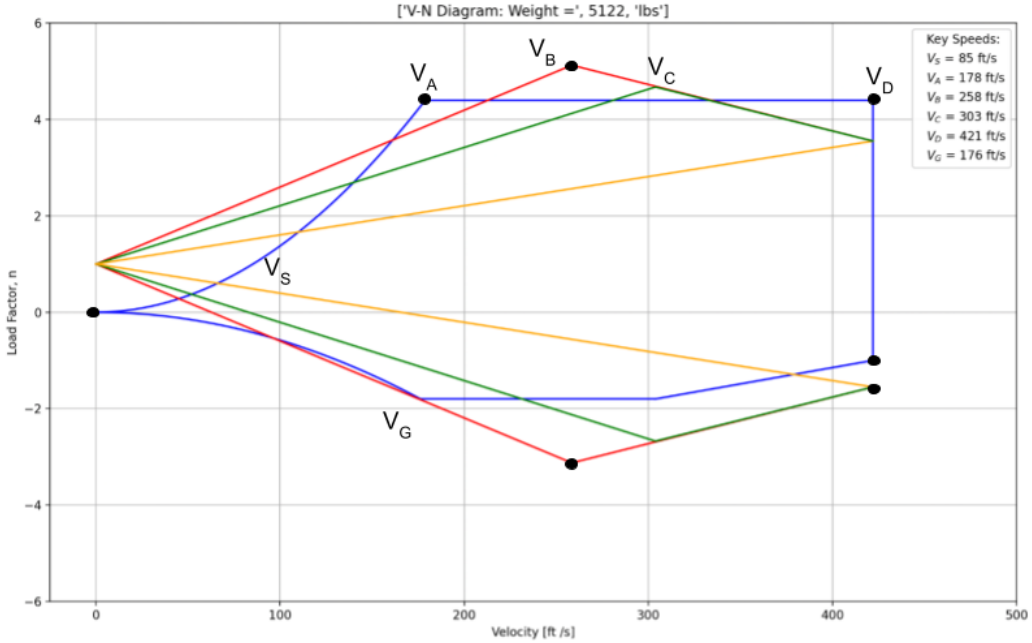

Fig. 35 Vn Diagram Lower Operational Weight

XI. Landing Gear

A. Overall Configuration

Number of Main Gear Struts: For the CD-4 Cybertruk, a tricycle landing gear configuration is chosen since it fit best with the overall design of having the wing and the center of gravity in front of the leading edge of the wing.
Number of Tires Per Strut: One tire per strut was selected to support the static and dynamic load of the whole aircraft
Tire Size: With the max take off weight of the CD-4 Cybertruk is 7460 lbs, another 10% of the weight is added on top of the original weight to satisfy the 7% safety factor from FAR 25 and allow for growth on the aircraft design later on. Thus the weight will be used for calculation is 8019 lbs.

For worst case load calculations. After doing geometric analysis, the following results were achieved:

- Horizontal distance from the nose landing gear to the AFT C.G (N_a) is 157.5 inches.
- Horizontal distance from the main landing gear to the FWD C.G (M_f) is 61.3 inches.
- Horizontal distance from the main landing gear to the AFT C.G (M_a) is 32.5 inches.
- Horizontal distance between the nose landing gear and the main landing gear is 190 inches

These following equations are then used to calculate worse case loads along with the results:

$$(\text{Max Static Load})_{\text{main}} = W\frac{N_a}{B} = 7460lb \tag{78}$$

$$(\text{Max Static Load})_{\text{nose}} = W\frac{M_f}{B} = 3460lb \tag{79}$$

$$(\text{Min Static Load})_{\text{nose}} = W\frac{M_a}{B} = 1835lb \tag{80}$$

$$(\text{Dynamic Braking Load})_{\text{nose}} = 0.31\frac{H}{B}W = 1116.4lb \tag{81}$$

$$\text{Note:} \quad \frac{M_a}{B} > 0.05 \quad \text{and} \quad \frac{M_f}{B} < 0.20 \tag{82}$$

For tire size, an assumption of general aviation for A and B was used in the below equation. Thus the minimum required tire size for the main landing gear and the nose landing gear are:

$$(\text{Tire size})_{\text{main}} = A \times W_W^B = 1.51 \times 4692.5^{0.349} = 28.9inches \tag{83}$$

$$(\text{Tire size})_{\text{nose}} = A \times W_W^B = 1.51 \times 1116.4^{0.349} = 17.5inches \tag{84}$$

The requirement for $\frac{M_a}{B}$ is satisfied with a result of 0.171, but the requirement for $\frac{M_f}{B}$ is not satisfied, a result of 0.323 was achieved. Thus, the static load on the nose landing gear is greater than 10%, to compensate for this, a larger tire was chosen for the nose landing gear. Our final tire sizes are 25 inches in diameter for the nose landing gear and 35 inches in diameter for the main landing gear.
Braking Kinetic Energy Calculation: The following equation is used to calculate the total energy required under braking from FAR 23.735:

$$\text{KE}_{\text{braking}} = \frac{1}{2}\frac{W_{\text{landing}}}{g}V_{\text{stall}}^2 = 111,700\text{ft-lb} \tag{85}$$

The braking force per tire can be calculated using the following equation:

$$\text{KE}_{\text{braking force}} = \frac{W \times R_{\text{tire}}}{N} = 59,783\text{ft-lb per tire} \tag{86}$$

In total, for two wheels, we have 119,567 ft-lb braking force estimated, and a requirement of 111,700 ft-lb of braking force needed. This is barely above the sizing requirements, but this is for the MTOW instead of 80 or 90 percent of the MTOW.

Tire Choice: The sizing of the wheels were choosing based on recommended width and thickness of the tires from Goodyear in according to use case and aircraft size. With this according to the Goodyear Tire we have a 24x7.25 Front Tire, suitable for Nose Gears, and a 35x10 tire for the rears, which do NOT have landing gear, and as such get a much thicker tire to compensate. The Goodyear Tire Table [5] a list of aircraft, their front and main landing gear, as well as their load, including landing speed, braking load, and MTOW. Tire weight individually was taken from sellers [6] and historical weights for similar sized tires[7]. With 35 inches of diameter for the main landing gear, there is more than adequate room for large brakes.

Struts and Suspension: We chose a Tricycle Design as the mounting points aligned with the strongest points of the chassis, and used hard mounted struts in the rear with a front cantilever suspension nose gear. The front suspension has a caster angle of 7 degrees, and has a telescoping suspension range of 13 inches of travel.

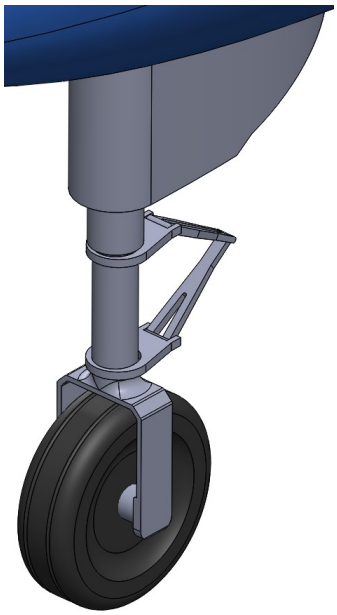

Fig. 36 Isometric View of Front Landing Gear

The front landing gear is mounted underneath the engine which is already supported by the chassis of the plane itself.

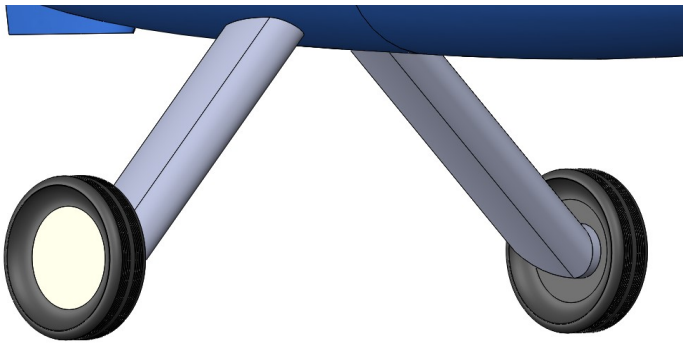

Fig. 37 Isometric View of Rear Landing Gear

The rear strut suspension is robust, cheap, and light. The struts are air profiled for a reduction in drag. In addition the structure goes straight below where the payload is mounted to the plane, and thus is near a strong structural member.
z

B. Specific Location

Longitudinal Tip-over Criterion: The longitudinal tip-over angle for the CD-4 Cybertruk is 16 degrees, and this satisfy the minimum of 15 degree requirement for this criterion.

Longitudinal Ground Clearance Criterion: The longitudinal ground clearance angle for the CD-4 Cybertruk is 22 degrees, and this satisfy the minimum of 15 degree requirement for this criterion.

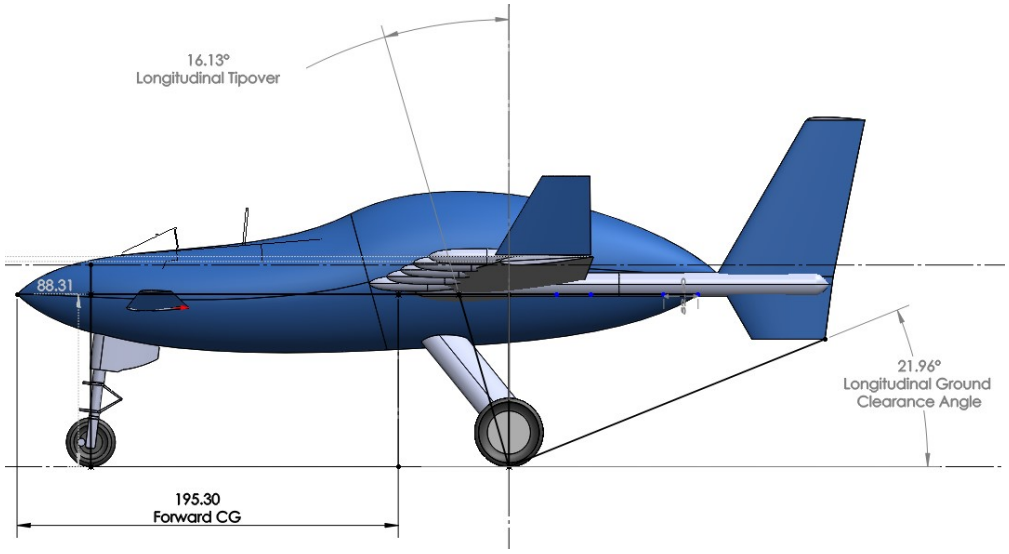

Fig. 38 Side view of the CD-4 with geometric analysis

Lateral Tip-Over Criterion: The lateral tip-over angle for the CD-4 Cybetruck is 49 degrees, and this satisfy the maximum 55 degree requirement for this criterion.

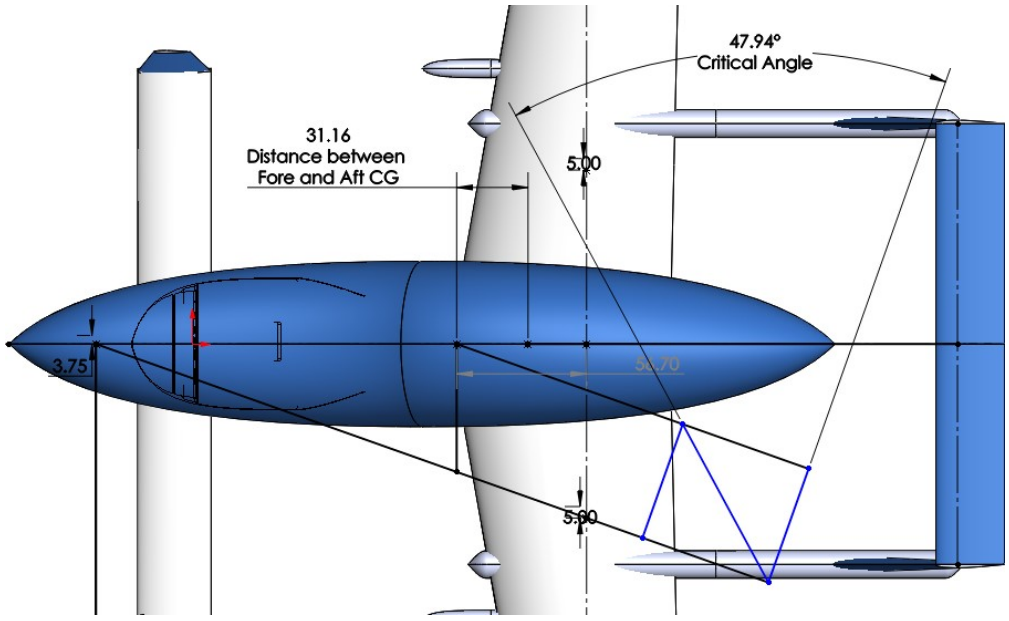

Fig. 39 Top view of the CD-4 with geometric analysis

Lateral Ground Clearance Criterion: The lateral ground clearance angle for the CD-4 Cybertruk is 18 degrees, and this also satisfy the minimum 5 degree requirement for this criterion.

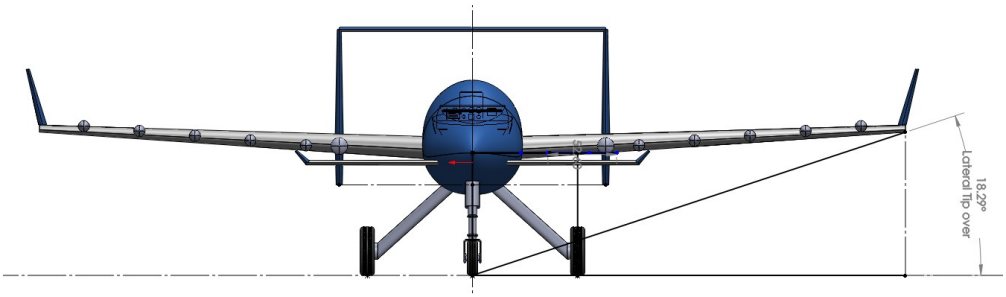

Fig. 40 Top view of the CD-4 with geometric analysis

XII. Interior Layout

The requirements for an agricultural aircraft fall under FAR 23.771 Pilot compartments which outline that the pilot's view must be free of glare, protected from the elements, and methods of adjusting the internal temperature and humidity. A number of other requirements are in place, such as the type of material, the temperature resistance of the materials, as well as the small details of all controls and their sizes which will be omitted for the sake of simplicity in this design review. Instead the largest factors will be concerned, such as those in FAR 23.771 regarding the pilot, the cockpit layout, and the plane's structural interior layout.

A. Pilot and Cockpit

All dimensions, unless otherwise written are in inches and degrees.

Fig. 41 Cockpit Side View

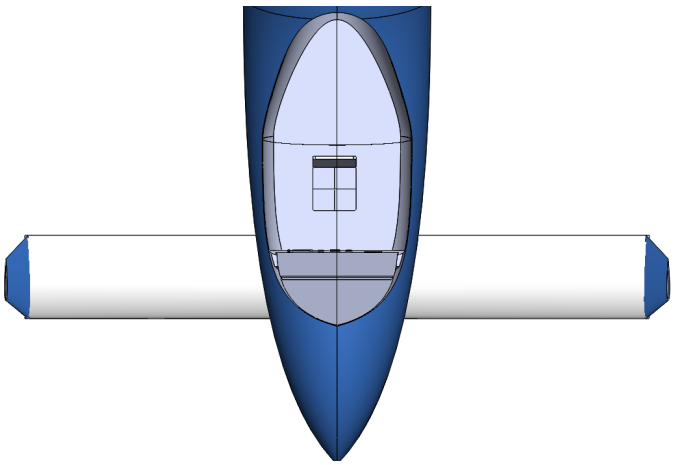

Fig. 42 Cockpit Top View

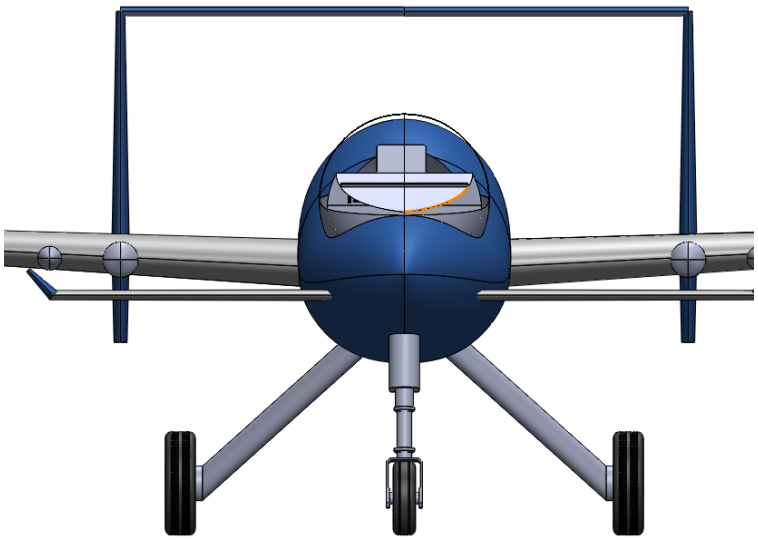

Fig. 43 Cockpit Front View

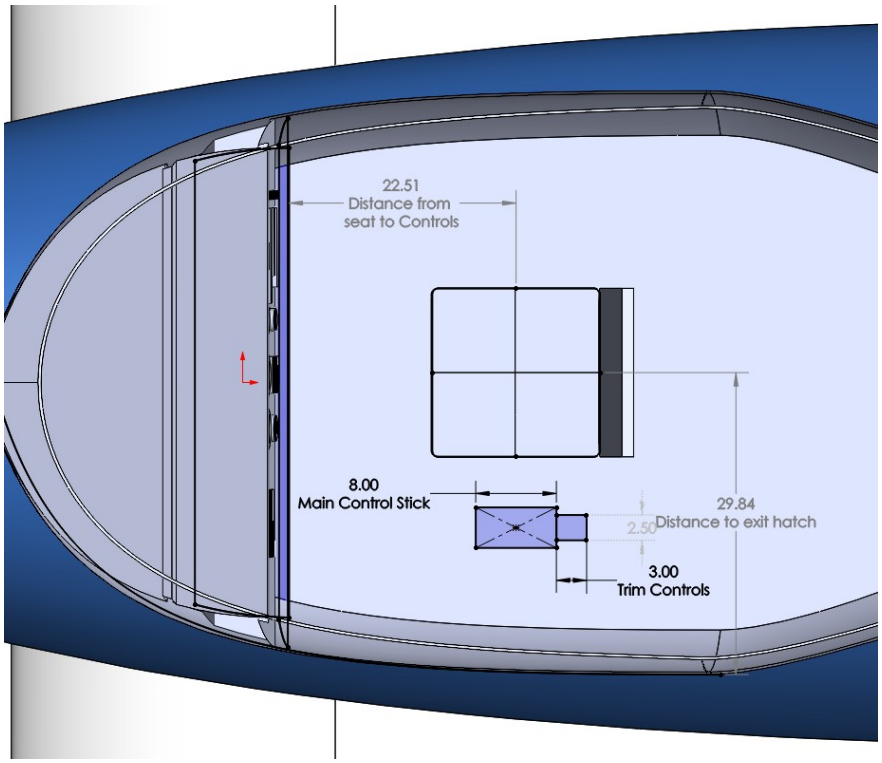

Fig. 44 Cockpit Top Cross Section View Layout

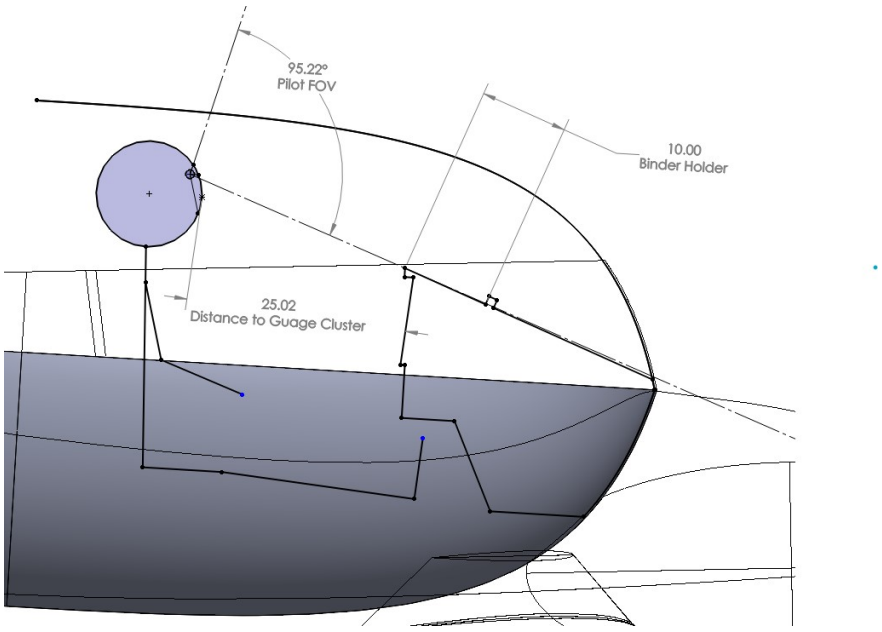

Fig. 45 Cockpit Side Cross Section View Layout

The canopy is made of a large acrylic half dome which is located as far forward in the aircraft to gain a better view of the terrain ahead, and will be reinforced with a roll cage to protect during crashes. In addition the configuration of the cockpit was laid out to be ergonomically safer due to the fatigue that an agricultural aircraft pilot faces. The rough estimate is taking of the average pilot in reference to the Request For Proposal (RFP) where an average male of 160

pounds is used to assume the largest possible cockpit configuration case. Cockpits can always be made smaller, but not always larger. To meet the safety requirements, measured and quantified field of views, reach, and layouts were designed as shown below.

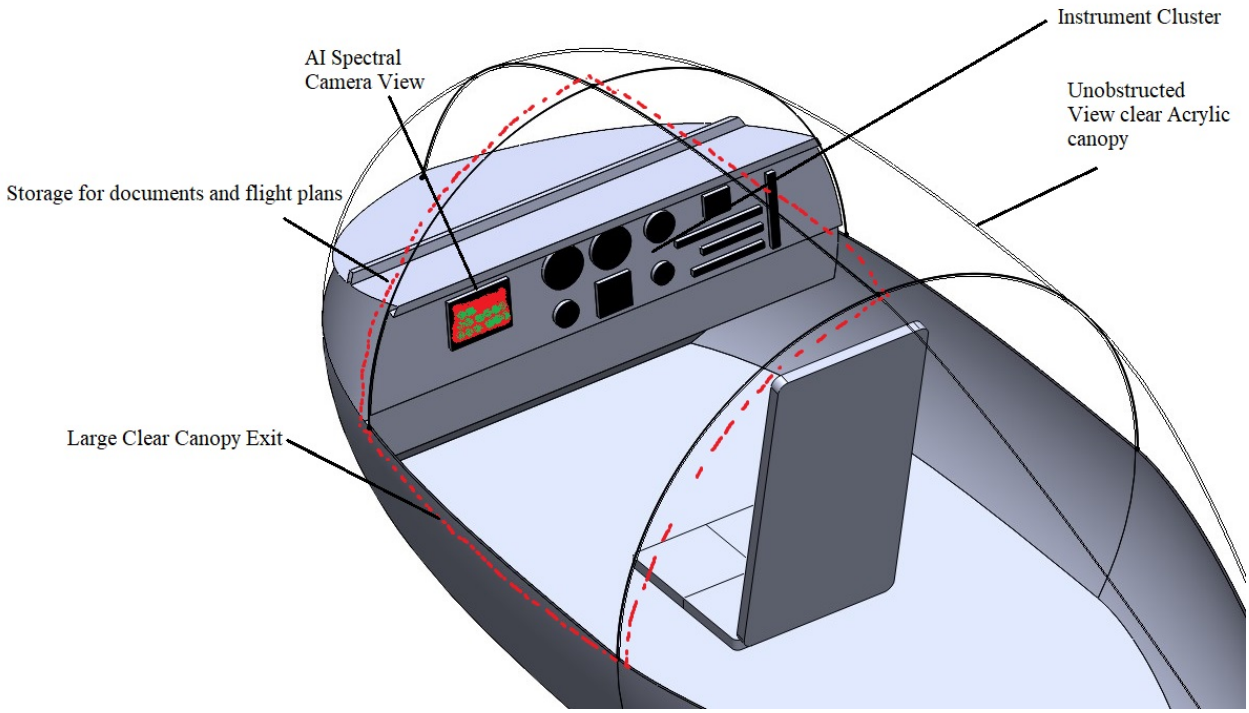

Fig. 46 Isometric Cockpit View

Figure 46 depicts a view of the instrumentation dashboard where the spectral imaging view that the pilot would see is on the left of the screen. All controls are laid out closely for easy reach and satisfy FAR 23.771 requirements for location and spacing in the cabin, namely that controls are located on the left pictured in Figure 44 and that the instrument cluster is unobstructed as well as has glare protection from the canopy.

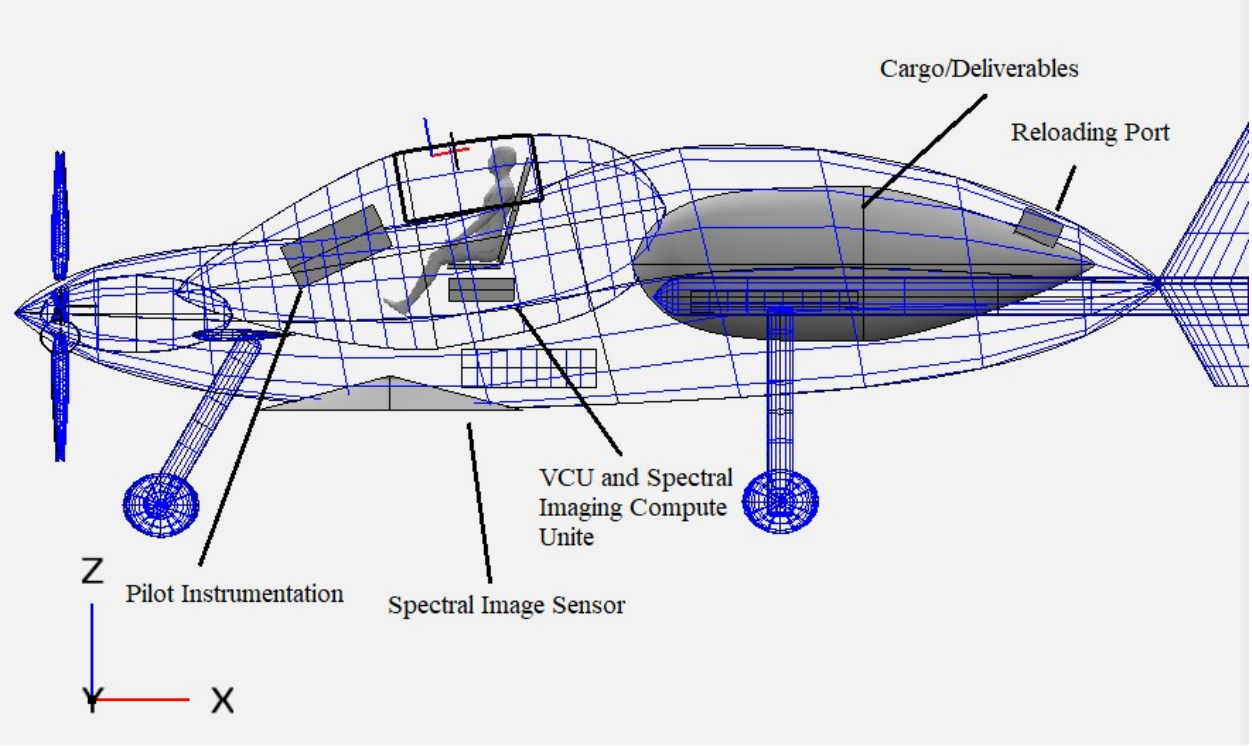

Fig. 47 Side View Plane Layout

Figure 47 shows the component layout of the cargo, the pilot, the spectral imaging sensor, and the compute unit for the spectral sensor itself, as it requires a lot of power. The total volume of the cargo was validated using CAD to be **364123.89 cubic inches**.

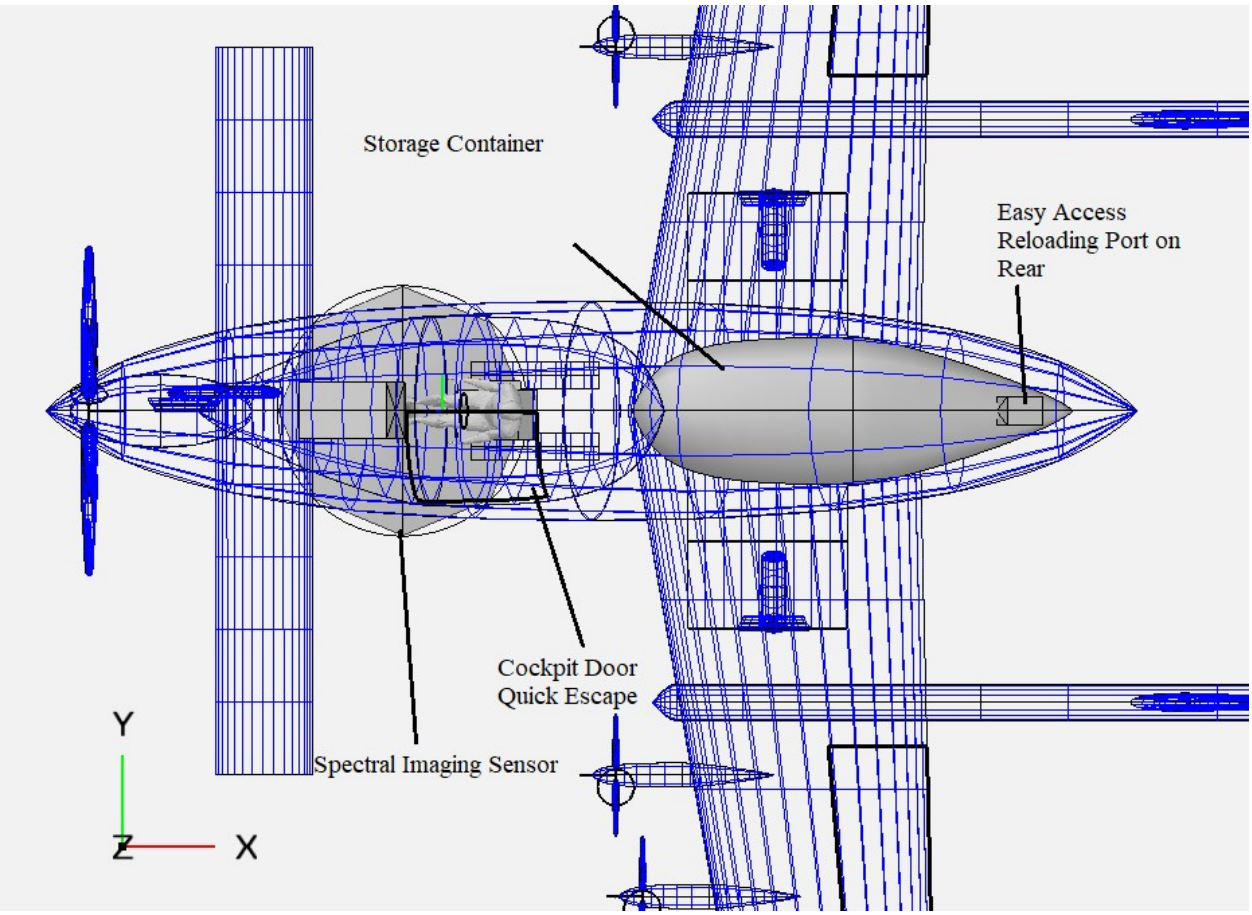

Fig. 48 Top Layout of Unique Access Points

Figure 48 loading port for the hopper demonstrates how easy it is to reload. The traditional method of using a specialty vehicle and approaching from the side of the aircraft would not work as it requires the shutting down of the distributed electrical propulsion system, and increasing the turnaround time. The width of the boom tail is key for allowing rapid reloading and does not require the pilot to turn off the engines.

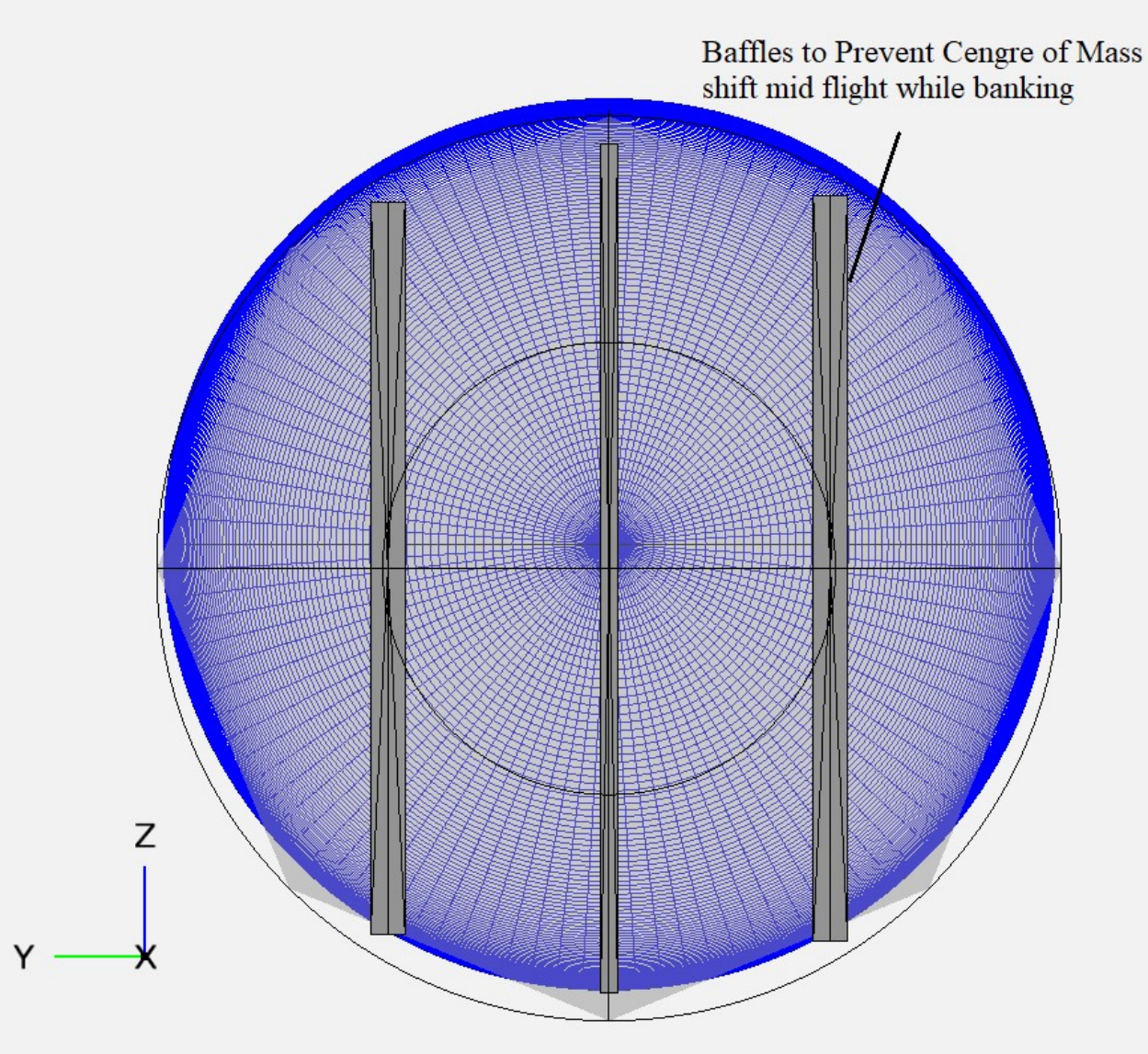

Fig. 49 Cross Section Cargo Hold

Figure 49 depicts a cross-sectional view of the cargo hold. Due to the nature of top dressing, the cargo can be anything from liquid to grain. In any case, the cargo is assumed to be non-solid, as well as draining during flight. This presents a specific problem for aircraft and large oil tankers as the large shift in the center of gravity as the vehicle moves around. To prevent this, large baffles are installed with outlets at the bottom and top which will keep the cargo from rapidly affecting the in flight performance and stability of the aircraft.

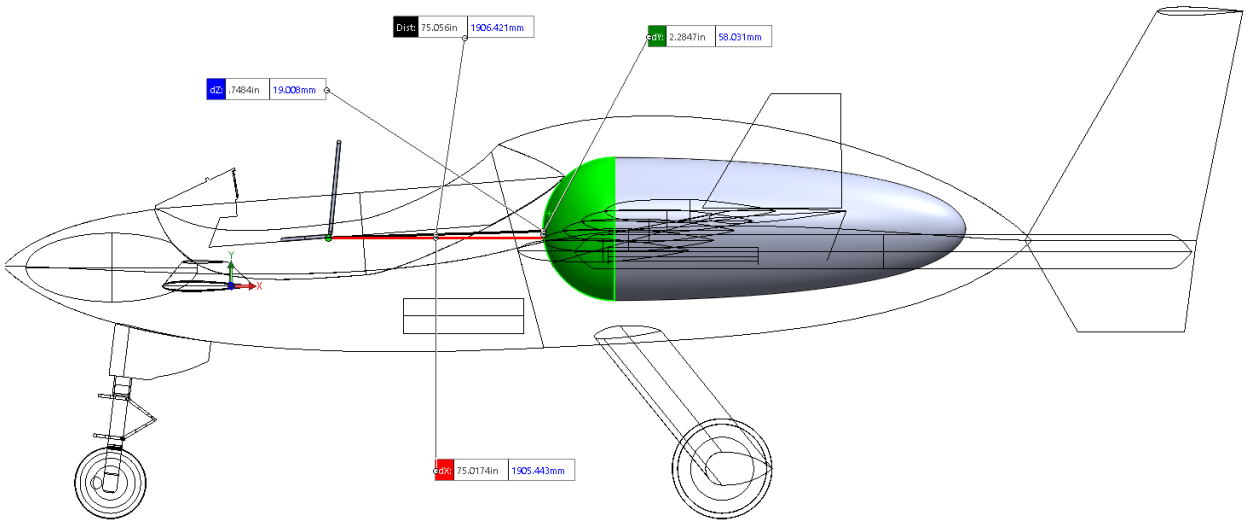

Fig. 50 Side View Payload Layout

Figure 50 shows the distance between the payload and the back of the seat of the pilot and the payload which is 75 inches. This is ample room to isolate the cabin structure and the cargo hold of any smells or oders that may violate FAR 23.771.

B. Powertrain Configuration

The hybrid-electric aircraft will feature a turboprop engine similar to the P&W PT6A-15AG of the AT-402B, which is capable of producing a maximum of 680 hp. The dimensions of the proposed engine are based on the dimensions of this engine, and include the gearbox and gas turbine. 2 battery packs are used to power the 10 distributed electric motors, which are connected to the turbofan engine in a serial-parallel partial hybrid configuration in order to recharge during flight while also providing supplemental power to the electric motors. 2 fuel tanks are placed in the wings to supply the gas engine with fuel. The dimensioned powertrain configuration can be seen in Figure 51. All dimensions are given in feet.

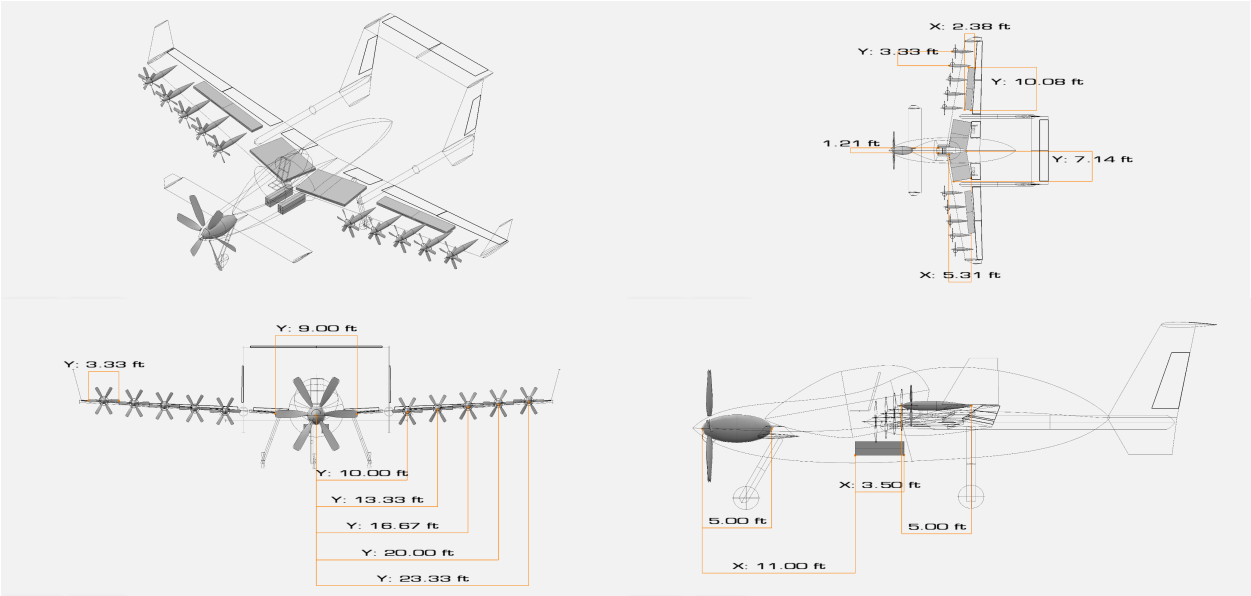

Fig. 51 Dimensioned Powertrain Configuration

XIII. Cost

A cost estimate was performed using the estimated weight and power of the aircraft to find the RDT&E, flyaway, and direct operating costs (DOC). The RAND DAPCA IV Model from Raymer was used to predict the RDT&E costs associated with engineering, tooling, manufacturing, development support, flight testing and manufacturing materials. The equations to predict the amount of hours and cost for each are listed below. A max velocity of 250 kts was used based on the RFP, with a predicted quantity of 100 aircraft.

$$H_E = 4.86 \cdot (W_e)^{0.777} \cdot V^{0.894} \cdot Q^{0.163} \tag{87}$$

$$H_T = 5.99 \cdot (W_e)^{0.777} \cdot V^{0.696} \cdot Q^{0.263} \tag{88}$$

$$H_M = 7.37 \cdot (W_e)^{0.82} \cdot V^{0.0484} \cdot Q^{0.641} \tag{89}$$

$$H_Q = 0.133 \cdot H_M \tag{90}$$

$$C_D = 91.3 \cdot (W_e)^{0.630} \cdot V^{1.3} \tag{91}$$

$$C_F = 2498 \cdot (W_e)^{0.325} \cdot V^{0.822} \cdot (\mathrm{FTA})^{1.21} \tag{92}$$

$$C_M = 22.1 \cdot (W_e)^{0.921} \cdot V^{0.621} \cdot Q^{0.799} \tag{93}$$

The rates of labor, tooling, quality control and manufacturing were estimated using given rates from Raymer and converting to 2025 dollars. The rates are listed below.

The total RDT&E costs were computed by multiplying the respective labor rates to their respective hours, and then summing up all the individual costs. The flyaway cost was predicted using a rough estimate based on the estimated MTOW of the aircraft. The equation from the Metabook is listed in Equation (94)

$$C_{\text{aircraft}} = 10^{(1.1846+1.2625 \cdot \log(\mathrm{MTOW}))} \cdot \mathrm{CEF} \tag{94}$$

Table 20 Rates of labor

Category	Rate/hr ($)
Engineering	158.4
Tooling	172.1
Quality Control	153
Manufacturing	138

The engine cost for a fully gas turbine power plant was estimated using the following equation from the Metabook.

$$C_{\text{engines}} = 10^{(2.5262+0.9465\cdot\log(\text{SHP\_TO}))} \cdot \text{CEF} \tag{95}$$

Based on the hybridization ratio of the plane that was being analyzed, the SHP_{TO} was divided into gas and electric portions, which were used to calculate the cost of the electric motors used. A value of $150/hp was used from the Metabook.

$$C_{motors} = 150 \cdot SHP_{TO} \cdot \text{CEF} \tag{96}$$

In hybrid and electric cases, the battery costs were accounted for as well, using a value of $520/kWh from the Metabook, where e is the energy density of the battery.

$$C_{batteries} = 520 \cdot e \cdot W_b \cdot \text{CEF} \tag{97}$$

For fully electric configurations, the cost of the engines is subtracted from the cost of the aircraft, and the cost of the motors and batteries are added to get the estimated cost of the aircraft. For the flyaway cost, an additional avionics cost factor is added to the aircraft cost, along with a 10% profit margin, as seen below.

$$C_{flyaway} = 1.1 \cdot (C_{aircraft} + C_{avionics}) \tag{98}$$

For operation and maintenance costs, costs such as crew, fuel, electricity, landing fees, navigation, airframe and engine maintenance, insurance, registration, and financing were all considered as contributing factors to the DOC. Additional cost equations are listed in the appendix. The estimated costs are listed in Table 21

Table 21 Estimated Costs for Conceptual Design

RDT&E ($ Million)	Flyaway ($ Million)	DOC ($\frac{\$}{\text{cargo ton - nmi}}$)
$150.5	$4.89	$116.36

There are challenges with estimating the cost of hybrid electric aircraft due to lack of historical data. The reason these numbers are high is likely due to the fact that the equations used to estimate the electric components of the powertrain tend to inflate the cost of the aircraft, since it is adding the costs of these components to the cost of a fully gas powered plane. More detailed cost analysis of various components is required to determine a more accurate cost.

XIV. Risk Analysis and Certification

This aircraft is subject to the FAR 23 FAA airworthiness standards for characteristics involving the risk analysis of flight control failure. The CD-4 meets these requirements through "drive-by-cable" systems with double redundancy and the use of push-rods instead of cables to reduce "stretch" and increase durability at the cost of weight. This is achievable without violating the internal maximum weight allowed for control surfaces systems due to the short fuselage of the CD-4. This is a high level analysis of the control surfaces fault tree, and makes assumptions of grouping all components under the same name in the fault tree. For this analysis pitch is considered, however a similar fault tree can be applied to all other control surfaces as the type of mechanism is shared. All control surfaces are subject to the input force limit

of FAR 23.397 (b) which describes the max input force required. Calculation of the required lengths and sizes of the mechanical design are omitted for here for brevity, as they are trivial to assuring the pilot input force is not exceeded.

A. Basic Design

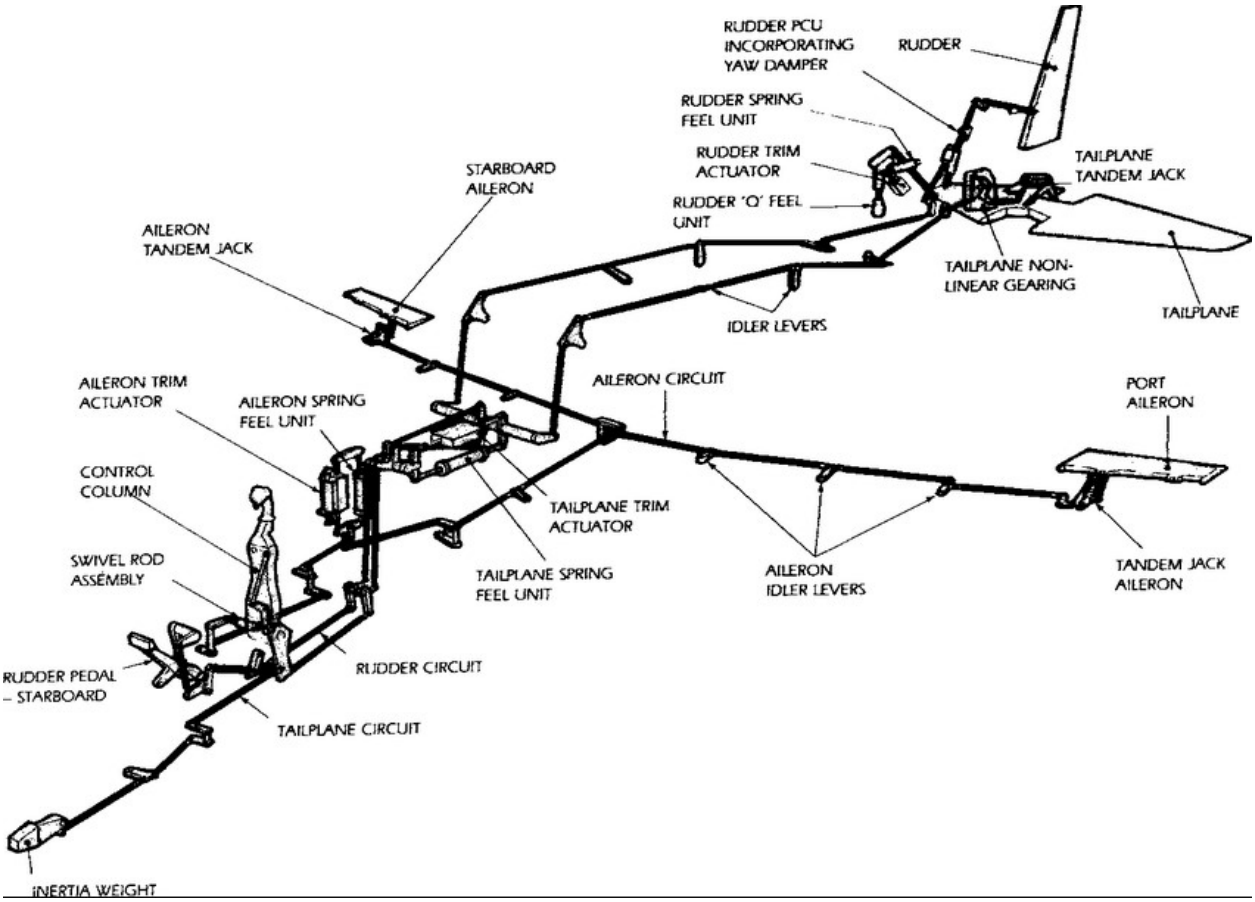

Fig. 52 Hawk 200 Push-Pull Rod Control System

The basic design of the controls surface system can be described as "push-pull" rod control system. This is a "fly-by-cable" system where the cables are replaced by rods which can act both in tension and compression. Different from the Hawk 200 in Fig. 40 is the addition of a front canard control surface as well as a second set of push-pull rods for controls mounted on the main wing. This is done to assure redundancy between controls, as all directions of motion either have 2 control surfaces that can act, or in the case of the main wing a second set of connecting rods. Pitch is redundant due to the rear horizontal stabilizer and the front canard, yaw is taken care of through the dual vertical stabilizers. Push-pull rod mechanisms offer significant advantages, namely the reduction in "slack" on fly-by-cable systems, the resistance to corrosion given they do not have the small crevasses found in cables, and the increased pilot response due to their stiffness. The large downside is weight as rods are still heavier than cables, even in hollow tube form. The weight requirement is still achievable as mentioned before due to the short frame of the aircraft, which reduces the length of rod required.

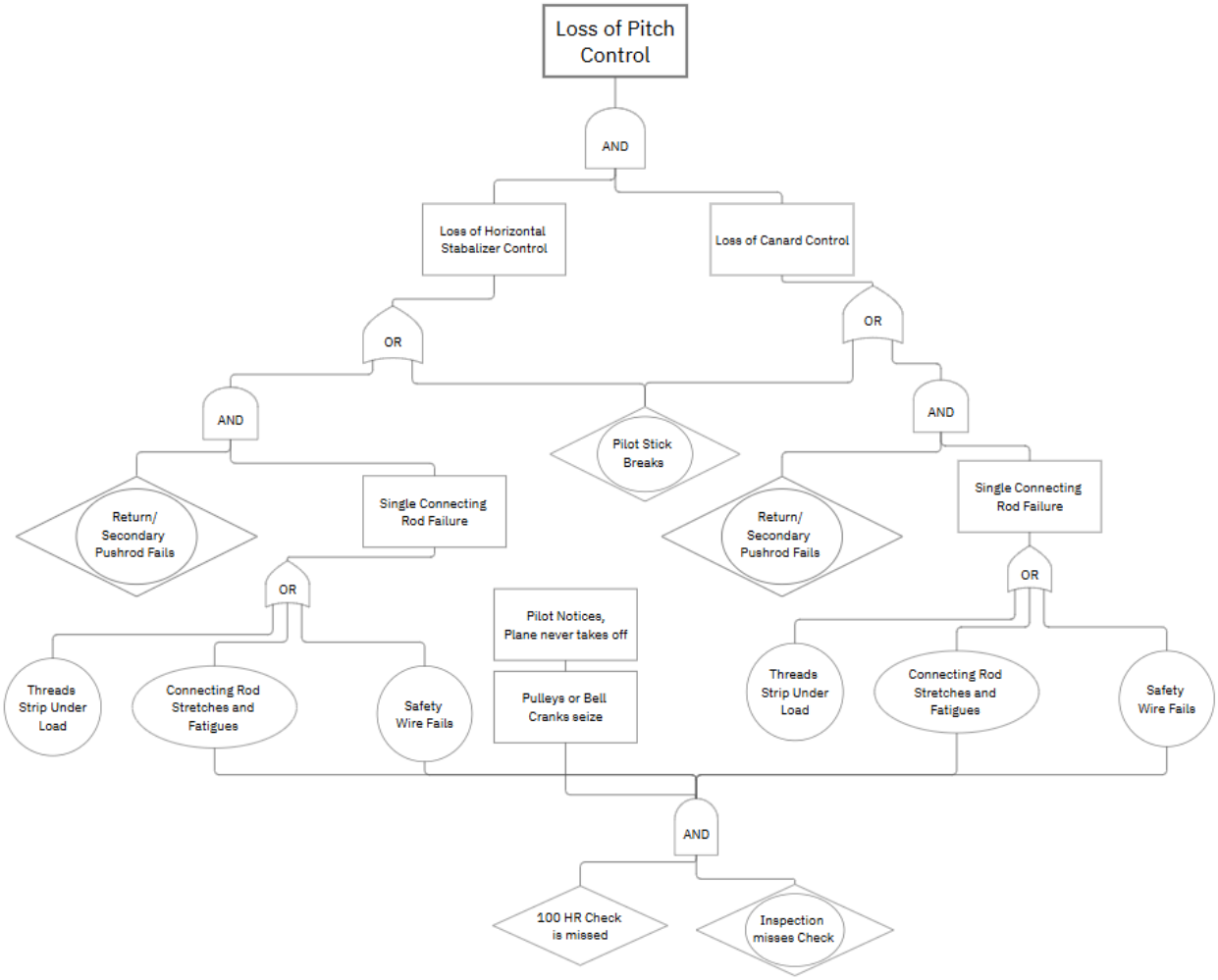

Fig. 53 Fault Tree analysis for Pitch Control

The requirements of FAR 23 for controls fall under Part 23, Subpart D 23.2300 which says: "(a)The applicant must design airplane flight control systems to: (1) Operate easily, smoothly, and positively enough to allow proper performance of their functions. (2) protect against likely hazards.". These requirements are satisfied under the use of a push and pull rod system which acts on rod ends which hold frictionless bearings in the design. To add to this standard, a number of cases and conditions are taken inspiration from the FAR 25 requirements to understand any modes of failure.

B. Single Rod Operational Condition

Should a single rod fail or break under flight for the pitch condition, the opposing pitch control surface can be used to control pitch in its absence. While the rear horizontal stabilizer is not adequately sized to give the full range of pitch motion up and down, it is sufficient to give enough control over the pitch of the aircraft to descend or ascend at a safe vertical rate, that is to say, without lowering the speed considerably close to stall. The main wing is designed with two redundant push-pull rods, and in the event one fails, the second one is sized such that it will retain full operation control of roll and flaps with respect to the required pilot input force

C. Stuck Rod Condition

Stuck rod or bell crank conditions can be handled through the secondary surfaces or mechanisms such as using the canard for pitch or the horizontal stabilizer. Should the system rust entirely and seize, the plane cannot physically taxi or take off as stick will not respond. Rust seizing mid flight is incredibly unlikely as the length of the whole mission profile is not enough time to develop rust that penetrates zinc-coated corrosion resistant AN fasteners.

D. Failure to inspect at 100 flight hours

While uncommon, the failure to inspect at 100 flight hours is the basis for the failure of the push-pull rods in the aircraft. It is critical to ensuring there is no flexure, and that all bearings or moving pieces are lubricated as required by the flight manual. If the check is forgotten, and the logbook check is also overlooked, then the fatigue, stretching, and safety wire failure scenarios enact, which if continuously unchecked over time can lead to a Single Rod Operational condition as described above. This is unlikely to begin with, and the failure tree shown above is only enacted when a repeated negligence for pre-flight inspection is done. It is important to note that all rod ends are considered "sealed" such that they do not need regular lubrication, however, do need regular inspection to see if the rotating surface has rusted.

XV. Method Validation

A. Weight Estimation Code

The AT-402B was selected as the comparable aircraft to validate the weight estimation and sizing code. Air Tractor's website[14] gives 9160 lbs as the MTOW, but 8,600 lbs as the takeoff weight when providing parameters such as climb speed and takeoff field length. The website does not provide details about the loading configurations of each weight, therefore it will be assumed that 8600 lbs is the usual takeoff weight, while 9160 lbs is the absolute maximum this aircraft can be loaded. The empty weight of the aircraft with the spray equipment is 4,299 lbs. The payload capacity is given in gallons, which makes it difficult to determine the weight of the maximum payload the aircraft can carry. However, since many sprays are mostly water, we can assume the hopper is filled with 400 gallons of water, which corresponds to 3331 lbs. With the empty and payload weights known, the fuel weight and MTOW of the aircraft can be estimated with the code. Various aerodynamic parameters had to be estimated for the aircraft. The Oswald efficiency factor is estimated to be 0.7 for rectangular wings and C_{D_0} is estimated to be 0.03. All other parameters are from Air Tractor's website. The convergence of the MTOW of the AT-402B is seen in Figure 54, while the convergence of the weight with max fuel is seen in Figure 55. An initial guess of 10,000 lbs was used in both cases.

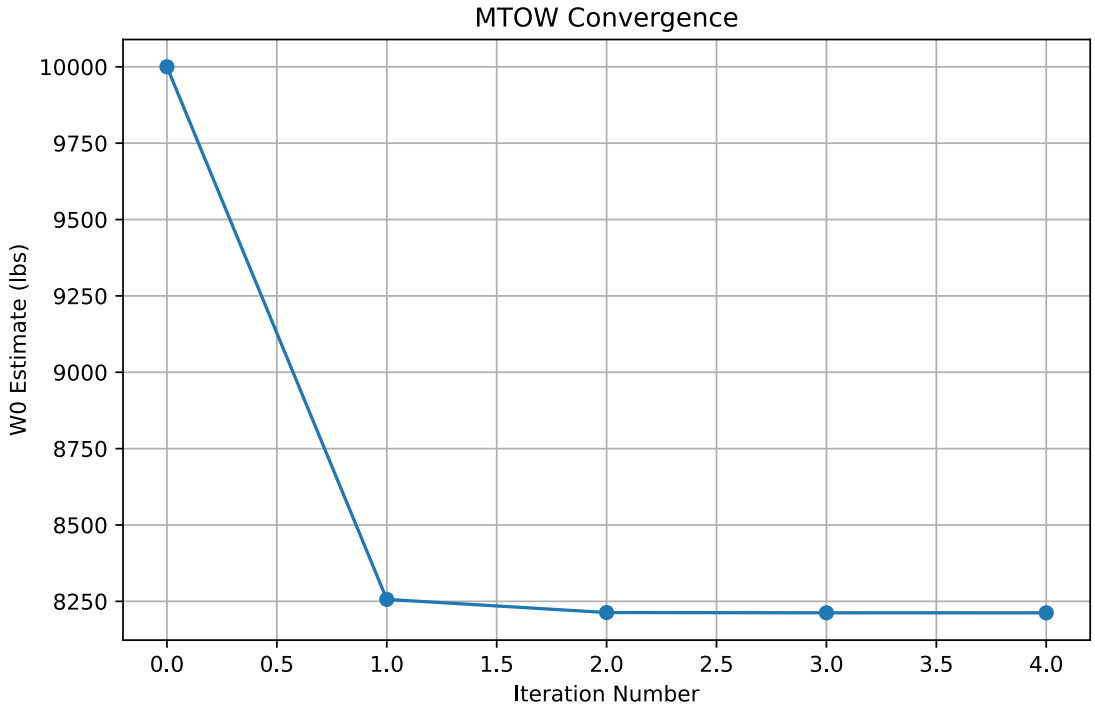

Fig. 54 MTOW convergence for AT-402B

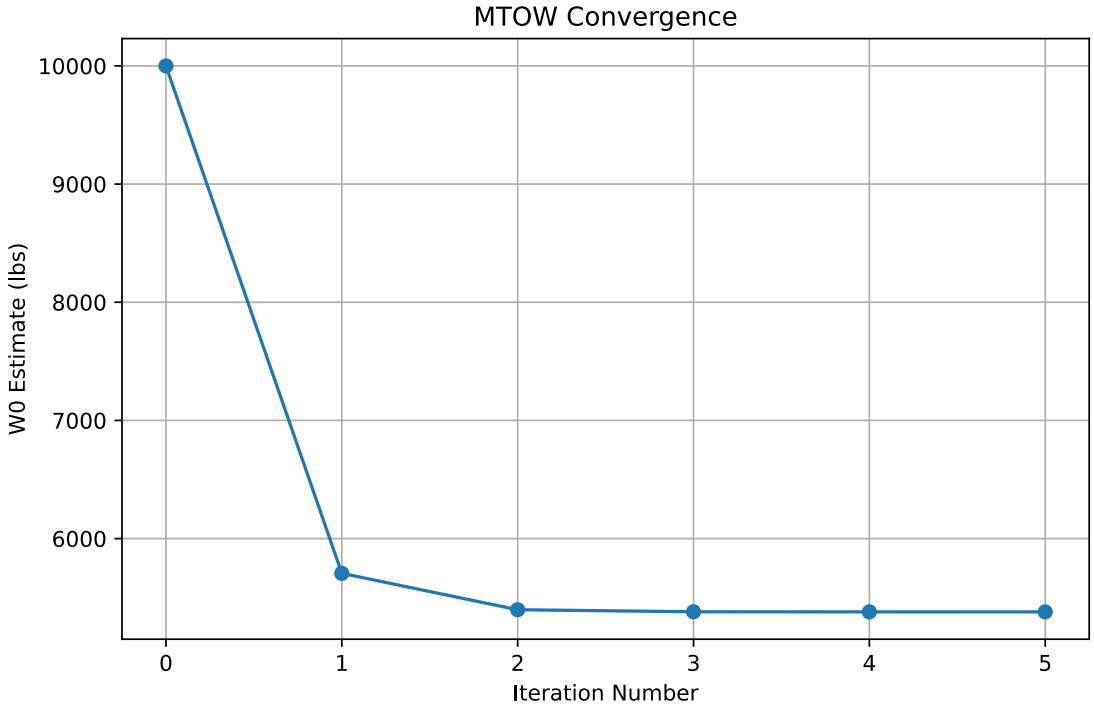

Fig. 55 Max range weight convergence for AT-402B

The code converged a weight of 8212 lbs and a fuel weight of 392 lbs for the standard mission configuration. The code converged a weight of 8212 lbs and a fuel weight of 890 lbs for the ferry mission configuration. When compared to the AT-402B's 170 gallon fuel tanks that can hold 1139 lbs of Jet A1 Fuel, the calculated maximum fuel weight is much lower. This discrepancy is likely due to the different loading configurations the AT-402B may have that vary how much payload and fuel it carries at one time, making it hard to compare actual fuel and weight values for a standard mission. The assumption for the ferry mission in the weight code is that the aircraft is carrying 0 payload, while the AT-402B may be able to carry a certain amount of payload for its maximum range. This may be the reason it has a higher MTOW value, since it is able to carry both the maximum amount of fuel and some payload. The standard mission the AT-402B was designed for may be different than the one in the RFP, meaning the required range for the mission may be higher, requiring more fuel.

B. Sizing Code

Parameters pertaining to the AT-402B from Air Tractor's website [14] were input into the sizing code in order to validate the code. For the stall, since the stall speed (57 kts), landing weight (7000 lb), and wing area (306 ft^2) are already known, a maximum lift coefficient could be calculated using the lift equation. This resulted in a value of 2.08, which is slightly higher than the estimated maximum lift coefficient of 1.9 used for the CD-4 Cybertruk. The takeoff distance is given as 975 ft at a takeoff weight of 8600 lbs. However, this is not specified if this is the total ground roll or obstacle clearance distance, therefore, it will be assumed to be the total ground roll. Since the AT-402B is a single engine aircraft, the one engine inoperative climb constraint will be removed. By inputting known parameters into the code, non-dimensional and dimensional sizing plots were produced. The actual wing and power loading values of 22.9 lb/ft^2 and 13.5 lb/hp of the AT-402B is marked as the design point in red on the plot.

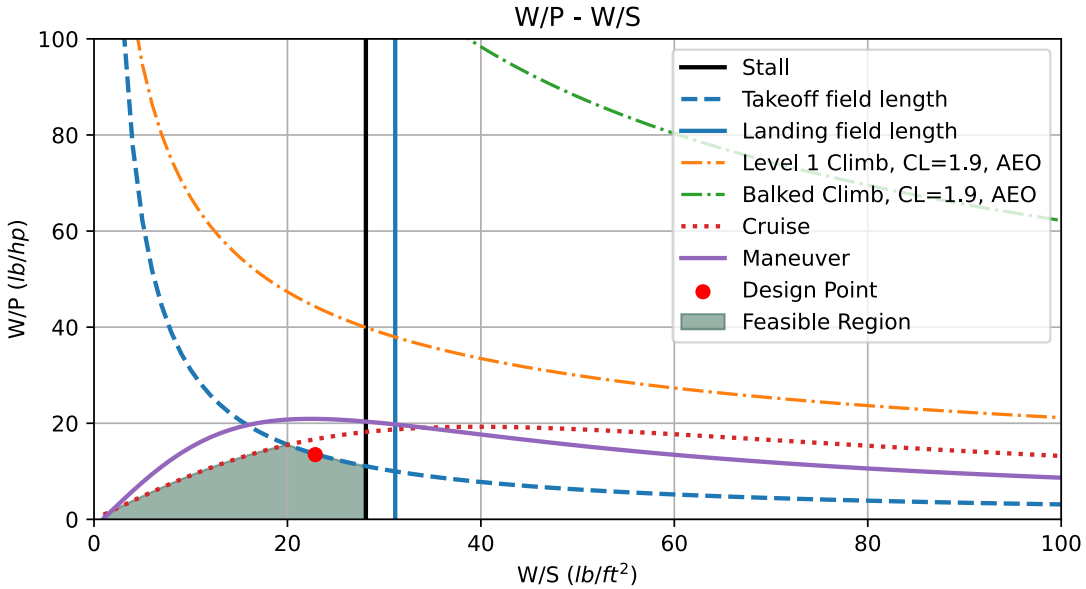

Fig. 56 Power Loading for AT-402B

Using the takeoff weight of 8600 lbs, the power loading graph was used to generate a power vs wing area graph to see if the design point (306 ft^2, 680 hp) falls within the feasible region.

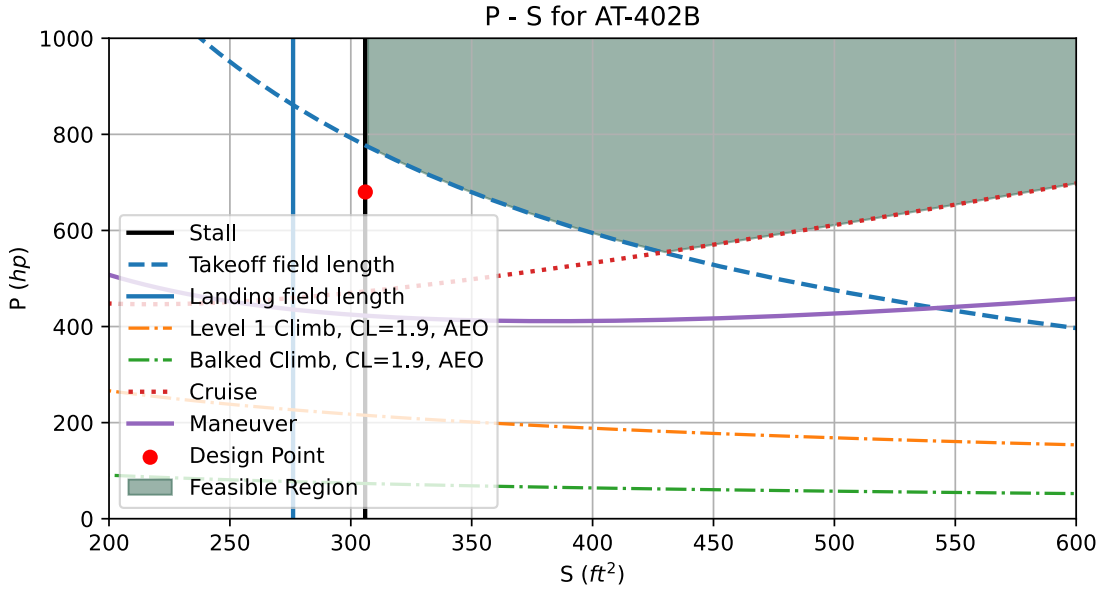

Fig. 57 Power vs Area for AT-402B

The design point falls on the stall line since the actual weight and wing area were used to determine the input for $C_{L_{max}}$. A conversion had to be made for this validation, since the stall speed was given at the landing weight of 7000, but the takeoff weight was used to get the power vs wing area graph. The actual design point falls just below the takeoff field length graph. This may be due to the ambiguity given in the AT-402B on what the takeoff field length was in the given parameters. Additionally, another discrepancy seen is that the maneuver curve is no longer an active constraint. This could potentially be caused by the AT-402B using different maneuver speeds than the ones that were input. 110

knots was used from previous computations, since it falls within the working speed range of the AT402B. However this value can vary, leading to the curve shifting up or down in various locations.

XVI. Computation Procedure and Software Design

A. Weight Estimation Software Design

The weight estimation code consisted of a function with a while loop that measured the error between previous and current guesses to determine whether the weight converged to a value. The function inputs consisted of an initial weight guess, the empty weight from the component build up, the crew and payload weights, the mission type, profile drag coefficient, aspect ratio, battery energy density, and hybridization ratio. The function returned the converged weight, fuel weight, and battery weight. Within the function was another function to estimate the fuel fraction and battery weight. The inputs for the fuel fraction function included the max power of the engine, the weight guess, the wing area, the profile drag coefficient, the aspect ratio, the Oswald efficiency factor, the number of segments to divide climb and cruise conditions into, the mission profile, the hybridization ratio, and the battery energy density. The fuel fraction function returned the fuel weight, reserve fuel weight, and the battery weight.

B. Sizing Estimation Software Design

The code defined functions for each constraint. The input of these functions were values from the RFP such as takeoff field length and stall speed, as well as estimated values such as $C_{L_{max}}$ or air density. These functions returned W/S values for stall and landing, as well as W/P arrays for every other constraint. A W/S array was created, which was then used to plot the constraint arrays on the same plot. The intersection point of the takeoff and maneuver constraint curves was found using a minimum difference function to determine the maximum value of the power loading, which was selected as the design point. A print statement was used to determine the wing and power loading values at this point. A fill between function was implemented to shade the areas under the active constraints that was defined as the feasible area. The output from the weight estimation code was input into the code, and was divided by the constraint power loading and wing loading arrays to obtain dimensional values. These dimensional values were then plotted on a new graph. Using similar methods mentioned previously, the feasible region and design point were defined and plotted.

C. Specific Range vs Cruise Speed Trade Study Software Design

Python was used along with equations in the Metabook. Functions were defined to calculate temperature, air density, and speed of sound as a function of altitude, based on standard atmospheric assumptions. These values were used to compute true airspeed for each Mach number and altitude combination. For each altitude, dynamic pressure and lift coefficient values were calculated across the range of airspeeds. These were then used to determine total drag and, subsequently, fuel flow rate using a thrust-specific fuel consumption model. The specific range was computed by dividing airspeed by fuel flow. Results were stored in a grid and plotted as a carpet plot, with specific range on the y-axis and cruise airspeed on the x-axis. Each curve represents a different altitude. In addition to these curves, constant Mach number contours were plotted across the graph and labeled to show the relationship between cruise Mach number and performance.

XVII. Conclusion

The CD-4 CyberTruk satisfies the requirements of an advanced agricultural aircraft as stated in the RFP. The design is able to complete the main design mission of carrying 2000 lbs of payload for covering a 400 acre area that is 25 nmi away from the takeoff point. Additionally, the aircraft meets the ferry mission requirement of reaching a range of 600 nmi. These ranges are verified in the payload range chart, which depicts how far the aircraft can fly for a given payload. The aircraft also meets the takeoff and landing requirements for a total field length of 1500 ft. This was verified in the takeoff and landing sizing calculations, where this value was input and the required power and wing loading were determined. The aircraft achieves the goal of reducing operator exposure to effluents by placing the hopper behind the cockpit, allowing for a safer application of chemicals to fields. The design includes a fault tree analysis for all major control surfaces. The failure analysis begins from the initial control inputs by the pilot in the cockpit and provides a path to the failure of the control surfaces. The aircraft is a fixed-wing design, as mentioned in the RFP.

For innovation and sustainability requirements, the CD-4 CyberTruk utilizes innovative propulsion systems with

its 10 distributed electric propulsion motors and a P&W PT6A-15AG engine that runs on SAFs. These propulsion systems achieve the RFP's goal of creating aircraft that have reduced emissions. Since the DEP produces no emissions if charged with electricity produced by renewable sources, and the gas engine uses SAFs which generate lower amounts of emissions when compared to traditional hydrocarbon fuels, the aircraft produces less emissions when compared to traditional agricultural aircraft. However, trade studies showed that in order for the DEP to be beneficial for fuel savings, large battery energy density is required in order to not add excessive battery weight. The aircraft also uses autonomous systems such as spectral imaging and data processing to help target specific areas of fields that are in need of treatment with aerial sprays. This feature allows the aircraft to reduce the amount of chemicals it sprays, saving money and reducing impact on the environment. Overall, the CD-4 CyberTruk offers a innovative and sustainable way to change the way aircraft are used in agriculture.

References

[1] "Growing at a slower pace, world population is expected to reach 9.7 billion in 2050 and could peak at nearly 11 billion around 2100 \textbar UN DESA \textbar United Nations Department of Economic and Social Affairs," , ????. URL https://www.un.org/development/desa/en/news/population/world-population-prospects-2019.html.

[2] Alfred, R., Obit, J. H., Chin, C. P.-Y., Haviluddin, H., and Lim, Y., "Towards Paddy Rice Smart Farming: A Review on Big Data, Machine Learning, and Rice Production Tasks," *IEEE Access*, Vol. 9, 2021, pp. 50358–50380. https://doi.org/10.1109/ACCESS.2021.3069449, URL https://ieeexplore.ieee.org/document/9389541.

[3] Staff, A. U., "A Century of Agricultural Aviation — 1921-2021 - AgAir Update," , Aug. 2021. URL https://agairupdate.com/2021/08/02/a-century-of-agricultural-aviation-1921-2021/.

[4] Dataintelo, "Agricultural Aircrafts Market Research Report 2032," , ???? URL https://dataintelo.com/report/agricultural-aircrafts-market.

[5] "Sustainable Aviation Fuel Stakeholders Unite to Form the SAF Coalition," , ????. URL https://thesafcoalition.com/news-post/sustainable-aviation-fuel-stakeholders-unite-to-form-the-saf-coalition/, publication Title: SAF Coalition.

[6] Wang, C., Liu, B., Liu, L., Zhu, Y., Hou, J., Liu, P., and Li, X., "A review of deep learning used in the hyperspectral image analysis for agriculture," *Artificial Intelligence Review*, Vol. 54, No. 7, 2021, pp. 5205–5253. https://doi.org/10.1007/s10462-021-10018-y, URL https://doi.org/10.1007/s10462-021-10018-y.

[7] Karunathilake, E. M. B. M., Le, A. T., Heo, S., Chung, Y. S., and Mansoor, S., "The Path to Smart Farming: Innovations and Opportunities in Precision Agriculture," *Agriculture*, Vol. 13, No. 8, 2023, p. 1593. https://doi.org/10.3390/agriculture13081593, URL https://www.mdpi.com/2077-0472/13/8/1593.

[8] Ali, M. A., Dhanaraj, R. K., and Nayyar, A., "A high performance-oriented AI-enabled IoT-based pest detection system using sound analytics in large agricultural field," *Microprocessors and Microsystems*, Vol. 103, 2023, p. 104946. https://doi.org/10.1016/j.micpro.2023.104946, URL https://www.sciencedirect.com/science/article/pii/S0141933123001904.

[9] Wu, Y., "Application of aluminum alloy in aircraft," *Journal of Physics: Conference Series*, Vol. 2228, No. 1, 2022, p. 012024. https://doi.org/10.1088/1742-6596/2228/1/012024, URL https://dx.doi.org/10.1088/1742-6596/2228/1/012024.

[10] "The Advantages and Disadvantages of Alloy Steel - MFG Shop," , Dec. 2024. URL https://shop.machinemfg.com/the-advantages-and-disadvantages-of-alloy-steel/.

[11] Kilimtzidis, S., Kotzakolios, A., and Kostopoulos, V., "Efficient structural optimisation of composite materials aircraft wings," *Composite Structures*, Vol. 303, 2023, p. 116268. https://doi.org/https://doi.org/10.1016/j.compstruct.2022.116268, URL https://www.sciencedirect.com/science/article/pii/S0263822322010005.

[12] Roskam, J., *Airplane Design: Preliminary sizing of airplanes*, Airplane Design, DARcorporation, 1997. URL https://books.google.com/books?id=usXVaf8Qu0cC.

[13] "AT-802A," , ????. URL https://airtractor.com/aircraft/at-802a/, publication Title: Air Tractor.

[14] "AT-402B," , ????. URL https://airtractor.com/aircraft/at-402b/, publication Title: Air Tractor.

[15] Ribeiro, G., "How does Lilium eVTOL jet propulsion work?" , Oct. 2023. URL https://mundogeo.com/en/2023/10/10/how-does-lilium-evtol-jet-propulsion-work/, publication Title: MundoGEO.

[16] "SAWE 66. Estimating Weight of Aircraft Electrical Wiring Systems," , ????. URL https://www.sawe.org/product/paper-0066/.

[17] "Piktronik - DC/DC converters," , ????. URL https://www.piktronik.com/en-products-dcdc-converters.

[18] "SDM-CD16ACA - 16-Channel AC/DC Relay Controller," , ????. URL https://www.campbellsci.com/sdm-cd16aca.

[19] Raymer, D., Aeronautics, A. I. o., and Astronautics, *Aircraft Design: A Conceptual Approach*, AIAA Textbook Series, American Institute of Aeronautics and Astronautics, 1989. URL https://books.google.com/books?id=Q9QeAQAAIAAJ.

[20] Martins, J. R. R. A., *The Metabook of Aircraft Design*, 2016.

[21] "SAWE 128. Weight Estimating of Aircraft Hydraulic Systems," , ????. URL https://www.sawe.org/product/paper-0128/.

[22] Kuśmierek, A., Grzeszczyk, R., Strohmayer, A., and Galinski, C., "Analysis Leading to the Design of a Hybrid Gas-Electric Multi-Engine Testbed," *Aerospace*, Vol. 10, 2023, p. 998. https://doi.org/10.3390/aerospace10120998.

[23] De Vries, R., Brown, M., and Vos, R., "Preliminary Sizing Method for Hybrid-Electric Distributed-Propulsion Aircraft," *Journal of Aircraft*, Vol. 56, No. 6, 2019, pp. 2172–2188. https://doi.org/10.2514/1.C035388, URL https://arc.aiaa.org/doi/10.2514/1.C035388.

[24] "Glass Fiber Composite Price, 2025 Glass Fiber Composite Price Manufacturers & Suppliers | Made-in-China.com," , ????. URL https://www.made-in-china.com/products-search/hot-china-products/Glass_Fiber_Composite_Price.html?utm_source=chatgpt.com.

[25] "Carbon Fiber vs. Aluminum: A Side-by-Side Comparison," , ????. URL https://carbonfibergear.com/blogs/carbonfiber/carbon-fiber-vs-aluminum.

[26] Davis, T., "Carbon Fiber vs. Fiberglass: A Comprehensive Comparison," , Aug. 2024. URL https://customfrp.com/carbon-fiber-vs-fiberglass-a-comprehensive-comparison/, publication Title: CustomFRP.

[27] "Carbon Fiber Vs. Fiber Glass: What's the Difference," , ????. URL https://www.nitprocomposites.com/blog/carbon-fiber-vs-fiber-glass, publication Title: NitPro Composites.

[28] Expert, A. M. S., "Alloy Steels: From Industrial Use to Aerospace Innovations," , Nov. 2023. URL https://friendmetals.com/alloy-steels-from-industrial-use-to-aerospace-innovations/, publication Title: Friend Metals Distributor.

[29] mavenstainlesssteel.com, "How Stainless steel plays a vital role in the aerospace Industry?" , Jan. 2021. URL https://www.mavenstainlesssteel.com/how-stainless-steel-plays-a-vital-role-in-the-aerospace-industry/, publication Title: Stainless Steel Manufacturer \textbar Maven Stainless Steel.

[30] "Advancing Aerospace: The Dominance of Fiberglass Composites," , ????. URL https://www.aerospheres.com/news/Advancing-Aerospace-The-Dominance-of-Fiberglass-Composites/.

Appendix

Acronyms

- AR: Area Ratio
- BLF: Balanced field length
- CEF: Cost Escalation Factor
- DEP: Distributed Electric Propulsion
- DOC: Direct Operating Cost
- EM: Electronic Motor
- FTA: Number of flight test aircraft
- GB: Gearbox
- GT: Gas Turbine
- MTOW: Maximum Take-Off Weight
- PM: Power Management and Distribution System (Control System)
- SHP_TO: Shaft Horsepower at Takeoff

List of Symbols

Greek Letters

- α: Angle of attack
- γ: Climb angle
- δ: Deflection angle
- λ: Sweep angle
- μ: Dynamic viscosity
- η_p: Propeller efficiency
- Φ: Hybridization ratio
- ϕ: Bank angle
- ρ_f: Density of fuel
- ρ_0: Air density at sea level
- ρ_{cr}: Air density at cruise altitude

Non-Greek Letters

- b: Wingspan
- C_{aircraft}: Total cost of the aircraft
- C_{engines}: Total cost of the engines
- C_{airframe}: Cost of the airframe
- C_{D}: Coefficient of drag
- C_{D0}: Minimum coefficient of drag
- C_{L}: Coefficient of lift
- $C_{L_{max}}$: Maximum coefficient of lift
- C_{L_w}: Wing lift coefficient
- C_{L_h}: Tail lift coefficient
- $C_{m_{cg}}$: Pitching moment coefficient about the CG
- C_{m_w}: Wing pitching moment coefficient (about the wing aerodynamic center)
- $C_{m_{fus}}$: Pitching moment coefficient of the fuselage, nacelles, and other components (about the CG)
- N_{eng}: Number of engines
- P_{TO}: Power available at takeoff
- P_{cr}: Power available at cruise
- Q: Number of aircraft to be produced
- R: Range of the aircraft
- R_E: Engineering labor rate
- R_T: Tooling labor rate
- R_M: Manufacturing labor rate
- R_Q: Quality control labor rate
- S: Wing planform area
- S_{a}: Aircraft approach distance
- $S_{\text{TO}_{\text{G}}}$: Takeoff ground field length
- S_{ref}: Reference area
- S_{wet}: Wetted area
- V: Maximum velocity of the aircraft
- V_{cr}: Cruise velocity
- W_e: Empty weight of the aircraft
- W_A: Weight of the airframe
- W_f: Weight of fuel
- W_{takeoff}: Takeoff weight

Cost Equations

1. Aircraft Cost

$$C_{\text{aircraft}} = 10^{(1.1846+1.2625 \cdot \log(\text{MTOW}))} \cdot \text{CEF}$$

2. Engines Cost

$$C_{\text{engines}} = 10^{(2.5262+0.9465 \cdot \log(\text{SHP\_TO}))} \cdot \text{CEF}$$

3. Airframe Cost

$$C_{\text{airframe}} = C_{\text{aircraft}} - C_{\text{engines}}$$

4. Cost Escalation Factor (CEF)

$$\text{CEF} = \frac{t_{\text{CEF}}}{b_{\text{CEF}}}$$

5. Base Year CEF

$$b_{\text{CEF}} = 5.17053 + 0.104981 \cdot (b_{\text{year}} - 2025)$$

6. Target Year CEF

$$t_{\text{CEF}} = 5.17053 + 0.104981 \cdot (t_{\text{year}} - 2025)$$

7. Engineering Hours

$$H_E = 4.86 \cdot (W_e)^{0.777} \cdot V^{0.894} \cdot Q^{0.163}$$

8. Tooling Hours

$$H_T = 5.99 \cdot (W_e)^{0.777} \cdot V^{0.696} \cdot Q^{0.263}$$

9. Manufacturing Hours

$$H_M = 7.37 \cdot (W_e)^{0.82} \cdot V^{0.0484} \cdot Q^{0.641}$$

10. Quality Control Hours

$$H_Q = 0.133 \cdot H_M$$

11. Development Support Cost

$$C_D = 91.3 \cdot (W_e)^{0.630} \cdot V^{1.3}$$

12. Flight Test Cost

$$C_F = 2498 \cdot (W_e)^{0.325} \cdot V^{0.822} \cdot (\text{FTA})^{1.21}$$

13. Manufacturing Materials Cost

$$C_M = 22.1 \cdot (W_e)^{0.921} \cdot V^{0.621} \cdot Q^{0.799}$$

14. Engine Production Cost

$$C_{\text{eng}} = 3112 \cdot [0.043 \cdot T_{\text{max}} + 243.25 \cdot M_{\text{max}} + 0.969 \cdot T_{\text{turbine\_inlet}} - 2228]$$

15. RDT&E + Flyaway Cost

$$\text{RDT\&E + Flyaway} = (H_E \cdot R_E) + (H_T \cdot R_T) + (H_M \cdot R_M) + (H_Q \cdot R_Q) + C_D + C_F + C_M + (C_{\text{eng}} \cdot N_{\text{eng}}) + C_{\text{avionics}}$$

16. Tooling Labor Rate

$$R_T = 2.883 \cdot y - 5666$$

17. Engineering Labor Rate

$$R_E = 2.576 \cdot y - 5058$$

18. Quality Control Labor Rate

$$R_Q = 2.60 \cdot y - 5112$$

19. Manufacturing Labor Rate

$$R_M = 2.316 \cdot y - 4552$$

20. Crew Cost

$$C_{\text{crew}} = \left[440 + 0.532 \cdot \left(\frac{\text{MTOW}}{1000}\right)\right] \cdot \text{CEF} \cdot t_b$$

21. Fuel Cost

$$C_{\text{fuel}} = 1.02 \cdot W_f \cdot \left(\frac{P_f}{\rho_f}\right)$$

22. Airport Cost

$$C_{\text{airport}} = 1.5 \cdot \left(\frac{\text{MTOW}}{1000}\right) \cdot \text{CEF}$$

23. Navigation Cost

$$C_{\text{navigation}} = 0.5 \cdot \text{CEF} \cdot \frac{1.852 \cdot R}{t_b} \cdot \sqrt{\frac{0.00045359237 \cdot \text{MTOW}}{50}}$$

24. Airframe Labor Maintenance

$$C_{\text{ML}} = 1.03 \cdot \left(3 + \frac{0.067 \cdot W_A}{1000}\right) \cdot RL$$

25. Airframe Material Cost

$$C_{\text{MM}} = 1.03 \cdot (30 \cdot \text{CEF}) + \left(0.79 \cdot 10^{-5} \cdot C_{\text{airframe}}\right)$$

26. Total Airframe Maintenance Cost

$$C_{\text{airframe\_maintenance}} = (C_{\text{ML}} + C_{\text{MM}}) \cdot t_b$$

27. Turboprop Engine Maintenance

$$C_{\text{ML}} = 1.03 \cdot 1.3 \cdot \left(0.4956 + 0.0532 \cdot \frac{\text{SHP\_TO}/N_{\text{eng}}}{1000} \cdot \frac{1100}{H_{\text{em}}} + 0.1\right) \cdot RL$$

28. Annual Utilization

$$U_{\text{annual}} = 1.5 \cdot 10^3 \cdot \left[3.4546 \cdot t_b + 2.994 - \sqrt{12.289 \cdot t_b^2 - 5.6626 \cdot t_b + 8.964}\right]$$

29. Insurance Cost

$$C_{\text{insurance}} = \left(\frac{\text{IR}_a \cdot C_{\text{aircraft}}}{U_{\text{annual}}}\right) \cdot t_b$$

30. Depreciation Cost

$$C_{\text{depreciation}} = C_{\text{unit}} \cdot (1 - K_{\text{depreciation}}) \cdot \frac{t_b}{n \cdot U_{\text{annual}}}$$

31. Registration Cost

$$C_{\text{registration}} = (0.001 + 10^{-8} \cdot \text{MTOW}) \cdot \text{DOC}$$

32. Finance Cost

$$C_{\text{finance}} = 0.07 \cdot \text{DOC}$$

Weight Estimation Code Inputs

- W_e = 4843 lbs
- W_0 = 10000 lbs
- $W_{payload}$ = 2000 lbs
- W_{crew} = 160 lbs
- Mission Profile = 'Standard'
- C_{D0} = 0.03673
- AR = 8.7
- e^* = 550 Wh/kg
- Φ = 0.1

Sizing Code Inputs

- $C_{L_{max}}$ = 1.9
- η_p = 0.80
- ϕ = 45°
- $\rho_{cr} = 1.8685 \cdot 10^{-3}$ slugs/ft^3
- $\rho_{TO} = 2.048 \cdot 10^{-3}$ slugs/ft^3
- $\rho_0 = 2.377 \cdot 10^{-3}$ slugs/ft^3
- s_{TO_G} = 1500 ft
- v_{cr} = 150 kts
- v_{MN} = 110 kts
- v_{stall} = 100 kts